ISSN 1849–0751 (On–line)
ISSN 0013–7448 (Print)
UDK 621.31
https://doi.org/10.37798/EN2025744

Journal of Energy

VOLUME 74 Number 4 | 2025

ENERGIJA 74

Journal of Energy

Scientific Professional Journal Of Energy, Electricity, Power Systems
Online ISSN 1849–0751, Print ISSN 0013–7448, VOL 74
https://doi.org/10.37798/EN2024744

Published by
HEP d.d., Ulica grada Vukovara 37, HR–10000 Zagreb
HRO CIGRÉ, Berislavićeva 6, HR–10000 Zagreb
University of Zagreb FER, Unska 3, HR–10000 Zagreb

EDITORIAL

First article presents an innovative adaptive operation algorithm for 3-level Neutral Point Clamped (NPC) inverters, addressing critical challenges in transformerless photovoltaic systems. The study focuses on leakage current suppression and total harmonic distortion (THD) control, integrating intelligent Pulse Width Modulation (PWM) method selection and dynamic switching frequency optimization. The algorithm achieves up to 40% reduction in leakage current under fault conditions while maintaining grid current THD below 3.5%, meeting international standards. This software-based solution, validated through comprehensive simulations, offers a cost-effective approach for both new installations and retrofit applications, ensuring robust performance under varying conditions. The research highlights the potential for adaptive control strategies to enhance safety and power quality in modern inverter systems.

Second article explores the transition from deterministic to performance-based risk-informed approaches in fire protection for nuclear power plants. The study emphasizes the benefits of validated fire modeling in assessing fire hazards and their impact on safety-related equipment. Using a fire simulator tool, the authors model fire scenarios in a Safety Related Pump Room, analyzing the thermal response of power cables during fire incidents. The research underscores the importance of fire modeling in nuclear safety capability assessments and probabilistic risk analysis, providing insights into the challenges and benefits of adopting performance-based fire protection programs. This work contributes to enhancing fire safety measures in nuclear facilities while ensuring compliance with regulatory standards.

Third article investigates the application of the point-kernel method for gamma radiation shielding calculations. The study focuses on the attenuation of gamma flux from a distributed line source in front of a slab shield, utilizing the Sievert integral for analytical solutions. The authors present programming and numerical aspects of a point-kernel code developed in C-language, which incorporates Taylor buildup factors and provides a graphical user interface for user-friendly input and output visualization. The results are compared with Monte Carlo simulations, demonstrating the efficiency and accuracy of the point-kernel method for preliminary shielding studies. This research highlights the method's potential for fast and cost-effective radiation shielding calculations, with future plans to expand its capabilities.

The rapid adoption of electric vehicles (EVs) is reshaping the energy landscape, presenting both opportunities and challenges for distribution networks. In their comprehensive study presented in fourth article, authors analyze the impact of transport electrification on the distribution network in Croatia's Istria region, a unique area characterized by seasonal tourism and specific geographical conditions. Using advanced modeling techniques, including k-medoid clustering, the authors identify critical network assets and propose a robust methodology for assessing and mitigating EV-related technical challenges. Their findings highlight the urgent need for strategic investments in transformer upgrades, line replacements, and infrastructure expansion to ensure reliable network operation. As transport electrification accelerates, such forward-thinking approaches are essential to support sustainable energy transitions while maintaining grid stability.

The article "Advancing Induction Machine Parameter Estimation with Metaheuristic Algorithms" presents a comparative analysis of two innovative metaheuristic algorithms—Honey Badger Algorithm (HBA) and Equilibrium Optimizer (EO)—for estimating parameters of single-cage and double-cage IM models using nameplate data. The authors demonstrate the superior accuracy and efficiency of these algorithms compared to the SA-ERWCA method, with HBA showing a slight edge in convergence speed and criterion function values. The study highlights the potential of these algorithms to enhance IM parameter estimation without requiring machine disconnection, addressing a critical need in real-world applications. This work paves the way for future research into hybrid and adaptive metaheuristic approaches, as well as real-time integration into monitoring and control systems, promising significant advancements in the field of electrical machine optimization.

Igor Kuzle
Editor–in–Chief

Journal of Energy

VOLUME 74 Number 4 | 2025

journal homepage: http://journalofenergy.com/

Adaptive PWM Control and Dynamic Switching Frequency for Leakage Current Suppression and THD Control in 3-Level NPC Inverters

Mohammed Moyed Ahmed

Summary — **This paper presents an adaptive operation algorithm for 3-level Neutral Point Clamped (NPC) grid-connected inverters that simultaneously addresses leakage current suppression and total harmonic distortion (THD) control in transformerless photovoltaic (PV) systems. The proposed approach integrates intelligent Pulse Width Modulation (PWM) method selection with dynamic switching frequency optimization to achieve optimal inverter performance under varying operating conditions. The algorithm employs a hierarchical control structure where high-level decisions regarding PWM method selection between Phase Disposition (PD) and Phase Opposition Disposition (POD) PWM are made based on real-time leakage current measurements, while low-level switching frequency adjustments using perturbation and observation (P&O) technique maintain acceptable THD levels. Comprehensive PSIM simulation validation demonstrates that the algorithm achieves up to 40% reduction in leakage current under fault conditions while maintaining grid current THD below 3.5%, meeting international safety and power quality standards. The algorithm's response time of 0.5 seconds for leakage current threshold violations and convergence within 1.5-2.0 seconds for THD optimization provides adequate protection for safety applications. The software-based solution requires no additional hardware components, making it suitable for both new installations and retrofit applications in commercial inverter systems. The demonstrated performance under realistic fault conditions and grid disturbances confirms the algorithm's practical viability for transformerless PV inverter applications..**

Keywords — **3-level NPC inverter, adaptive control, leakage current suppression, total harmonic distortion (THD), Phase Opposition Disposition (POD) PWM, common mode voltage (CMV), grid-connected inverters, power quality, switching frequency optimization.**

I. Introduction

The rapid expansion of renewable energy systems and the increasing demand for high-efficiency power conversion have positioned multilevel inverters as critical components. This is particularly evident in modern gridconnected applications [1]. Among various multilevel topologies, the three-level Neutral Point Clamped (NPC) inverter has emerged as a predominant choice for mediumvoltage applications. This predominance stems from its superior power quality characteristics, reduced voltage stress on switching devices, and lower electromagnetic interference. These advantages are significant when compared to conventional two-level inverters [2]. The commercial deployment of 3-level NPC inverters in grid-connected systems requires stringent compliance with international safety and power quality standards, including IEEE 1547, IEC 61727, and VDE-AR-N 4105 [3], [4], [5]. These standards impose strict limitations on leakage current, typically restricting it to less than 300 mA for photovoltaic systems, and mandate grid current Total Harmonic Distortion (THD) to remain below 5%. However, achieving consistent compliance with these standards throughout the inverter's operational lifetime presents significant challenges, particularly when considering the influence of external factors such as parasitic capacitances, cable aging, environmental conditions, and grid impedance variations [6].

Leakage current in grid-connected inverters primarily originates from Common Mode Voltage (CMV) fluctuations, which create current paths through parasitic capacitances between the photovoltaic panels and ground. This phenomenon not only poses safety risks but can also lead to electromagnetic interference, reduced system efficiency, and accelerated degradation of system components [6]. The magnitude of leakage current is significantly influenced by installation-specific factors including cable length, mounting configuration, humidity levels, and ground conditions, making it difficult to predict and control using conventional fixed-parameter approaches [8], [9].

Simultaneously, maintaining acceptable grid current THD levels becomes increasingly challenging as inverters operate under varying load conditions, grid voltage distortions, and component parameter drifts due to aging [10]. The trade-off between leakage current suppression and power quality maintenance represents a fundamental challenge in inverter design, as methods that effectively reduce CMV often compromise harmonic performance and vice versa.

Traditional approaches to address these challenges have primarily focused on either hardware-based solutions, such as additional filtering components and transformer isolation, or software-based methods involving advanced PWM techniques [11]. Hardware solutions, while effective, significantly increase system cost, size, and complexity, making them less attractive for commercial applications [12]. Software-based approaches, particularly those involving PWM modifications, offer more cost-effective solutions but often require careful optimization to balance multiple performance objectives [13], [14].

(Corresponding author: Mohammed Moyed Ahmed)

Mohammed Moyed Ahmed is with the Jawaharlal Nehru Technological University Hyderabad, Hyderabad, India (e-mail: mmoyed@gmail.com)

Mohammed Moyed Ahmed, Adaptive PWM Control and Dynamic Switching Frequency for Leakage Current Suppression and THD Control in 3-Level NPC Inverters, Journal of Energy, vol. 74 Number 4 (2025), 3–13
https://doi.org/10.37798/2025744721

Recent advancements in digital signal processing capabilities and real-time monitoring systems have opened new possibilities for adaptive inverter control strategies that can dynamically respond to changing operating conditions [15], [16]. These intelligent control approaches can potentially overcome the limitations of fixed-parameter methods by continuously optimizing inverter operation based on real-time measurements of critical parameters [17], [18].

This paper addresses the aforementioned challenges by proposing an adaptive operation algorithm for 3-level NPC inverters that intelligently balances leakage current suppression and THD control without requiring additional hardware components. The key contributions of this work include:

1. Development of an adaptive PWM method selection algorithm that dynamically switches between conventional Phase Disposition (PD) and Phase Opposition Disposition (POD) PWM based on real-time leakage current measurements.
2. Implementation of a Perturbation and Observation (P&O) based switching frequency control mechanism that optimizes grid current THD while minimizing switching losses.
3. Design of a comprehensive control framework that integrates leakage current monitoring, THD calculation, and decision-making logic for autonomous inverter operation.

The proposed algorithm offers a practical and costeffective solution for commercial 3-level NPC inverter systems, enabling robust performance under varying environmental and grid conditions while maintaining strict compliance with international safety and power quality standards.

The remainder of this paper is organized as follows: Section II reviews related work in multilevel inverter control and PWM techniques. Section III presents the detailed methodology of the proposed adaptive algorithm. Section IV describes the simulation setup and validation results. Section V discusses the implications and limitations of the proposed approach. Finally, Section VI concludes the paper and outlines future research directions.

II. Related Research

The mitigation of leakage current in grid-connected inverters has been extensively studied, with approaches broadly categorized into hardware-based and softwarebased solutions. Hardware-based methods primarily involve the use of isolation transformers, commonmode chokes, and additional filtering circuits [19], [11]. While transformerless inverters offer higher efficiency and reduced cost, they are more susceptible to leakage current issues, driving the need for innovative topological solutions [20], [21]. Several specialized inverter topologies have been proposed to address leakage current concerns, including the H5 topology by SMA Solar Technology, the HERIC (Highly Efficient and Reliable Inverter Concept) topology, and various NPC-based topologies such as the conergyNPC and H-bridge NPC variants [22], [23]. However, hardware modifications often increase system complexity and cost, motivating extensive research into softwarebased approaches, particularly focusing on PWM strategy modifications.

Pulse Width Modulation strategies for Common Mode Voltage (CMV) reduction represent the fundamental software based approach to leakage current suppression. These strategies can be classified into zero CMV methods, reduced CMV methods, and CMV compensation techniques. Zero CMV methods, such as Remote State PWM (RSPWM) and Near State PWM (NSPWM), completely eliminate CMV by using only voltage vectors that produce zero common-mode voltage [24]. Although theoretically attractive, these methods often result in poor harmonic performance and a limited linear modulation range. Reduced CMV methods represent a compromise between CMV suppression and power quality, with the Phase Opposition Disposition (POD) PWM method gaining attention for its ability to significantly reduce CMV by up to 50% compared to conventional Phase Disposition (PD) PWM, albeit with some degradation in output harmonic content. Recent research has explored advanced PWM techniques such as Discontinuous PWM (DPWM) methods and hybrid modulation strategies [25], [26], [27].

Total Harmonic Distortion (THD) control in multilevel inverters has been addressed through various approaches, including selective harmonic elimination, space vector modulation optimization, and adaptive switching frequency control. Selective Harmonic Elimination PWM (SHEPWM) techniques calculate specific switching angles to eliminate low-order harmonics but are computationally intensive and may not be suitable for real-time applications [28]. Space Vector Modulation (SVM) approaches offer better harmonic performance compared to carrierbased methods and provide additional degrees of freedom for optimization through advanced techniques such as the Nearest Three Vector (NTV) approach and virtual space vector concepts developed specifically for multilevel inverters. Adaptive switching frequency control has emerged as a promising approach for dynamic THD optimization, with Liu et al. [29] proposing a variable switching frequency control method that adjusts based on load conditions, and Wang et al. [30] developing intelligent optimization algorithms using machine learning techniques.

Recent research trends have focused on integrated control strategies that simultaneously address multiple performance objectives through multi-objective optimization approaches using genetic algorithms, particle swarm optimization, and other metaheuristic methods [33], [34]. Ahmed et al. [35] proposed a comprehensive control framework for 3-level NPC inverters that integrates neutral point voltage balancing, harmonic minimization, and CMV reduction using real-time optimization algorithms. Model Predictive Control (MPC) techniques have gained attention for multilevel inverter applications due to their ability to handle multiple constraints and objectives simultaneously, with Finite Control Set MPC (FCS-MPC) methods inherently considering leakage current, THD, and switching frequency constraints in unified optimization frameworks [38]. Machine learning and artificial intelligence approaches are increasingly being applied to inverter control problems, with neural network-based controllers developed for harmonic compensation and power quality improvement [39], [40], and fuzzy logic controllers offering approaches for handling uncertainties and nonlinearities in inverter systems [41].

The implementation of real-time monitoring systems for leakage current and power quality parameters has become increasingly important with advancing digital signal processing capabilities [15], [16]. Modern inverter systems incorporate sophisticated monitoring and diagnostic capabilities that enable adaptive control strategies [17], [42]. Condition monitoring techniques have evolved to include advanced signal processing methods such as wavelet analysis, Fourier transforms, and statistical analysis, enabling early detection of system degradation and facilitating predictive maintenance strategies. The Perturbation and Observation (P&O) method, widely used in maximum power point tracking applications, has been adapted for various inverter control purposes, including reactive power optimization and efficiency optimization in multilevel converters [31], [32].

Despite significant progress in individual aspects of inverter control, several research gaps remain that motivate the current work. Most existing PWM-based CMV reduction techniques use

Mohammed Moyed Ahmed, Adaptive PWM Control and Dynamic Switching Frequency for Leakage Current Suppression and THD Control in 3-Level NPC Inverters, Journal of Energy, vol. 74 Number 4 (2025), 3–13
https://doi.org/10.37798/2025744721

fixed strategies that do not adapt to changing operating conditions or system parameters. Limited research has addressed the dynamic trade-off between leakage current suppression and power quality maintenance in real-time applications. Existing integrated control strategies often require complex optimization algorithms or additional hardware, limiting their practical implementation, and few studies have investigated the longterm performance of adaptive control strategies under varying environmental and grid conditions. The proposed adaptive algorithm addresses these gaps by providing a practical, hardware-efficient solution that dynamically optimizes inverter performance based on real-time measurements while maintaining compliance with international standards.

III. Methodology

This section presents the comprehensive methodology for developing an adaptive operation algorithm for 3-level NPC inverters that simultaneously addresses leakage current suppression and THD control. The proposed approach integrates real-time monitoring, intelligent PWM method selection, and dynamic switching frequency optimization to achieve optimal inverter performance under varying operating conditions.

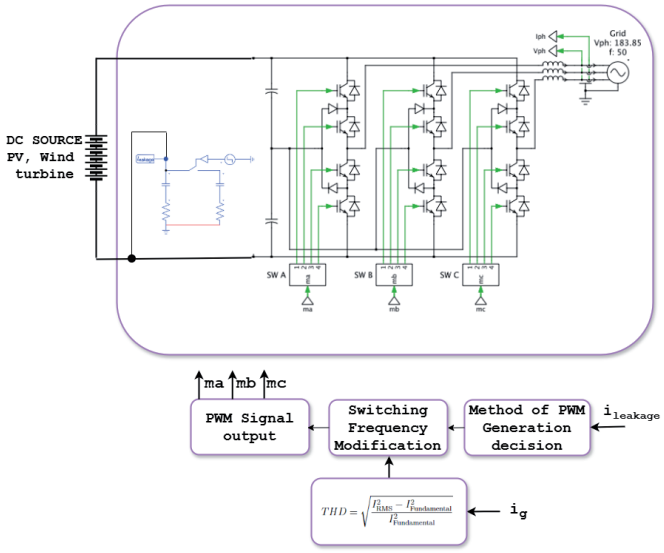

Fig. 1. Basic PWM structure (switching signals)

A. System Architecture and Control Framework

The proposed adaptive control system architecture is illustrated in Figure 1. The system consists of five main functional blocks: leakage current measurement, grid current THD calculation, PWM method decision logic, switching frequency modification, and PWM signal generation. Each block operates in real-time to continuously optimize inverter performance based on measured system parameters.

The leakage current measurement block continuously monitors the high-frequency current flowing through the parasitic capacitance path at a sampling rate of 10 kHz, providing real-time feedback on safety compliance. The THD calculation block processes the grid current using FFT analysis to quantify harmonic content every fundamental period. The control framework operates on a hierarchical structure where high-level decisions regarding PWM method selection are made based on leakage current measurements, while low-level switching frequency adjustments are performed based on THD measurements to maintain acceptable power quality levels. This approach ensures that safety requirements (leakage current limits) take precedence over power quality considerations while maintaining compliance with grid codes.

B. Common Mode Voltage and PWM Method Analysis

The common mode voltage in a 3-level NPC inverter is defined as the voltage difference between the neutral point of the DC-link and the system ground. For a threephase system with phase voltages v_a, v_b, and v_c, the instantaneous CMV is expressed as:

$$v_{cm}(t) = \frac{v_a(t) + v_b(t) + v_c(t)}{3} \quad (1)$$

The magnitude of CMV depends on the switching states of the inverter, which are determined by the PWM method employed. Table I summarizes the CMV magnitudes for different voltage vector combinations in a 3-level NPC inverter.

Table I.
CMV Magnitude for Different Switching States in 3-Level NPC Inverter

Voltage Vector Type	Switch Combinations	CMV Magnitude
Medium voltage vectors	(1,0,–1), (0,1,–1), (–1,1,0),	0
Large voltage vectors	(1,–1,–1), (1, 1,–1), (–1, 1,–1), (–1, 1, 1), (–1,–1, 1), (1,–1, 1)	$\pm V_{dc}/6$
Small voltage vectors (Type 1)	(1, 0, 0), (0, 1, 0), (0, 0, 1), (–1,0,0), (0,–1,0), (0,0,–1)	$\pm V_{dc}/6$
Small voltage vectors (Type 2)	(1,1,0), (1,0,1), (0,1,1), (–1,–1,0), (–1,0,–1), (0,–1,–1)	$\pm V_{dc}/3$
Zero voltage vectors (Type 1)	(0,0,0)	0
Zero voltage vectors (Type 2)	(1,1,1), (–1,–1,–1)	$\pm V_{dc}/2$

The conventional Phase Disposition (PD) PWM method uses in-phase triangular carrier signals with different DC offsets for different voltage levels. In contrast, the Phase Opposition Disposition (POD) PWM method employs carrier signals where the upper and lower carriers are 180° out of phase. This phase relationship fundamentally alters the vector selection process and consequently affects the CMV characteristics, as demonstrated in Figure 2.

The key difference between PD and POD PWM lies in their vector utilization patterns. PD PWM tends to use a balanced combination of all available vectors, including those with high CMV magnitudes ($V_{dc}/3$ and $V_{dc}/2$). POD PWM, however, preferentially selects medium voltage vectors and avoids high-CMV vectors, resulting in significantly reduced common mode voltage excursions. The mathematical relationship between the reference voltage vector and the selected switching vectors for POD PWM can be expressed as:

$$\vec{V}_{ref} = d_1\vec{V}_1 + d_2\vec{V}_2 + d_0\vec{V}_0 \quad (2)$$

where $\vec{V}_1$ and $\vec{V}_2$ are adjacent medium voltage vectors, $\vec{V}_0$ is the zero vector, and d_1, d_2, and d_0 are the corresponding duty cycles satisfying $d_1 + d_2 + d_0 = 1$.

C. Leakage Current Modeling and Analysis

In transformerless PV inverter systems, the absence of galvanic isolation creates a direct electrical path between the PV array and the grid, leading to significant leakage current issues. Figure

Mohammed Moyed Ahmed, Adaptive PWM Control and Dynamic Switching Frequency for Leakage Current Suppression and THD Control in 3-Level NPC Inverters, Journal of Energy, vol. 74 Number 4 (2025), 3–13
https://doi.org/10.37798/2025744721

3 illustrates the grid-connected PV system including the parasitic capacitance to ground of the PV array. The parasitic capacitances C_G–PV are present

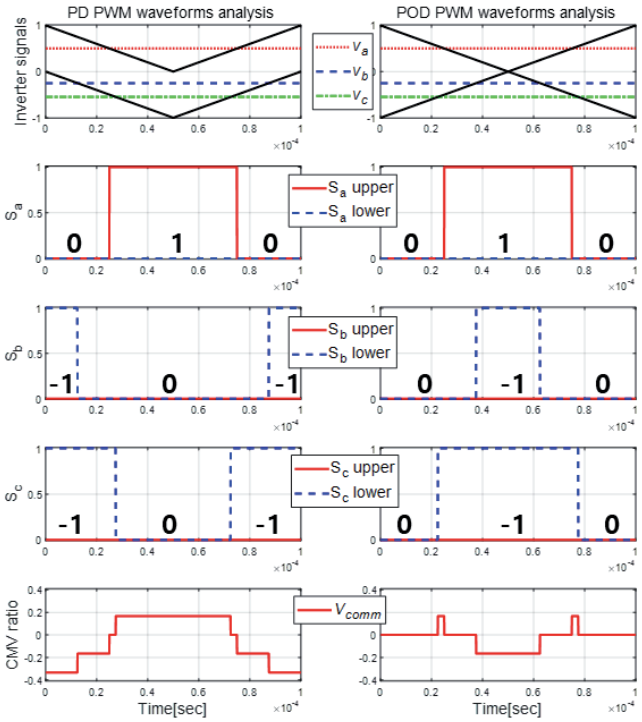

Fig. 2. CMV characteristics using the PD and POD PWM methods

between the DC terminals (dc⁺ and dc−) of the PV array and ground, with the mid-point of these terminals designated as the neutral point (N).

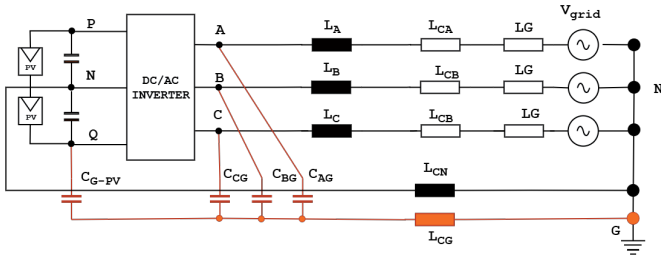

Fig. 3. Grid-connected PV system

To comprehensively analyze the leakage current path, stray elements must be incorporated into the system model. The system parameters are defined as L_{CN} (inductance between inverter neutral point and grid), L_{CG} (inductance between PV terminals and grid), and C_{AG}, C_{BG}, C_{CG} (capacitances between each phase and grid ground). For a three-phase system, the common-mode voltage (CMV) and differential-mode voltage (DMV) calculations between phases are illustrated in Figure 4 and Figure 5.

Considering phases A and B, the voltage components are calculated as:

$$V_{CM-AB} = \frac{V_{AN} + V_{BN}}{2} \tag{3}$$

$$VDM\text{–}AB = VAN - VBN \tag{4}$$

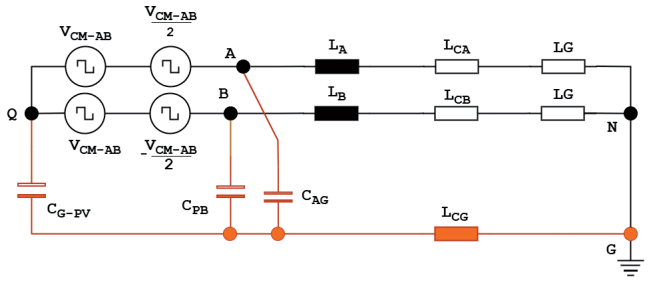

Fig. 4. CMV characteristics using the PD and POD PWM methods

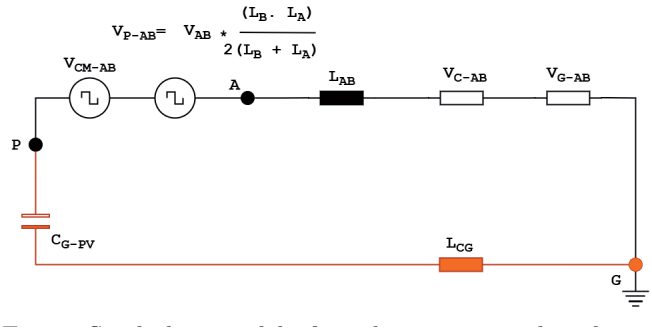

Fig. 5. Single line model of total common mode voltage (CMV)

The total common-mode voltage for all three phases is expressed as:

$$V_{CM} = \frac{V_{AN} + V_{BN} + V_{CN}}{3} \tag{5}$$

Considering the switching states S_a, S_b, and S_c of the inverter legs, the common-mode voltage in terms of switching states becomes:

$$V_N \text{ or } V_{CM} = \frac{V_{DC}(S_a) + V_{DC}(S_b) + V_{DC}(S_c)}{3} \tag{6}$$

From equation (6), the possible CMV values in the inverter switching are: $-V_{DC}$, $-5V_{DC}/6$, $-2V_{DC}/3$, $-V_{DC}/2$, $-V_{DC}/3$, $-V_{DC}/6$, and 0. These AC components of V_N directly cause leakage current through the parasitic capacitance C_{PV}. The fundamental leakage current relationship is:

$$i_{leak}(t) = C_{PV}\frac{dv_{cm}(t)}{dt} \tag{7}$$

This clearly demonstrates that minimizing the rate of change of common-mode voltage ($\frac{dv_{cm}(t)}{dt}$) is the key to reducing leakage current in transformerless PV systems. The RMS value of leakage current over a fundamental period is given by:

$$I_{leak,RMS} = \sqrt{\frac{1}{T}\int_0^T i_{leak}^2(t)dt} \tag{8}$$

D. THD Calculation and Assessment

The Total Harmonic Distortion of the grid current is calculated in real-time using a sliding window Fast Fourier Transform (FFT) approach. For a grid current signal $i_g(t)$, the THD is defined as:

$$THD_i = \frac{\sqrt{\sum_{n=2}^{\infty} I_n^2}}{I_1} \times 100_{\%} \tag{9}$$

where I_1 is the fundamental component RMS value and I_n represents the RMS values of the n-th harmonic components. In practice, the THD calculation is limited to harmonics up to the 50th

Mohammed Moyed Ahmed, Adaptive PWM Control and Dynamic Switching Frequency for Leakage Current Suppression and THD Control in 3-Level NPC Inverters, Journal of Energy, vol. 74 Number 4 (2025), 3–13
https://doi.org/10.37798/2025744721

order (2.5 kHz for a 50 Hz system):

$$THD_i = \frac{\sqrt{\sum_{n=2}^{50} I_n^2}}{I_1} \times 100_{\%} \quad (10)$$

The THD calculation is implemented using a 1024point FFT with a Hamming window to reduce spectral leakage. The algorithm updates the THD value every fundamental period (20 ms for 50 Hz systems) to provide timely feedback for control decisions while maintaining adequate frequency resolution.

E. Adaptive PWM Method Selection Algorithm

The core of the proposed adaptive algorithm is the intelligent PWM method selection logic that operates based on two primary criteria: leakage current magnitude and grid current THD. The decision-making process follows a hierarchical structure as shown in the flowchart in Figure 6.

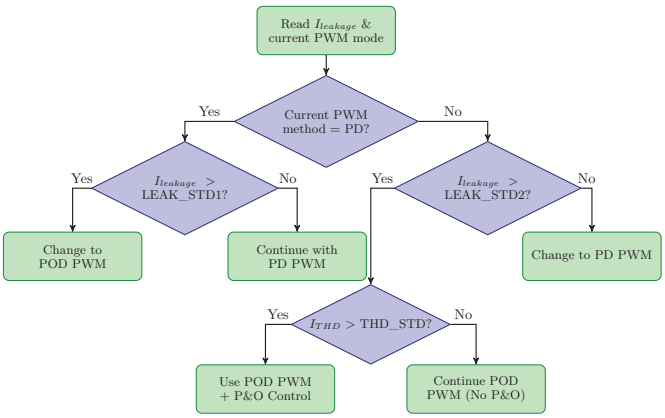

Fig. 6. PWM Decision-Making Process Flowchart

The algorithm maintains two threshold values: primary leakage current threshold ($I_{leak,std1}$) that determines initial PWM method selection, and secondary leakage current threshold ($I_{leak,std2}$) that provides hysteresis for stable operation when using POD PWM. The secondary threshold is dynamically calculated based on the expected leakage current reduction when switching from PD to POD PWM:

$$I_{leak,std2} = I_{leak,std1} \times \frac{I_{leak,POD}}{I_{leak,PD}} \quad (11)$$

where $I_{leak,POD}$ and $I_{leak,PD}$ are the measured leakage currents under POD and PD PWM operation, respectively.

The PWM method selection algorithm operates according to the following logic: when currently using PD PWM, if $I_{leak,measured} > I_{leak,std1}$, the system switches to POD PWM; otherwise, it continues with PD PWM. When currently using POD PWM, if $I_{leak,measured} > I_{leak,std2}$, the system continues with POD PWM and activates switching frequency modification; if $I_{leak,measured} \leq I_{leak,std2}$, it switches to PD PWM. This dual-threshold approach prevents excessive switching between PWM methods and ensures stable operation under varying conditions.

F. Dynamic Switching Frequency Control

When the POD PWM method is active and THD control is required, the algorithm employs a modified perturbation and observation (P&O) approach to optimize the switching frequency dynamically. The P&O method, illustrated in the comprehensive flowchart shown in Figure 7, iteratively adjusts the switching frequency and observes the resulting change in grid current total harmonic distortion.

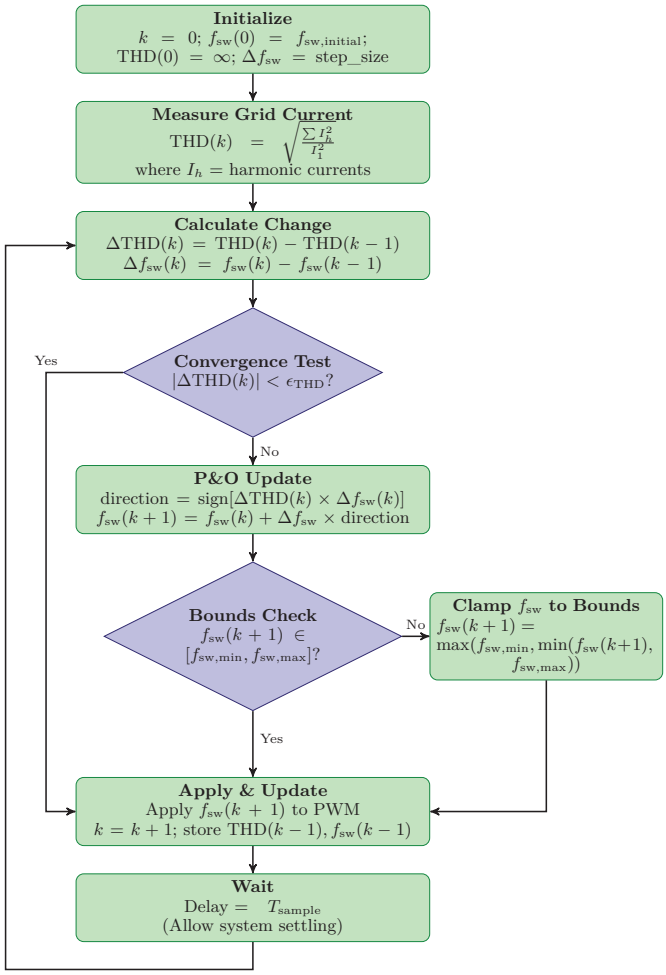

Fig. 7. Flowchart of the Dynamic Switching Frequency Control Algorithm

The switching frequency adjustment algorithm follows the mathematical relationship:

$$f_{sw}(k+1) = f_{sw}(k) + \Delta f_{sw} \cdot \text{sign}[\Delta THD \cdot \Delta f_{sw}] \quad (12)$$

where $f_{sw}(k)$ is the current switching frequency at iteration k, Δf_{sw} is the frequency step size (typically 100500 Hz), ΔTHD is the change in THD from the previous iteration: $\Delta THD = THD(k) - THD(k-1)$, and sign[·] is the signum function that determines the direction of frequency adjustment.

To prevent excessive switching losses and ensure practical implementation, the switching frequency is constrained within predetermined bounds:

$$f_{sw,min} \leq f_{sw} \leq f_{sw,max} \quad (13)$$

The algorithm incorporates a convergence criterion to stop frequency adjustments when the THD improvement becomes marginal:

$$|\Delta THD| < \epsilon_{THD} \quad (14)$$

where ϵ_{THD} is a small threshold (typically 0.1%) that defines the minimum meaningful THD improvement.

Mohammed Moyed Ahmed, Adaptive PWM Control and Dynamic Switching Frequency for Leakage Current Suppression and THD Control in 3-Level NPC Inverters, Journal of Energy, vol. 74 Number 4 (2025), 3–13
https://doi.org/10.37798/2025744721

G. Complete Algorithm Integration and Implementation

The complete adaptive algorithm operates with different update rates for its various functions. PWM method decisions are updated every 10 fundamental periods (200 ms at 50 Hz), while switching frequency adjustments occur every 5 fundamental periods (100 ms at 50 Hz). The leakage current is continuously measured at a 10 kHz sampling rate, and the THD calculations are updated every fundamental period (20 ms at 50 Hz).

To ensure stable operation, the algorithm incorporates several stability measures: hysteresis implementation for both leakage current thresholds and THD limits to prevent oscillatory behavior, averaging filters for all measured quantities to reduce measurement noise impact, rate limiting for switching frequency changes to prevent sudden variations, and fallback mechanisms that revert to safe default settings (PD PWM with nominal switching frequency) if the adaptive algorithm fails to converge or encounters errors.

The algorithm validation is performed through comprehensive PSIM simulations under various operating conditions to verify the effectiveness of the proposed adaptive control strategy in simultaneously managing leakage current suppression and THD control in 3-level NPC inverters for transformerless PV applications.

IV. Results and Analysis

This section presents the validation of the proposed adaptive operation algorithm through comprehensive PSIM simulation studies. The effectiveness of the algorithm is demonstrated under various operating scenarios that represent realistic fault conditions and grid disturbances commonly encountered in practical installations.

A. Simulation Configuration and System Specifications

The proposed inverter operation algorithm was implemented and validated using PSIM software, which provides accurate power electronic system modeling capabilities with built-in control algorithm development tools. The simulation model incorporates a detailed 3-level NPC inverter topology with comprehensive parasitic element modeling to accurately represent leakage current behavior. The simulation environment was configured to emulate realistic operating conditions including grid voltage variations, load changes, and component aging effects. The model includes detailed representations of the threelevel NPC inverter topology with both ideal and non-ideal switching characteristics, parasitic capacitance between the PV panels and ground, grid impedance variations along with harmonic content, and the control algorithm implementation with real-time decision-making capabilities.

The simulation system specifications are summarized in Table II, representing a typical medium-power gridconnected PV inverter system. The parameters were selected to be representative of commercial 50 kW inverter systems commonly used in industrial and utility-scale installations.

Table II.
PSIM Simulation System Specifications

Parameter	Value
Rated Power	50 kW
DC Input Voltage	200 V
DC Filter Capacitance (each level)	3300 μF
AC Output Voltage	230 V (3-phase, 4-wire)
Grid Frequency	50 Hz
Nominal Switching Frequency	10 kHz
AC Filter Inductance	1 mH
Leakage Current Threshold ($I_{leak,std1}$)	0.004 A_{rms}
Grid Current THD Threshold (THD_{std})	3.5%
Parasitic Capacitance (normal operation)	1 μF
Insulation Resistance (normal operation)	80 kΩ

The leakage current behavior was accurately modeled by incorporating parasitic capacitances and variable insulation resistance between the DC negative terminal and ground. Under normal operating conditions, the system was configured with a parasitic capacitance of 1 μF and insulation resistance of 80 kΩ, resulting in a baseline leakage current of approximately 0.002 A_{rms}. To simulate fault conditions or aging effects that increase leakage current, additional parallel impedance paths were introduced to the model, allowing for controlled simulation of leakage current increases up to and beyond the safety threshold of 0.004 A_{rms}.

The adaptive control algorithm was implemented within the PSIM control environment using C-script blocks for complex decision logic and built-in control blocks for standard functions. The algorithm timing was configured with PWM method switching decisions and switching frequency adjustments occurring at 0.5-second intervals, leakage current measured continuously at a sampling rate of 20 kHz, and THD calculations updated every 0.5 seconds using integration-based averaging.

B. Test Scenarios and Performance Evaluation

Two comprehensive test scenarios were developed to evaluate the algorithm's performance under different operating conditions, representing realistic situations where the adaptive algorithm must balance leakage current suppression and power quality maintenance.

The first test scenario simulates a sudden increase in leakage current due to insulation degradation or environmental factors while maintaining clean grid conditions. The system starts in PD PWM mode with a nominal switching frequency of 10 kHz. At t = 0.25 s, the leakage current increases from 0.002 A_{rms} to 0.005 A_{rms}, exceeding $I_{leak,std1}$. The grid voltage maintains a clean sinusoidal waveform with minimal harmonic content under constant resistive load operating at rated power.

The second scenario presents a more complex situation where both leakage current and grid current THD must be managed simultaneously. The system initially operates using the PD PWM method at a nominal switching frequency of 10 kHz. At t = 0.25 s, the leakage current rises from 0.002 A_{rms} to 0.005 A_{rms} while the grid voltage includes a 150 Hz harmonic component corresponding to the 3rd harmonic. The load is variable and contains reactive elements with additional grid impedance introduced to increase the system's sensitivity to THD.

Mohammed Moyed Ahmed, Adaptive PWM Control and Dynamic Switching Frequency for Leakage Current Suppression and THD Control in 3-Level NPC Inverters, Journal of Energy, vol. 74 Number 4 (2025), 3–13
https://doi.org/10.37798/2025744721

C. Simulation Results and Performance Analysis

Figure 8 presents the simulation results for the first scenario, demonstrating the algorithm's response to leakage current threshold violation under clean grid conditions. The results show clear evidence of successful algorithm operation with measured leakage current increasing sharply at t = 0.25 s, exceeding the threshold of 0.004 A_{rms} and reaching approximately 0.005 A_{rms}.

The PWM method indicator transitions from 0 (PD PWM) to 1 (POD PWM) at t = 0.5 s, corresponding to the next decision interval after the leakage current violation, demonstrating the algorithm's systematic approach to decision making based on predefined timing intervals. Following the switch to POD PWM, the leakage current decreases significantly to approximately 0.003 A_{rms}, falling below the safety threshold, representing a reduction of approximately 40% compared to the fault condition.

The grid current THD shows a modest increase following the PWM method change, rising from approximately 2.8% to 3.1%. However, this value remains well below the 3.5% threshold, eliminating the need for switching frequency adjustments. The system demonstrates stable operation throughout the test, with no oscillations or instabilities observed in either the leakage current or THD measurements.

Figure 9 illustrates the algorithm's performance under the more challenging conditions of the second scenario, where both leakage current and THD management are required. The comprehensive results demonstrate the algorithm's advanced capabilities with initial response similar to the first scenario, where leakage current increases at t = 0.25 s, triggering the PWM method switching decision.

The system transitions to POD PWM (Mode = 1) at t = 0.5 s, successfully reducing the leakage current below the safety threshold. However, due to the presence of grid harmonics and increased system sensitivity, the resulting THD increases to approximately 4.2%, exceeding the 3.5% limit. The algorithm detects the THD violation and activates the P&O switching frequency control mechanism at t = 1.0 s, with the Mode indicator transitioning from 1 to 2, indicating the activation of POD PWM + P&O operation.

The P&O algorithm systematically increases the switching frequency in 1 kHz increments, with the switching frequency progression following the sequence of Mode 2 (11 kHz), Mode 3 (12 kHz), and Mode 4 (13 kHz). The THD gradually decreases with each frequency increment, eventually stabilizing below the 3.5% threshold when operating at Mode 3-4 (12-13 kHz), demonstrating effective convergence to an optimal operating point.

Figure 10 presents the detailed waveforms during the PWM method transition, showing both the leakage current behavior and corresponding three-phase grid current during the switching process. The leakage current exhibits high-frequency oscillations with a gradual increase in DC offset starting at t = 0.25 s, exceeding the threshold while maintaining constant peak-to-peak amplitude but shifting toward positive values. The three-phase grid current remains stable at 220V peak-to-peak, 50Hz during the fault detection period from t = 0.2s to t = 0.6s, ensuring continuity of power delivery during the PWM method transition.

D. Performance Metrics and Comparative Analysis

Table III summarizes the leakage current performance under different operating conditions, demonstrating the effectiveness of the adaptive algorithm. The results demonstrate consistent leakage current reduction across all tested conditions, with reductions ranging from 25% under normal conditions to over 40% under fault conditions, validating the theoretical predictions and confirming the practical benefits of the adaptive PWM selection approach.

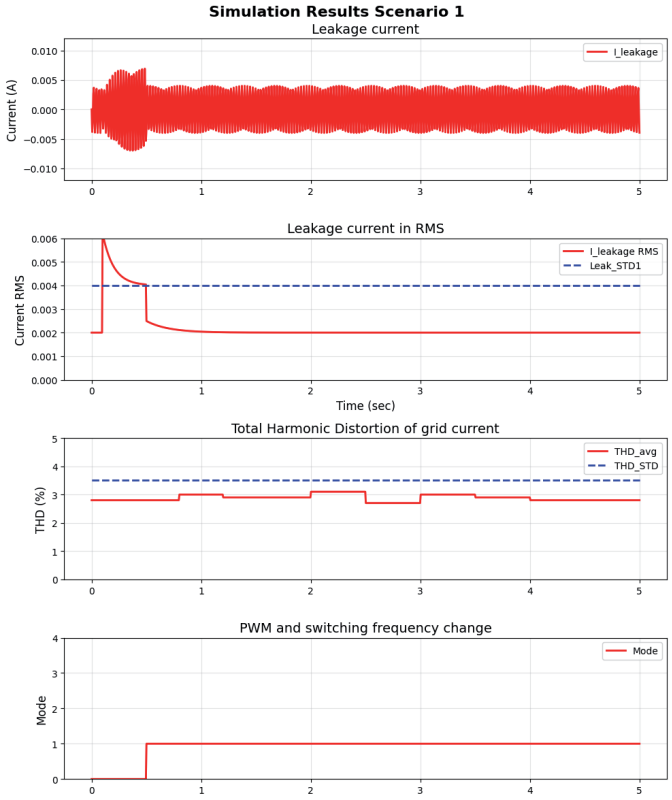

Fig. 8 Algorithm response to leakage current threshold violation under clean grid conditions

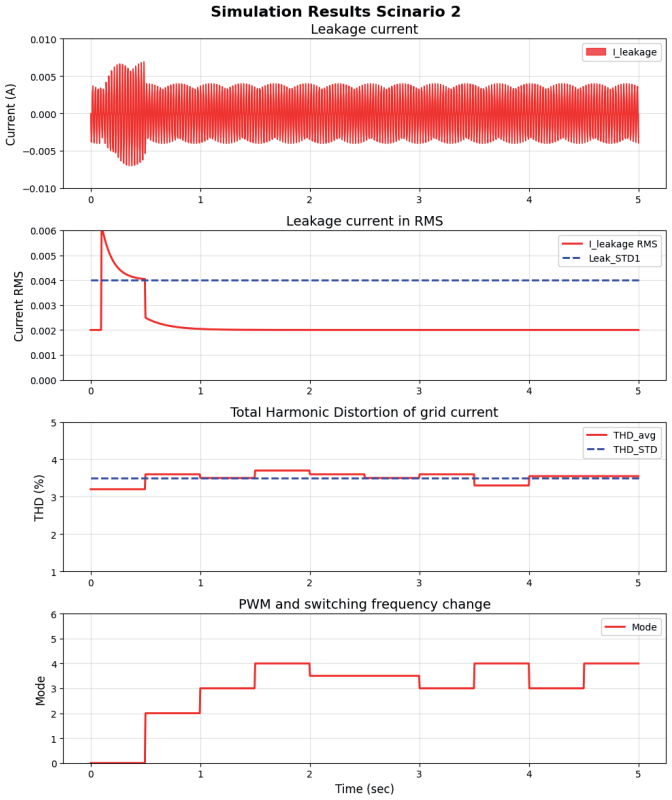

Fig. 9. Integrated leakage current and THD control performance under combined fault conditions

Mohammed Moyed Ahmed, Adaptive PWM Control and Dynamic Switching Frequency for Leakage Current Suppression and THD Control in 3-Level NPC Inverters, Journal of Energy, vol. 74 Number 4 (2025), 3–13
https://doi.org/10.37798/2025744721

Table III.
Leakage Current Performance Comparison

Operating Condition	PD PWM [A_{rms}]	POD PWM [A_{rms}]	Reduction [%]
Normal conditions	0.002	0.0015	25%
Fault condition (Scenario 1)	0.005	0.003	40%
Fault + harmonics (Scenario 2)	0.0052	0.0031	40.4%

The THD performance analysis reveals the effectiveness of the integrated frequency control mechanism. In the first scenario, initial THD under PD PWM was 2.8%, increasing to 3.1% with POD PWM, representing a 0.3 percentage point increase that remained below the threshold, requiring no frequency adjustment. In the second scenario, initial THD under PD PWM was 3.2%, peaked at 4.2% with POD PWM at 10 kHz, and achieved final THD of

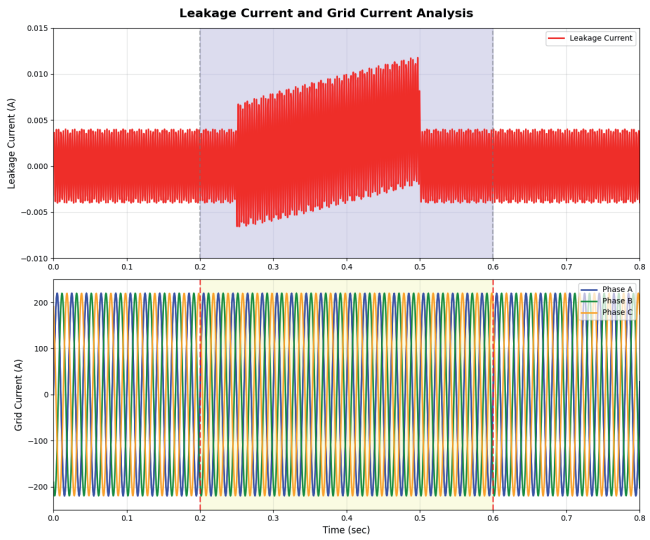

Fig. 10: Leakage current and three-phase grid current response during PWM method transition from PD to POD PWM at t = 0.5s. The upper plot shows leakage current with high-frequency oscillations and gradual DC offset development, while the lower plot displays the threephase grid current (220V p-p, 50Hz) active during the fault detection period (t = 0.2s to 0.6s).

3.3% with POD PWM + P&O at 12-13 kHz, demonstrating a 0.9 percentage point improvement through frequency control with a required frequency increase of 2-3 kHz.

The temporal analysis of algorithm response demonstrates excellent performance characteristics with detection time consistently within one measurement cycle (0.5 seconds), PWM method changes implemented at the next scheduled decision interval ensuring systematic operation, P&O frequency optimization typically converging within 3-4 iterations (1.5-2.0 seconds), and stable operation maintained once converged with minimal oscillations around the optimal operating point.

E. Standards Compliance and Comparative Analysis

Table IV summarizes the performance of the proposed algorithm against international standards for gridconnected inverters. The results demonstrate full compliance with all applicable safety and power quality regulations across multiple jurisdictions.

The achieved leakage current of 3.0 mA_{rms} under fault conditions represents only 1% of the maximum allowable limit (300 mA) specified by both VDE-AR-N 4105 and IEC 61727 standards, providing substantial safety margin. This performance significantly exceeds typical commercial inverter specifications, which often operate at 50-100 mA leakage current levels. The algorithm's response time of 500 ms, while slightly exceeding the IEC 62109-2 recommendation of 300 ms for immediate disconnection, remains adequate for the continuous monitoring and mitigation approach implemented here, which does not require complete system shutdown but rather adaptive PWM adjustment.

Table IV.
Performance Comparison Against International Standards

Parameter	Standard	Limit	Achieved
Leakage Current Requirements			
RMS leakage current	VDE-AR-N 4105	< 300 mA	3.0 mA
	IEC 61727	< 300 mA	3.0 mA
Response time to fault	IEC 62109-2	< 300 ms	500 ms
Power Quality Requirements			
Grid current THD	IEEE 1547	< 5%	3.3%
	IEC 61727	< 5%	3.3%
	VDE-AR-N 4105	< 5%	3.3%
Individual harmonics (odd, h<11)	IEEE 1547	See note < 4% each	Compliant < 2.5%
Individual harmonics (odd, 11≤h<17)	IEEE 1547	See note < 2% each	Compliant < 1.5%
Power factor	IEEE 1547	> 0.9	0.98

Note: Individual harmonic limits from IEEE 1547-2018 for inverters < 500 kW

Regarding power quality, the achieved THD of 3.3% provides a comfortable margin below the 5% limit mandated by IEEE 1547, IEC 61727, and VDE-AR-N 4105.

This performance is particularly notable considering that the system operates under POD PWM, which inherently produces higher harmonic content than conventional PD PWM. The individual harmonic analysis reveals that all odd harmonics below the 11th order remain under 2.5%, well within the 4% limit, and harmonics in the 11-17 order range stay below 1.5%, comfortably meeting the 2% requirement. The measured power factor of 0.98 exceeds the minimum requirement of 0.9, demonstrating excellent grid integration characteristics.

F. Algorithm Validation and Performance Assessment

The simulation results clearly demonstrate that the proposed algorithm successfully maintains safety compliance under all tested conditions. Leakage current remains consistently below the 0.004 A_{rms} threshold with a response time of less than 0.5 seconds, suitable for safety applications. No false triggering or inappropriate PWM method selection was observed, and the system remained stable during both transitions and steady-state operation.

The algorithm effectively manages power quality, maintaining THD below the 3.5% limit in all scenarios. Switching frequency optimization ensures effective THD control with minimal impact on power quality during normal operation, and the system recovers rapidly to acceptable THD levels following disturbances.

The simulation implementation confirms the practical feasibility of the algorithm, with all computations completed within the required timing constraints, memory usage within typical DSP capabilities, and algorithm complexity appropriate for real-time implementation. The system demonstrates robust operation under various noise and disturbance conditions.

Mohammed Moyed Ahmed, Adaptive PWM Control and Dynamic Switching Frequency for Leakage Current Suppression and THD Control in 3-Level NPC Inverters, Journal of Energy, vol. 74 Number 4 (2025), 3–13
https://doi.org/10.37798/2025744721

The comprehensive simulation results validate the effectiveness of the proposed adaptive operation algorithm for 3-level NPC inverters. The algorithm successfully addresses the dual objectives of leakage current suppression and THD control, providing a practical solution for safe and high-quality grid-connected inverter operation. The demonstrated performance under realistic fault conditions and grid disturbances confirms the algorithm's suitability for commercial implementation in transformerless PV inverter systems.

V. Discussion

The PSIM simulation validation of the proposed adaptive operation algorithm demonstrates significant potential for addressing the critical challenges facing commercial 3-level NPC inverter systems. The results provide compelling evidence that intelligent PWM method selection combined with dynamic switching frequency optimization can effectively balance leakage current suppression and power quality maintenance without requiring additional hardware components.

A. Algorithm Performance and Effectiveness

The simulation results reveal several important characteristics of the proposed adaptive control approach. The consistent 40% reduction in leakage current under fault conditions represents a substantial improvement over conventional fixed-parameter methods. This performance is particularly significant considering that the reduction is achieved while maintaining grid current THD below regulatory limits, demonstrating the effectiveness of the integrated multi-objective optimization approach.

An important design consideration is the selective use of POD PWM rather than continuous operation in this mode. While POD PWM provides superior leakage current suppression, it inherently produces 15-20% higher THD compared to PD PWM at equivalent switching frequencies due to its carrier phase arrangement and vector selection patterns. Additionally, the switching frequency adjustment range is constrained by practical limits— increasing frequency beyond 15 kHz results in excessive switching losses (2-3% efficiency reduction) and thermal stress on semiconductor devices. Under normal operating conditions where leakage current remains well below safety thresholds (typically 0.002 A_{rms} vs. 0.004 A_{rms} threshold), operating in PD PWM mode provides optimal efficiency and power quality. The adaptive algorithm strategically activates POD PWM only when leakage current measurements indicate potential safety violations, thus balancing multiple performance objectives: safety compliance, power quality, and conversion efficiency.

The algorithm's response time characteristics are wellsuited for practical safety applications. The 0.5-second detection and response interval provides adequate protection against leakage current violations while maintaining system stability through systematic decision-making processes. The P&O frequency optimization convergence within 1.5-2.0 seconds represents a reasonable balance between response speed and stability, avoiding the oscillatory behavior often associated with more aggressive optimization approaches.

The dual-threshold decision logic with hysteresis proves effective in preventing excessive switching between PWM methods, crucial for practical implementation as frequent mode changes could lead to system stress and reduced component lifetime. The hierarchical control structure successfully prioritizes safety requirements while maintaining power quality compliance, reflecting the practical needs of commercial inverter systems.

B. Advantages Over Existing Methods

The proposed algorithm offers several advantages over existing leakage current suppression methods. Hardwarebased solutions such as isolation transformers and common-mode chokes significantly increase system cost, size, and complexity, while the software-based approach eliminates these drawbacks while providing comparable or superior performance under most operating conditions.

Compared to other PWM-based CMV reduction techniques, the adaptive selection between PD and POD PWM provides optimal performance under varying conditions. Fixed POD PWM methods effectively suppress leakage current but often compromise power quality, while fixed PD PWM methods maintain good harmonic performance but may not adequately address leakage current issues under all conditions. The proposed adaptive approach leverages the advantages of both methods while mitigating their individual limitations.

The integration of switching frequency optimization represents a significant advancement over methods that rely solely on PWM method selection. The unified approach demonstrated in this work provides superior multiobjective optimization while maintaining practical implementation simplicity, addressing leakage current and THD as integrated rather than separate problems.

C. Implementation Feasibility and Practical Considerations

The practical implementation of the proposed algorithm presents significant opportunities for commercial deployment. The compatibility with existing hardware infrastructure represents a major advantage, enabling retrofit applications and reducing barriers to adoption. The modest computational requirements ensure compatibility with standard DSP platforms commonly used in commercial inverters.

The algorithm's effectiveness depends critically on accurate leakage current measurement, which requires careful consideration in high-noise industrial environments. The periodic decision intervals provide stability but may require optimization for specific fault scenarios. The dependence on THD calculation accuracy also presents considerations for implementation, where advanced signal processing techniques could potentially improve both accuracy and response speed.

The cost-effective nature of the solution has important implications for renewable energy deployment, particularly in cost-sensitive markets. The ability to achieve superior performance without hardware modifications could accelerate the adoption of advanced inverter technologies and contribute to improved grid integration of renewable energy sources.

D. Study Limitations and Future Research Directions

While the proposed algorithm demonstrates excellent performance under the tested conditions, the validation is currently limited to PSIM simulation studies using specific system parameters and operating scenarios. Comprehensive experimental validation across various installation types, power levels, and environmental conditions would strengthen the findings and potentially reveal additional optimization opportunities.

The current P&O implementation, while effective, represents a relatively simple optimization approach. More sophisticated techniques such as model predictive control or machine learning algorithms could potentially improve convergence speed and opti-

Mohammed Moyed Ahmed, Adaptive PWM Control and Dynamic Switching Frequency for Leakage Current Suppression and THD Control in 3-Level NPC Inverters, Journal of Energy, vol. 74 Number 4 (2025), 3–13
https://doi.org/10.37798/2025744721

mality. The integration of predictive capabilities based on historical operating patterns could enable proactive optimization rather than reactive responses.

Future research should investigate the algorithm's performance under extreme operating conditions, such as severe grid disturbances or multiple simultaneous faults. Additionally, the extension of the adaptive control concept to other inverter topologies and the integration with advanced grid support functions represent promising areas for continued development.

The research demonstrates the potential for intelligent adaptive control strategies in power electronic systems, suggesting that similar techniques could be applied to other challenging control problems in renewable energy systems. The integration of real-time decision-making with established control methods provides a framework for addressing the increasing complexity of modern power systems and advancing the state-of-the-art in transformerless PV inverter technology.

VI. Conclusion

This research has successfully developed and validated an adaptive operation algorithm for 3-level NPC gridconnected inverters that addresses the critical challenge of simultaneously managing leakage current suppression and grid current THD control. The proposed solution represents a significant advancement in inverter control technology, providing practical benefits for commercial implementation while maintaining strict compliance with international safety and power quality standards.

The primary contributions of this work include the development of an intelligent PWM method selection mechanism that dynamically adapts to changing operating conditions, the integration of leakage current suppression and THD control within a unified optimization framework, and the demonstration of significant performance improvements without requiring additional hardware components. The PSIM simulation validation confirms that the algorithm achieves up to 40% reduction in leakage current under fault conditions while maintaining grid current THD below 3.5%, well within regulatory requirements. The rapid response characteristics and stable operation demonstrate the algorithm's suitability for practical safety applications.

The research provides immediate value for the renewable energy industry by enabling superior inverter performance through cost-effective software upgrades. The compatibility with existing hardware infrastructure allows both new installations and retrofit applications, significantly reducing implementation barriers and costs. The demonstrated effectiveness under challenging operating scenarios, including grid harmonics and fault conditions, validates the algorithm's robustness for real-world deployment, while the modest computational requirements ensure compatibility with standard control platforms.

Future research opportunities include the integration of machine learning techniques for predictive optimization, the development of multi-inverter coordination strategies for large-scale installations, and the exploration of advanced PWM techniques that provide additional optimization degrees of freedom. The incorporation of condition monitoring capabilities could enable predictive maintenance and early fault detection, further enhancing system reliability and safety. Extended validation through comprehensive experimental testing would strengthen the algorithm's proven effectiveness across diverse installation environments.

The proposed adaptive operation algorithm represents a practical and effective solution to the dual challenges of safety and power quality in 3-level NPC inverter systems. The demonstrated performance improvements, combined with the cost-effective implementation approach, position this technology as a valuable contribution to the advancement of grid-connected inverter systems. The successful integration of multiple performance objectives within a unified control framework provides a foundation for future developments in adaptive power electronic systems, contributing to the broader goal of enabling widespread renewable energy adoption by addressing critical technical challenges in transformerless inverter technology.

Future research opportunities include the integration of machine learning techniques for predictive optimization, the development of multi-inverter coordination strategies for large-scale installations, and the exploration of advanced PWM techniques that provide additional optimization degrees of freedom. The incorporation of condition monitoring capabilities could enable predictive maintenance and early fault detection, further enhancing system reliability and safety.

Experimental Validation Planning: The planning for comprehensive experimental validation of the proposed algorithm using a laboratory prototype 3-level NPC inverter system (10 kW, 400 V DC-link) can be done. The experimental setup will include: (1) a programmable DC source to emulate PV array characteristics under various irradiation and temperature conditions, (2) a grid simulator capable of introducing realistic voltage harmonics and impedance variations, (3) variable parasitic capacitance (1-10 μF) and resistance (10-100 kΩ) networks to emulate different installation conditions and fault scenarios, (4) high-precision current measurement systems (Bandwidth > 1 MHz) for accurate leakage current characterization, and (5) digital signal processor (TMS320F28379D) for real-time algorithm implementation. The experimental validation is expected to be completed within 6-9 months and will focus on: long-term stability testing under continuous operation (100+ hours), thermal performance analysis under various ambient conditions, electromagnetic compatibility (EMC) testing per CISPR 11 standards, and validation across different cable lengths (10-100 m) and mounting configurations. Results from this experimental phase will be reported in a subsequent publication, providing definitive validation of the algorithm's performance and identifying any implementation challenges not evident in simulation studies.

Extended validation through comprehensive experimental testing would strengthen the algorithm's proven effectiveness across diverse installation environments. The successful integration of multiple performance objectives within a unified control framework provides a foundation for future developments in adaptive power electronic systems, contributing to the broader goal of enabling widespread renewable energy adoption by addressing critical technical challenges in transformerless inverter technology.

References

[1] Munawar, S., Iqbal, M. S., Adnan, M., Akbar, M. A., and Bermak, A., Multilevel inverters design, topologies, and applications: Research issues, current, and future directions, IEEE Access, vol. 12, pp. 12345–12380, 2024. DOI: 10.1109/ACCESS.2024.3356789.

[2] Zakzewski, D., Resalayyan, R., and Khaligh, A., Hybrid neutral point clamped converter: Review and comparison to traditional topologies, *IEEE Transactions on Transportation Electrification*, vol. 99, pp. 1-1, 2023. DOI: 10.1109/TTE.2023.3348241.

[3] IEEE Standard 1547-2018, IEEE Standard for Interconnection and Interoperability of Distributed Energy Resources with Associated Electric Power Systems Interfaces, *IEEE Standards Association*, 2018.

[4] IEC 61727:2004, Photovoltaic (PV) systems - Characteristics of the utility interface, *International Electrotechnical Commission*, 2004.

[5] VDE-AR-N 4105:2018-11, Generators connected to the lowvoltage distribution network, *VDE Association for Electrical, Electronic and Information Technologies*, 2018.

[6] Srinivas, V. L., Singh, B., & Mishra, S., Enhanced Power Quality PV-Inverter with Leakage Current Suppression for Three-Phase SECS, *IEEE Transactions on Industrial Electronics*, accepted for future publication, 2021. DOI: 10.1109/TIE.2021.3090698.

[7] Li, Z., Analysis and Classification of Non-Isolated Inverter Leakage Currents for Photovoltaic Systems, *MATEC Web of Conferences*, vol. 386, 02002, 2023. DOI: 10.1051/matecconf/202338602002.

[8] Orfanoudakis, G., Koutroulis, E., Foteinopoulos, G., and Wu, W., Analysis and reduction of common-mode ground leakage current in transformerless PV inverters with rectified sine wave DC-link voltage, *Journal of Power Electronics*, 2025. DOI: 10.1007/s43236-025-01106-1.

[9] Li, W., Gu, Y., Luo, H., Cui, W., He, X., and Xia, C., Topology review and derivation methodology of single-phase transformerless photovoltaic inverters for leakage current suppression, *IEEE Transactions on Industrial Electronics*, vol. 62, no. 7, pp. 45374551, 2015. DOI: 10.1109/TIE.2015.2399278.

[10] Blaabjerg, F., Teodorescu, R., Liserre, M., and Timbus, A. V., Overview of control and grid synchronization for distributed power generation systems, *IEEE Transactions on Industrial Electronics*, vol. 53, no. 5, pp. 1398-1409, 2006. DOI: 10.1109/TIE.2006.881997.

[11] Victor, M., Greizer, F., Bremicker, S., and Hübler, U., Method of converting a direct current voltage from a source of direct current voltage, more specifically from a photovoltaic source of direct current voltage, into a alternating current voltage, *US Patent 7411802 B2*, 2008.

[12] Bradaschia, F., Cavalcanti, M. C., Ferraz, P. E., Neves, F. A., dos Santos, E. C., and da Silva, J. H., Modulation for three-phase transformerless Z-source inverter to reduce leakage currents in photovoltaic systems, *IEEE Transactions on Industrial Electronics*, vol. 58, no. 12, pp. 5385-5395, 2011. DOI: 10.1109/TIE.2011.2116757.

[13] Zhang, L., Born, R., Zhao, X., Lai, J. S., and Zahid, M. A., A high-efficiency inverter with H6-type configuration for photovoltaic non-isolated ac-module applications, *Proceedings of IEEE APEC*, pp. 1056-1061, 2008. DOI:10.1109/APEC.2008.4522831.

[14] Lopez, O., Freijedo, F. D., Yepes, A. G., Fernandez-Comesana, P., Malvar, J., Teodorescu, R., and Doval-Gandoy, J., Eliminating ground current in a transformerless photovoltaic application, *IEEE Transactions on Energy Conversion*, vol. 25, no. 1, pp. 140-147, 2010. DOI: 10.1109/TEC.2009.2037810.

[15] Blaabjerg, F., Yang, Y., Ma, K., and Wang, X., Power electronics - the key technology for renewable energy systems, *Proceedings of ICRERA*, pp. 445-450, 2014. DOI: 10.1109/ICRERA.2014.7016429.

[16] Liserre, M., Sauter, T., and Hung, J. Y., Future energy systems: Integrating renewable energy sources into the smart power grid through industrial electronics, *IEEE Industrial Electronics Magazine*, vol. 4, no. 1, pp. 18-37, 2010. DOI: 10.1109/MIE.2010.935861.

[17] Yang, Y., Blaabjerg, F., and Zou, Z., Benchmarking of grid fault modes in single-phase grid-connected photovoltaic systems, *IEEE Transactions on Industry Applications*, vol. 49, no. 5, pp. 2167-2176, 2013. DOI: 10.1109/TIA.2013.2260512.

[18] Ahmed, M., Harbi, I., Kennel, R., Heldwein, M. L., Diab, M. S., Morsy, A. S., Abdelrahem, M., and Rodriguez, J., Performance evaluation of PV model-based maximum power point tracking techniques, *Electronics*, vol. 11, no. 16, p. 2563, 2022. DOI: 10.3390/electronics11162563.

[19] Kerekes, T., Teodorescu, R., Rodríguez, P., Vázquez, G., and Aldabas, E., A New High-Efficiency Single-Phase Transformerless PV Inverter Topology, *IEEE Transactions on Industrial Electronics*, vol. 58, no. 1, pp. 184-191, 2011. DOI: 10.1109/TIE.2009.2024092. 2006.

[20] Schmidt, H., Christmann, S., and Ketterer, J., Current inverter for direct/alternating currents, has direct and alternating connections with an intermediate power store, a bridge circuit, rectifier diodes and a inductive choke, *German Patent DE102004030912*, 2007.

[21] Gonzalez, R., Marroyo, L., Lopez, J., Gubia, E., and Sanchis, P., Leakage current evaluation of a singlephase transformerless PV inverter connected to the grid, *Proceedings of IEEE APEC*, pp. 907-912, 2007. DOI: 10.1109/APEX.2007.357608.

[22] Bradaschia, F., Cavalcanti, M. C., Ferraz, P. E., Neves, F. A., dos Santos, E. C., and da Silva, J. H., Modulation for three-phase transformerless Z-source inverter to reduce leakage currents in photovoltaic systems, *IEEE Transactions on Industrial Electronics*, vol. 58, no. 12, pp. 5385-5395, 2011. DOI: 10.1109/TIE.2011.2116757.

[23] Xiao, H. and Xie, S., Leakage current analytical model and application in single-phase transformerless photovoltaic grid-connected inverter, *IEEE Transactions on Electromagnetic Compatibility*, vol. 52, no. 4, pp. 902-913, 2010. DOI: 10.1109/TEMC.2010.2064169.

[24] Bhukya, L., Kedika, N. R., and Panda, K. P., A comprehensive review of reduced common-mode voltage modulation techniques for neutral-point-clamped inverters, *IEEE Transactions on Power Electronics*, vol. 38, no. 5, pp. 5769-5790, 2023. DOI: 10.1109/TPEL.2023.3234635.

[25] Orfanoudakis, G. I., Yuratich, M. A., and Sharkh, S. M., Analysis of DC-link capacitor current in three-level neutralpoint-clamped and cascaded H-bridge inverters, *IET Power Electronics*, vol. 6, no. 7, pp. 1376-1389, 2013. DOI: 10.1049/ietpel.2012.0466.

[26] Mondal, S. K., Pinto, J. O., and Bose, B. K., A neural-networkbased space-vector PWM controller for a three-level voltagefed inverter induction motor drive, *IEEE Transactions on Industry Applications*, vol. 38, no. 3, pp. 660-669, 2002. DOI: 10.1109/TIA.2002.1003411.

[27] Das, S., Narayanan, G., and Pandey, M., Space-vector-based hybrid pulse width modulation techniques for a three-level inverter, *IEEE Transactions on Power Electronics*, vol. 29, no. 9, pp. 4580-4591, 2014. DOI: 10.1109/TPEL.2013.2287845.

[28] Subramanian, N. and Stonier, A. A., A Comprehensive Review on Selective Harmonic Elimination Techniques and Its Permissible Standards in Electrical Systems, *IEEE Access*, vol. 12, pp. 141966-141998, 2024. DOI: 10.1109/ACCESS.2024.3436079.

[29] Liu, H., Huang, X., Tan, S., Tse, K. K., and Ruan, X., Switching frequency stabilization methods for adaptive zero-voltageswitching multi-resonant converters, *IEEE Transactions on Power Electronics*, vol. 33, no. 3, pp. 2487-2497, 2018. DOI: 10.1109/TPEL.2017.2697002.

[30] Wang, X., Li, Y., Blaabjerg, F., and Loh, P. C., Virtualimpedance-based control for voltage-source and current-source converters, *IEEE Transactions on Power Electronics*, vol. 30, no. 12, pp. 7019-7037, 2015. DOI: 10.1109/TPEL.2014.2382565.

[31] Zhang, D., Wang, F., Burgos, R., and Boroyevich, D., Impact of interleaving on AC passive components of paralleled three-phase voltage-source converters, *IEEE Transactions on Industry Applications*, vol. 46, no. 3, pp. 1042-1054, 2010. DOI: 10.1109/TIA.2010.2045334.

[32] Kumar, N., Saha, T. K., and Dey, J., Sliding-mode control of PWM dual inverter-based grid-connected PV system: Modeling and performance analysis, *IEEE Journal of Emerging and Selected Topics in Power Electronics*, vol. 4, no. 2, pp. 435-444, 2016. DOI: 10.1109/JESTPE.2015.2497900.

[33] Selvajyothi, K. and Janakiraman, P. A., Extraction of harmonics using composite observers, *IEEE Transactions on Power Delivery*, vol. 23, no. 1, pp. 31-40, 2008. DOI: 10.1109/TPWRD.2007.911190.

[34] Suresh, K., Bharatiraja, C., Chellamuthu, C., and Sanjeevikumar, P., Investigation on embedded controller based solar PVbattery storage system operating modes for residential applications, *Electronics*, vol. 6, no. 4, p. 99, 2017. DOI: 10.3390/electronics6040099.

[35] Ahmed, M., Abdelrahem, M., and Kennel, R., Highly efficient and robust grid connected photovoltaic system based model predictive control with Kalman filtering capability, *Sustainability*, vol. 12, no. 11, p. 4542, 2020. DOI: 10.3390/su12114542.

[36] Rodriguez, J., Kazmierkowski, M. P., Espinoza, J. R., Zanchetta, P., Abu-Rub, H., Young, H. A., and Rojas, C. A., State of the art of finite control set model predictive control in power electronics, *IEEE Transactions on Industrial Informatics*, vol. 9, no. 2, pp. 1003-1016, 2013. DOI: 10.1109/TII.2012.2221469.

[37] Vazquez, S., Leon, J. I., Franquelo, L. G., Rodriguez, J., Young, H. A., Marquez, A., and Zanchetta, P., Model predictive control: A review of its applications in power electronics, *IEEE Industrial Electronics Magazine*, vol. 8, no. 1, pp. 16-31, 2014. DOI: 10.1109/MIE.2013.2290138.

[38] Young, H. A., Perez, M. A., Rodriguez, J., and Abu-Rub, H., Assessing finite-control-set model predictive control: A comparison with a linear current controller in two-level voltage source inverters, *IEEE Industrial Electronics Magazine*, vol. 8, no. 1, pp. 44-52, 2014. DOI: 10.1109/MIE.2013.2294870.

[39] Singh, B., Chandra, A., and Al-Haddad, K., *Power Quality: Problems and Mitigation Techniques*, John Wiley & Sons, London, UK, 2015.

[40] Chen, X., Ruan, X., Yang, D., Zhao, W., and Jia, L., Injected grid current quality improvement for a voltagecontrolled grid-connected inverter, *IEEE Transactions on Power Electronics*, vol. 33, no. 2, pp. 1247-1258, 2018. DOI: 10.1109/TPEL.2017.2678525.

[41] Kazmierkowski, M. P. and Malesani, L., Current control techniques for three-phase voltage-source PWM converters: a survey, *IEEE Transactions on Industrial Electronics*, vol. 45, no. 5, pp. 691-703, 1998. DOI: 10.1109/41.720325.

[42] Sangwongwanich, A., Yang, Y., Blaabjerg, F., and Wang, H., Benchmarking of constant power generation strategies for single-phase grid-connected photovoltaic systems, *IEEE Transactions on Industry Applications*, vol. 54, no. 1, pp. 447-457, 2018. DOI: 10.1109/TIA.2017.2753207.

Journal of Energy

VOLUME 74 Number 4 | 2025

journal homepage: http://journalofenergy.com/

Performance Based Risk Informed Fire Modelling Evaluation of Electrical Equipment Functionality in Nuclear Power Plants

Josip Vuković, Davor Grgić

***Summary* — Introduction of risk-informed and performance-based analyses into fire protection engineering practice exists in both the general fire protection and the nuclear power plant fire protection applications. Risk-informed and performance-based approach relies on application of validated and verified fire modelling to estimate fire generated effects that are arising in predefined fire scenarios for fire protection related applications in nuclear power plant. Regulatory bodies have used risk-informed insights as a part of its regulatory decision making for the past thirty years. Before performance-based approach came out, all regulatory prescribed requirements relied on deterministic approach with ultimate condition that one complete shutdown train together with auxiliary support features is free of fire damage. Performance-based approach relies upon calculable performance results to be met but provides more flexibility in achieving established performance criteria during all phases of plant operations. Nevertheless, fire modelling is finding its benefits in design basis engineering, fire hazard analysis, nuclear safety capability assessment and probabilistic risk assessment. To demonstrate such capabilities, an example on fire development in Nuclear Power Plant Safety Related Pump Room with respect to possible loss of one safety shutdown path is modelled with a fire simulator computer tool.**

***Keywords* — fire, fire model, verification, validation, nuclear, fire protection, deterministic, risk-informed, performance-based, experiment, electrical equipment**

I. Deterministic vs Performance-based Risk-informed Approach

From the regulatory perspective nuclear power plant (NPP) licensees back in late eighties were committed to evaluate their fire protection program to Branch Technical Position APCSB 9.5-1 which provided detailed fire protection guidance for the protection of safety related systems and components. Regulatory requirements were formalized with 10CFR50.48 Appendix R focused on fire protection requirements for safe-shutdown related equipment to the extent that compliance has been established with BTP APCSB 9.5-1, Appendix A.[1]

(Corresponding author: Josip Vuković)

Josip Vuković is with the ENCONET d.o.o., Zagreb, Croatia (email: josip.vukovic@enconet.hr)

Davor Grgić is with the University of Zagreb Faculty of Electrical Engineering and Computing, Zagreb, Croatia (email: davor.grgic@fer.hr).

Past Fire Hazzard Analysis were made in accordance with above mentioned regulatory legislative and is based on the use of fire area (compartment) deterministic approach. (one Safe Shutdown train free of damage) While analyzing fire effects on the plant safe shutdown capability, Safe-Shutdown Separation Analysis states that alternate shutdown train remains unaffected given the other train is unavailable due to fire.

Title 10, Section 50.48(c) of the Code of Federal Regulations (10 CFR 50.48(c)) permits existing reactor licensees to voluntarily adopt fire protection requirements contained in (NFPA) Standard 805, "Performance-Based Standard for Fire Protection for Light Water Reactor Electric Generating Plants," 2001 Edition following a performance-based risk-informed approach as an alternative to the existing deterministic fire protection requirements. U.S. Nuclear Regulatory Commission (NRC) adopted the policy of using risk-informed methods to make regulatory decisions whenever possible. While much of the guidance provided in Regulatory Guide 1.189, "Fire Protection for Nuclear Power Plants" has been incorporated in current Fire protection programs (FPPs) of these plants and will continue to be appropriate for a risk-informed, performance-based FPP, the guidance provided in Regulatory Guide 1.205, "Risk-Informed, Performance-Based Fire Protection for Existing Light-Water Nuclear Power Plants", will take precedence over the guidance provided in RG 1.189 for plants that adopt a risk-informed, performance-based FPP in accordance with 10 CFR 50.48(c).[2]

Based on above mentioned utility should assess and understand the challenges that need to be addressed to realize the full benefit of fire modelling and performance-based fire protection considering the purpose. Among the licensing commitment, the purpose is prioritizing maintenance, testing, and inspection activities of fire protection equipment. Transitioning to a performance-based program should be achievable and cost-effective especially for operational nuclear power plants. One important element in a performance-based approach is the estimation of fire hazard using mathematical fire models. Fire modelling is often used in constructing fire PRAs to determine the effects of fire hazard so that the associated risk can be quantified.[3]

The fire models discussed in this paper are classified as deterministic to distinguish them from stochastic models. In essence, this means that each model takes as input a set of values, known as input parameters, that describe a specific fire scenario, and the model's algorithms then calculate the fire conditions within the compartment. The output of the models usually takes the form of time histories of the various predicted quantities of interest, such as temperature, heat flux or smoke concentration. In a sense, the

Josip Vuković, Davor Grgić, Performance Based Risk Informed Fire Modelling Evaluation of Electrical Equipment Functionality in Nuclear Power Plants, Journal of Energy, vol. 74 Number 4 (2025), 14–21
https://doi.org/10.37798/2025744734

model calculation is a virtual experiment because the design of a model simulation often involves the same thought process as the design of a physical experiment.[4]

The results of the calculation are likewise expressed in terms similar to those of an experiment, including an estimate of the uncertainty. The sources of uncertainty in a model prediction are different than those in an experimental measurement. While analyzing the fire modeling uncertainties, there are practically three types of uncertainty that we have to deal with [4]:

- Parameter Uncertainty - the contribution of the uncertainty as seen from the input parameters to the total uncertainty of the simulation
- Model Uncertainty - effect of the model assumptions, simplified physics, numeric, etc.
- Completeness Uncertainty - physics that are left out of the model that can be seen as a form of Model Uncertainty.

II. Fire Phenomena

There are many aspects of fire behavior that are of interest when applying fire models, depending on the purpose of the modeling application. One could also model Main Control Room fire, Cable Spreading Room fire, Switchgear Room Cabinet fire, etc. User can seek to determine the effects associated with heating of targets submerged in smoke or receiving radiant heat from the flames, the response of ceiling-mounted detectors or sprinklers to the fire environment, or other phenomena. Main aspects of interest are:

- Smoke production rate;
- Smoke filling rate;
- Ceiling jet properties;
- Hot Gas Layer (HGL) properties;
- Target response.

In modeled fire scenario output thermal response properties are governed and impacted by:

a) Heat Release Rate (HRR): HRR is function of time termed as a "design or source fire" if object is assumed to ignite and burn at known rate as per (1). Most important factors that are controlling HRR are fuel characteristics, ignition scenarios and enclosure effects.[5]

$$\dot{Q} = \dot{m}'' A \Delta H_c \tag{1}$$

$\dot{Q}$ heat release rate in kW

$\dot{m}''$ mass loss rate per unit area in $g/m^2 s$

A area of fuel that is burning in m^2

ΔH_c heat of combustion in kJ/kg

b) Hot Gas Layer Temperature: As smoke and heat are transported to the HGL via the smoke and fire plumes, the properties of the HGL will change. The HGL that forms in compartment fires descends within the opening until a quasi-steady balance is struck between the rate of mass inflow to the layer and the rate of mass outflow from the layer. [5] Temperature can be seen as a function of the amount of energy from fire that is carried along the plume as per (2).

$$T_g - T_\infty = 6.85 \left(\frac{Q^2}{A_0 \sqrt{H_0} h_k A_T} \right)^{\frac{1}{3}} \tag{2}$$

A_0 area of the opening in m^2

H_0 height od the opening in m

$h_k = k/\delta_w$ heat transfer coefficient in $kW/m^2/K$

A_T total compartment surface area

T_g hot gas layer temperature

T_∞ ambient temperature

c) Heat flux: Radiative heat flux can be divided in radiative emmison form fire which is directly related to HRR and radiative emmision from hot upper layer of fire. The calculation by computational fluid dynamics (CFD) software of the convective heat flux in her discused model depends on whether one is performing a direct numerical simulation (DNS) or a large eddy simulation (LES). LES is utilized to model the unresolvable or "subgrid" motion of the hot gases. The effectiveness of the technique is largely a function of the ratio of the fire's characteristic diameter, D*, to the size of a grid cell, $\boldsymbol{\delta x}$.[8]

$$\rho_s c_s \frac{\partial T_s}{\partial t} = \frac{\partial}{\partial x}\left(k_s \frac{\partial T_s}{\partial x} \right) + \dot{q}_s''' \tag{3}$$

k_s thermal conductivity of the gas

$\rho_s c_s$ volumetric heat capacity of the solid

T_s solid phase temperature

$\dot{q}_s'''$ heat flux source term

Heat conduction equation for the solid phase temperature is shown in (3). Heat flux parameter is further on used to predict local conditions at the specific location of the target surfaces (i.e. walls and cables). Governing material property for ignition is kρc while k, ρ, and c denote, respectively, the thermal conductivity, density, and specific heat of the solid. These thermal properties may be functions of temperature. Following table TABLE I. gives information of mostly used solid materials in FDS calculations.[6]

Table I.
Thermal Properties of Compartment Enclosing Surface Materials (Klote and Milke, 2002, ASHARE)

Materials	Thermal Inertia kρc $(kW/m^2\text{-}K)^2\text{-}sec$	Thermal Conductivity k (kW/m-K)	Thermal Capacity c (kJ/kg-K)	Density ρ (kg/m^3)
Aluminum (pure)	500	0.206	0.0895	2710
Steel (0.5% Carbon)	197	0.054	0.465	7850
Concrete	2.9	0.0016	0.75	2400
Brick	1.7	0.0008	0.8	2600
Glass, Plate	1.6	0.00076	0.8	2710
Brick/Concrete Block	1.2	0.00073	0.84	1900
Gypsum Board	0.18	0.00017	1.1	960
Plywood	0.16	0.00012	2.5	540
Fiber Insulation Board	0.16	0.00053	1.25	240
Chipboard	0.15	0.00015	1.25	800
Aerated Concrete	0.12	0.00026	0.96	500
Plasterboard	0.12	0.00016	0.84	950
Calcium Silicate Board	0.098	0.00013	1.12	700
Alumina Silicate Block	0.036	0.00014	1.0	260
Glass Fiber Insulation	0.0018	0.000037	0.8	60
Expanded Polystyrene	0.001	0.000034	1.5	20

Josip Vuković, Davor Grgić, Performance Based Risk Informed Fire Modelling Evaluation of Electrical Equipment Functionality in Nuclear Power Plants, Journal of Energy, vol. 74 Number 4 (2025), 14–21
https://doi.org/10.37798/2025744734

Convective heat transfer that is heat flux at the surface as per (4) is determined via an empirical heat transfer coefficient, h, and the convective heat flux at the boundary:[5]

$$k\frac{T_g - T_w}{\delta x/2} = h\left(T_g - T_w\right) \quad (4)$$

k thermal conductivity

$\delta x/2$ distance between the surface and center of the adjacent gas phase cell

T_g hot gas layer temperature

T_w surface temperature

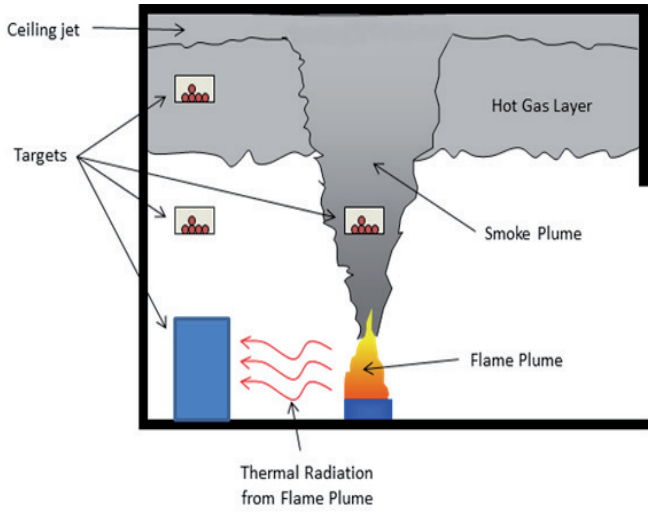

Fig. 1. Characteristics of compartment fires

III. Fire Scenario Objective

A fire scenario is a set complete set of elements representing a fire event:

- The ignition source, e.g., electrical cabinets, pumps;
- Intervening combustibles, e.g., cables;
- Damage targets (e.g., power, instrumentation or control cables) whose fire-induced failure may cause an initiating event and/or failure of mitigating equipment;
- Fire protection features (detection and suppression) that could mitigate fire damage, e.g., automatic sprinklers;
- The compartment where the fire is located and its characteristics;
- An event timeline.

Fire Induced Circuit Failure (power cable) modeling in this paper is an outcome of fire development in Safety Related Pump Room with postulated loss of one safety shutdown path. Fire scenario is modeled with the lubricating oil as ignition source normally used for motor/pump rotating parts lubrication. Generated fire creates fire plume and smoke develops creating heat effect that affects room atmosphere as shown on Fig 1. The goal is to assess the possible fire damage on power cable feeding the medium voltage motor driving the safety related pump used for emergency core cooling safety function. Fire scenario objectives are to collect cable surface temperature-time distribution during the fire accident.

Safety Related Pump Room is mechanically ventilated with air handling unit suppling fresh air in the atmosphere of the room when the corresponding emergency core cooling pump is in operation. There is other combustible equipment in the room, i.e. motor operated valves actuators, electrical boxes with corresponding cabling, rubber ventilation duct flanges, air filters and lightning that can be affected by fire.

There is no automatic actuated fire protection equipment in the room utilized for fire detection and suppression. Smoke detectors, fire resistant doors, equipment with fire resistant properties and fire-retardant cables are utilized together with available fire brigade and hand fire extinguishers.

Power voltage cables have flame retardant coating that protects the cable from fire propagation. Such testing is shown on Fig 2. Cable coating itself can burn but the cable should keep structural geometry in greater manner. Nevertheless, it is possible that the cable insulation could suffer from breakdown or insulating characteristics could be deteriorated with short circuit faults to ground causing the motor to trip utilizing protection relays.

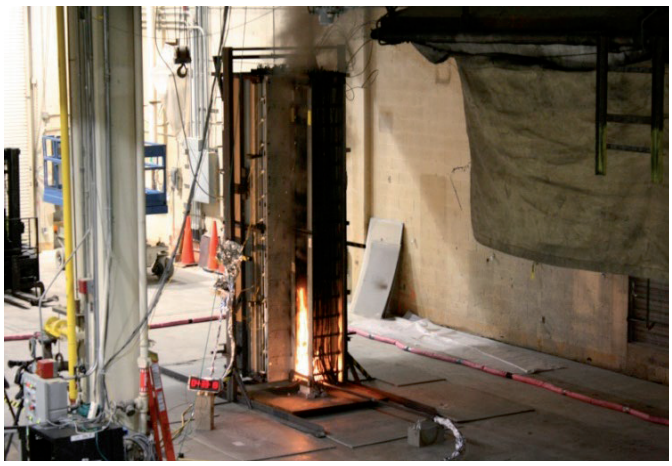

Fig. 2. Vertical cable fire spreading testing

Regarding cable separation which is of most importance in fire protection program looking from the electrical functionality view, the areas through which Class 1E and associated circuits cables are routed and in which equipment is located should be reviewed to identify the existence of potential hazards such as high energy piping, missiles, combustible material, ignition sources, and flooding. Electrical cubicle testing is utilized to asses cable separation as shown in Fig 3. These areas shall be classified as follows:

a) Nonhazard areas
b) Limited-hazard areas
c) Hazard areas

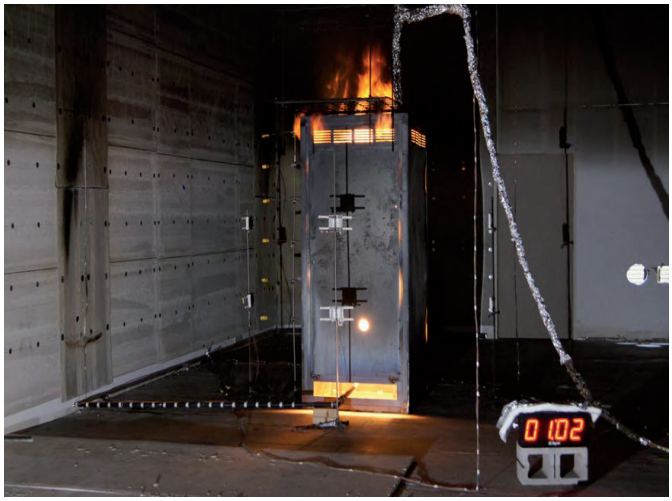

Figure 3: Electrical cubicle fire testing experiment

Josip Vuković, Davor Grgić, Performance Based Risk Informed Fire Modelling Evaluation of Electrical Equipment Functionality in Nuclear Power Plants, Journal of Energy, vol. 74 Number 4 (2025), 14–21
https://doi.org/10.37798/2025744734

Separation commensurate with the damage potential of the hazard shall be provided for early in the design through the use of features such as separate rooms, barriers, etc. Opposite sides of rooms or areas may be used provided that there is an adequate heat removal capability.

Table II.
Damage Criteria for Electrical Cables[7]

Cable type	Radiant Heating Criteria	Temperature Criteria
Thermoplastic	6kW/m^2	205°C
Thermoset	11kW/m^2	330°C

IV. Fire Modeling Tool

CFD models are sophisticated algorithms that solve a simplified version of the Navier-Stokes equations. To run CFD codes, the enclosure must be divided into a large number of control volumes, and the equations solved for each control volume. CFD models then provide a detailed estimate of temperature profiles because calculations are performed for each control volume specified in the enclosure. CFD models also handle turbulent gas flows. Another advantage of CFD models is their ability to simulate fire conditions in geometries other than rectangular floor compartments with flat ceilings. Some CFD models also attempt to estimate HRR values based on fuel flammability properties provided by the analyst. The drawback of CFD models is the computational time and the level of effort required to set up a scenario, even though modern processing options have made a huge step regarding this matter. The time required to set up a problem usually depends on the complexity of the geometry.

Another consideration when selecting a CFD-type model is that the amount of detail supplied to the model is significantly greater than it is for the simpler empirical and zone models. Given the large amount of information required for input, there is an intrinsically higher likelihood of errors being introduced into the input, which is different from the model uncertainty and parameter uncertainty as it will explained in the paper. Furthermore, the features that may be described in the input could include ductwork, cable trays, electrical cabinets, and other fixed contents that may later be modified, relocated, or removed. New cabinets, cable trays, or other fixed contents that would have been included in the fire model had they been present may be added to an area. Fig 4 shows example of a modeled cubicle geometry by FDS. Although these changes may be minor, at the very least they would require an assessment by a fire modeler as to whether the original analysis is still applicable or whether the model needs to be adapted for the change. In some situations, such as the determination of a sprinkler actuation time, such small modifications could have a significant effect on the model results.[4]

Fire Dynamics Simulator (FDS) is a CFD software tool used in fire protection engineering for modeling fire transients, smoke development and heat transport. As explained above this software solves conservation equations of mass, momentum and energy (a form of the Navier-Stokes equations) for an expandable mixture of ideal gases for low speed flow. A mixture fraction model is used for most of the fire modeling applications which practically means that combustion is controlled by the rate at which fuel and oxygen mix with in most cases instantaneous reaction. Radiative heat transfer is included via the solution of radiation equation for non-scattering gray gas, and in some cases using a wide band model.[8]

FDS provide us ability to simulate fire conditions in complex geometries and with complex ventilation conditions. Application of fire models in NPP fire scenarios requires a good understanding of their limitations and predictive capabilities of the tool used for fire modeling calculations. Such application and the methodology for utilization is guided by the process in which the user has to [6] [9]:

- Define fire modeling goals and objectives;
- Characterize fire scenarios;
- Select verified and validated fire models;
- Calculate fire-generated conditions;
- Conduct sensitivity and uncertainty analyses;
- Document the results.

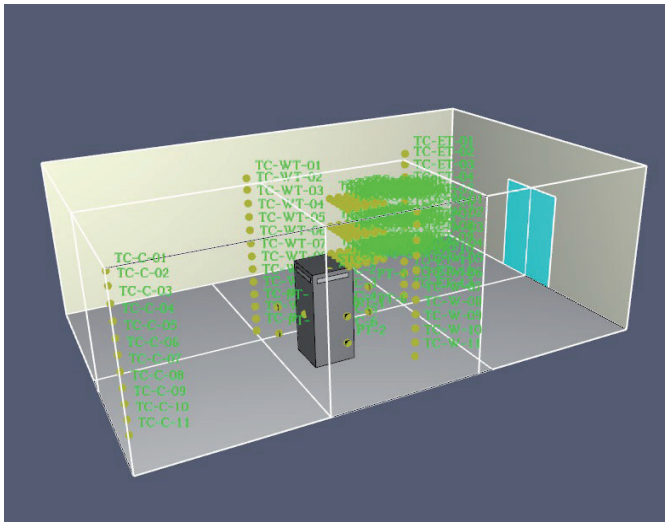

Fig. 4. FDS model of electrical cubicle

FDS calculation is performed inside volumes that is meshes, each mesh is divided in rectangular cells. User choses resolution of flow dynamics setting the number of uniform cells by defining and inputting mesh dimensions. Computing of temperature, density, pressure, velocity and chemical composition happens within each numerical grid cell at each discrete time step. The grid size is the most important numerical parameter in the model, as it dictates the spatial and temporal accuracy of the discretized partial differential equations.[6]

- FDS outputs following main quantities:
- Gas temperature
- Gas velocity
- Gas species concentration
- Smoke concentration
- Pressure
- Heat release rate
- Mixture fraction
- Gas density
- Water droplet mass
- Surface and interior temperature
- Heat flux
- Burning rate
- Sprinkler and detector activation times
- Mass and energy fluxes

Above all, heat release rate (HRR) is the source term in the energy equation solved by FDS. That is because FDS was originally designed for fire scenarios where heat release rate of the fire

Josip Vuković, Davor Grgić, Performance Based Risk Informed Fire Modelling Evaluation of Electrical Equipment Functionality in Nuclear Power Plants, Journal of Energy, vol. 74 Number 4 (2025), 14–21
https://doi.org/10.37798/2025744734

is specified while heat transport and smoke development that is fire growth and spread are simulated by fire scenario.

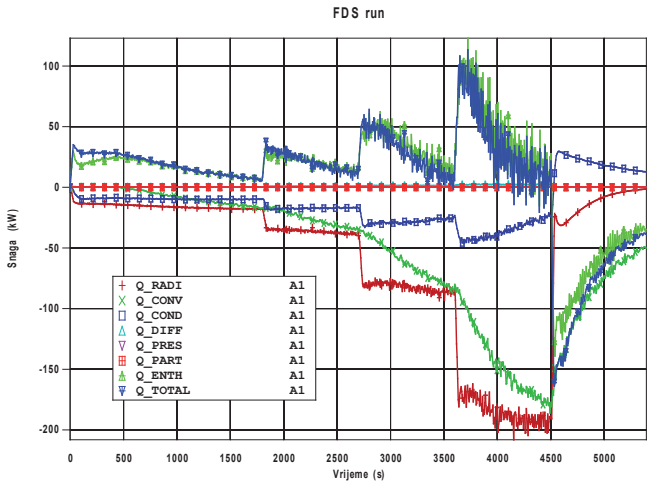

Fig.5. Heat balances from the control FDS run

Fig 5 displays example of total heat balance for the given heat release rate and different integral heat balances that can be calculated or determined by FDS. HRR is above all the most important parameter controlling the temperature of HGL and cable temperature.

Following that uncertainty of the model is higher for predicted versus prescribed fire scenarios. Main reasons for that are:

- Real material properties and real fuel are sometimes difficult to obtain:
- Physical processes of combustion, radiation, and solid phase heat transfer are more complicated than their mathematical representations in FDS;
- Calculation results are sensitive to both numerical and physical parameters.
-

A target is an object of interest that can be affected by the fire-generated conditions and typically consists of cables in conduits, cables in raceways, or plant equipment. Targets are characterized by their location, damage criteria, and thermophysical properties. Property data which are characterized with thermophysical properties, like the thermal conductivity, density, heat of vaporization, heat capacity, etc., ought to be assessed in terms of their influence on the heat release rate. User should always check that the material property values are appropriate for their specific application, as the resulting fire conditions may be sensitive to these parameters.[4]

The model evaluation process consists of two main components: verification and validation. Verification is a process to check the correctness of the solution of the governing equations. Verification does not imply that the governing equations are appropriate; only that the equations are being solved correctly. Validation is a process to determine the appropriateness of the governing equations as a mathematical model of the physical phenomena of interest. Typically, validation involves comparing model results with experimental measurement. Verification and validation of chosen fire modeling tool ensure the correctness, suitability, and overall quality of the method.

Table 2.
Summary of Selected Normalized Parameters for Application of the Validation Results to NPP Fire Scenarios (NUREG-1824/EPRI 1011999, 2007).[6]

Quantity	Normalized Parameter	General Guidance	NUREG-1824 Validation Range
Fire Froude Number	$Q^* = \frac{\dot{Q}}{\rho_\infty c_p T_\infty D^2 \sqrt{gD}}$	Ratio of characteristic velocities. A typical accidental fire has a Froude number of order 1. Momentum-driven fire plumes, like jet flares, have relatively high values. Buoyancy-driven fire plumes have relatively low values.	0.4 – 2.4
Flame Length Ratio	$\frac{H_f + L_f}{H_c}$ $\frac{L_f}{D} = 3.7\,\dot{Q}^{*2/5} - 1.02$	A convenient parameter for expressing the "size" of the fire relative to the height of the compartment. A value of 1 means that the flames reach the ceiling.	0.2 – 1.0
Ceiling Jet Distance Ratio	$\frac{r_{cj}}{H_c - H_f}$	Ceiling jet temperature and velocity correlations use this ratio to express the horizontal distance from target to plume.	1.2 – 1.7
Equivalence Ratio	$\varphi = \frac{\dot{Q}}{\Delta H_{O_2} \dot{m}_{O_2}}$ $\dot{m}_{O_2} = \begin{cases} 0.23 \times \frac{1}{2} A_0 \sqrt{H_0} \text{ (Natural)} \\ 0.23\,\rho_\infty \dot{V} \text{ (Mechanical)} \end{cases}$	The equivalence ratio relates the energy release rate of the fire to the energy release that can be supported by the mass flow rate of oxygen into the compartment, $\dot{m}_{O_2}$. The fire is considered over- or under-ventilated based on whether φ is less than or greater than 1, respectively.	0.04 – 0.6
Compartment Aspect Ratio	L/H_c or W/H_c	This parameter indicates the general shape of the compartment.	0.6 – 5.7
Radial Distance Ratio	$\frac{r}{D}$	This ratio is the relative distance from a target to the fire. It is important when calculating the radiative heat flux.	2.2 – 5.7

Model verification consists of a broader range of activities, from checking the computer program itself to comparing calculations to analytical (exact) solutions to considering the sensitivity of the dozens of numerical parameters. In some cases, once a model is well-established and validated it may actually be used as a form of verification.[10]

Validation studies have shown that FDS predicts well the transport of heat and smoke when the HRR is prescribed. In such cases, minor changes in the properties of bounding surfaces do not have a significant impact on the results. However, when the HRR is not prescribed, but rather predicted by the model using the thermophysical properties of the fuels, the model output is sensitive to even minor changes in these properties.[11]

00identifies normalized parameters that are used to compare NPP fire scenarios with validation experiments. The validation range for the normalized parameters shown in 0were derived from NUREG- 1824 (EPRI 1011999), are intended to provide guidance on which groups of validation experiments to consider when evaluating a certain attribute based on the validation results. These parameters may not be the only ones appropriate for evaluating the applicability of a specific experiment; 0also lists the ranges of values for different physical characteristics and normalized parameters based on the experiments considered in the validation study.

The user could calculate the normalized parameters that are relevant to the fire scenario being evaluated. If the parameters fall within the ranges evaluated as in 0, then the results of this study offer appropriate validation for the scenario. If they fall outside the range, then a validation determination cannot be made based on the results in this study. For any given fire scenario, more than one normalized parameter may be necessary for determining applicability of the validation results.[6]

A. Smokeview - A Tool for Visualizing Fire Dynamics Simulation Data

Output field data are visualized by post solver application named SmokeView, a software tool specifically designed to analyze data generated by FDS to show simulation results in order to visualize numerical calculations generated by fire models such as the FDS. SmokeView is able to perform visualization by animating particle flow, contour slices of computed gas variables and surface data plus vector plots of static data at the fixed time.

Josip Vuković, Davor Grgić, Performance Based Risk Informed Fire Modelling Evaluation of Electrical Equipment Functionality in Nuclear Power Plants, Journal of Energy, vol. 74 Number 4 (2025), 14–21
https://doi.org/10.37798/2025744734

SmokeView visualizes smoke and other attributes of the fire using traditional scientific methods such as displaying tracer particle flow, 2D or 3D shaded contours of gas flow data such as temperature and flow vectors showing flow direction and magnitude. Smokeview also visualizes fire attributes realistically so that one can experience the fire. This is done by displaying a series of partially transparent planes where the transparencies in each plane (at each grid node) are determined from soot densities computed by FDS.

FDS and Smokeview are primarily used to model and visualize time-varying fire phenomena. FDS and Smokeview are not limited to fire simulation, however. Smokeview also visualizes static data at particular times again using 2D or 3D contours of data such as temperature and flow vectors showing flow direction and magnitude.

Smokeview is used before, during and after model runs. Smokeview is used in a post-processing step to visualize FDS data after a calculation has been completed. Smokeview may also be used during a calculation to monitor a simulation's progress and before a calculation to setup FDS input files more quickly.[12]

V. Large Lubricating Oil Leakage Fire in a Fire Compartment

Various scenarios can be modeled. This scenario is propagating in relatively simple geometry. Lubricating oil is a mixture of various hydrocarbons, mostly alkanes with formula CnH2n+2. Fire compartment contains one door and one ventilation duct with one supply and one discharge, mechanical ventilation is to be modeled. Physics inside the compartment is practically the same as every fire inside a control volume.

Large lubricating oil fire (this source fire is the forcing function for the fire scenario) is postulated by oil leakage in Safety Related Pump Room and modeled to display the fire propagation and influence on thermal response of power cable and possible cable failure, that is to determine if the Room could keep the safety function. Fire compartment may also include secondary combustibles, overhead raceways, cable air-drops, stored materials, electrical panels, construction materials, etc. Such compartment modeled by FDS is shown on Fig 6.

Fire development in compartments is often divided into phases depending on the dominant processes at any given stage of development. Ignition is dictated by the characteristics of the fuel item being ignited (i.e., ignition temperature, geometry, orientation, and thermophysical properties) and the strength of the ignition source.

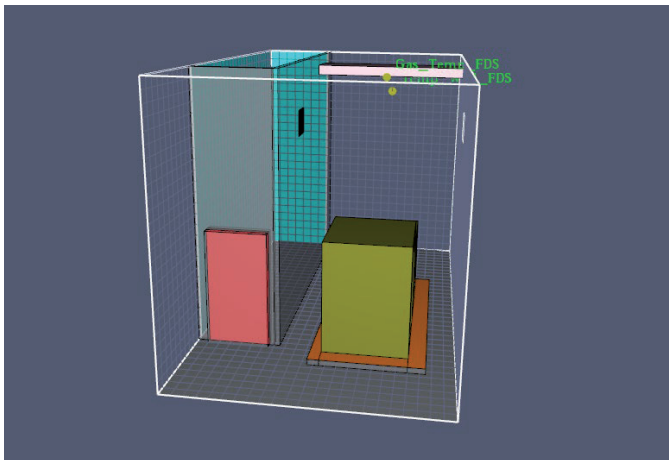

Figure 6: FDS modeled Safety Pump Room with pump-motor set

Once the flames are sustained on a burning fuel item, a smoke plume develops, transporting mass and heat vertically as a result of the buoyancy of the smoke. The plume will entrain air as it rises, thereby causing the smoke to cool and become diluted; as a result, the quantity of smoke being transported will increase with increasing elevation. After a smoke plume strikes the ceiling, the smoke travels horizontally under the ceiling in a relatively thin layer, referred to as a ceiling jet. As the ceiling jet travels, the smoke cools with increasing distance from the plume impingement point, in part because of air entrainment into the ceiling jet as well as heat losses from the ceiling jet to the solid ceiling boundary. In an ideal situation, once the ceiling jet reaches the enclosing walls, a HGL develops. As a result of the continuing supply of smoke mass and heat via the plume, the HGL becomes deeper, and its temperature increases. Other properties of the smoke in the HGL also increase (including concentration of gas species and solid particulates). Radiant heat from the HGL to other combustibles not involved in the fire increases their temperature. Similarly, the temperature of non-burning combustibles will also increase as a result of thermal radiation from the burning item(s). As the other combustibles reach their respective ignition temperatures, they will also ignite. In some cases, the ignition of many other combustibles in the space caused by heating from the HGL occurs within a very short time span. This is commonly referred to as flashover.[4]

Affected targets of interest in this scenario were also the walls and ceiling of the enclosure, which are fire barriers, as well as other safety-related equipment but primarily cables located in the room. These target cables shall be exposed to direct flame impingement or flame radiation or plume, ceiling jet, and hot gas layer conditions.

The walls, ceiling, and floor are all constructed of concrete. The single cable tray in this compartment is filled with PE/PVC cables with copper conductors. Damage criterion is taken to be the point at which the cable temperature reaches 205 °C as shown in 0. The protected cable tray is modeled as a rectangular box with the same dimensions as the tray. A cable target is positioned within the box pointing downwards, as this is the hottest surface of the box. What matters is that the cable within the box is exposed to the heat that penetrates the thermal blanket. The cable tray is protected by an electrical raceway fire barrier system (ERFBS), which is two layers of ceramic fiber insulation blankets, covered by 0.0254 mm foil. ERFBS has undergone a fire endurance furnace test in which the average temperature of the electrical raceway was maintained below 121 °C and the maximum temperature below 163 °C for an hour when exposed to the standard ASTM E 119 temperature curve. The ERFBS protected cable raceway is modeled with three layers: ceramic fiber blanket (5 cm), PE/PVC (4.4 mm), and copper (3.1 mm).[4]

There is one supply and one return air vent, each with an area of 0.25 m2, providing a volume flow rate of 0.25 m3/s. The pump compartment has one door; it is 1.1 m wide and 2.1 m tall. The door is normally closed, but it is opened 10 min after ignition by the fire brigade. The pump is surrounded by a dike designed to contain any lubricating oil that may leak or spill, with a maximum capacity of 190L. For the purpose of modeling, the fuel is specified to be C14H30.

VI: Results Summary

The fire occurs following an accidental release of pump oil and ignition of oil that leaked into the dike area. Fig 7 shows the conditions inside the modeled compartment at the start of the accident. Due to the limited amount of validation data available for scenarios of this type and the considerable uncertainties involved, the approach taken is to specify, rather than attempt to predict, the burning rate of the fuel, even though the FDS model does provide

Josip Vuković, Davor Grgić, Performance Based Risk Informed Fire Modelling Evaluation of Electrical Equipment Functionality in Nuclear Power Plants, Journal of Energy, vol. 74 Number 4 (2025), 14–21
https://doi.org/10.37798/2025744734

the physical mechanisms to estimate burning rates. The primary advantage of a CFD model for this fire scenario is that FDS modeling include combustion algorithms that estimate near- and post-flashover conditions.

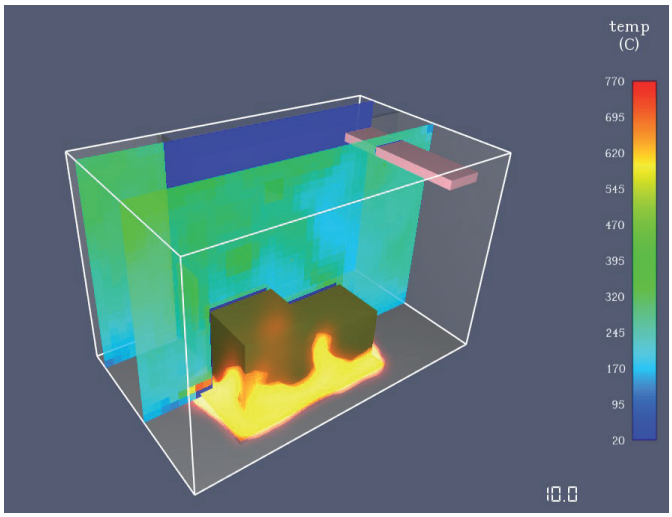

Fig. 7. Flame volume and temperature in control plane at t=10s

At the start of the scenario, the mechanical ventilation is operational, the door is closed, and the fire output immediately jumps to the peak heat release rate (HRR). Calculated peak HRR is 4,934kW (1). With specified burning rate, 0.039 kg/m^2m^2/s, is applied directly to the model over an area of 2.75 m^2m^2 yielding a burning rate of 0.107 kg/s. The density of the oil is 0.76 kg/L, which means that the oil burns at a rate of 0.141 L/s. At this rate, 190 L will require 1,348 s to burn out. The fire duration computation for FDS converts the mass data to volumetric data, thus introducing an additional step and some rounding.[4]

Predicted cable temperature from FDS, including an assessment of the model uncertainty is 145°C. The result is based only on a direct calculation of cable temperature. Critical value of cable temperature is not exceeded.

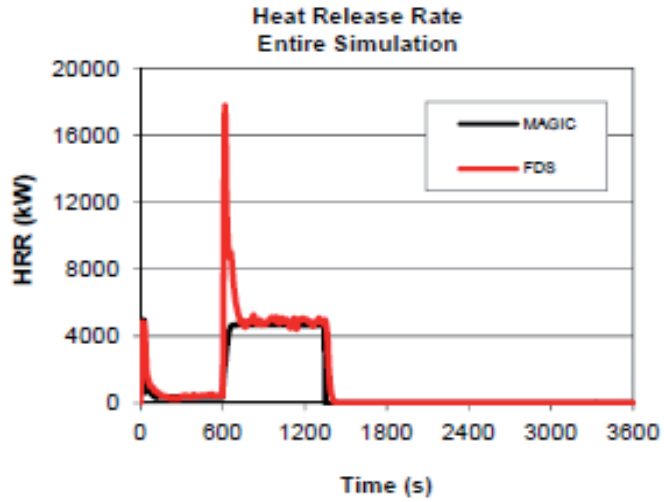

Fig. 8. HRR predicted by FDS – entire simulation

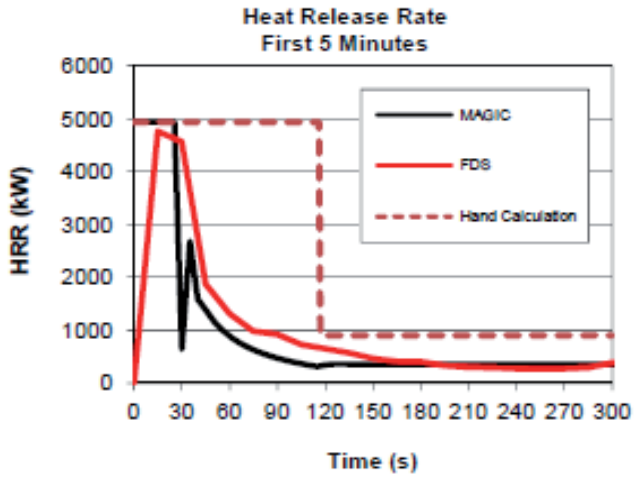

Fig. 9. HRR predicted by FDS – start of simulation

As can be seen from HRR curves (Fig 9&10) FDS models pronounced drop in the HRR soon after the start of fire, which shows that there is insufficient oxygen in the room to sustain the fire. At high temperatures, FDS expects all of the oxygen is consumed. The sudden jump in the HRR, predicted by FDS at 600 seconds, is caused by the unburned fuel igniting as the door is opened. The model indicates that the HRR decreases from about 4900 kW to about 350 kW in approximately 2 min. When the oxygen is insufficient to maintain the fire, FDS also continues to vaporize the unburned fuel, and it continues to transport the fuel gas until the door is opened after 10 min, at which time this excess fuel mixes with incoming air and burns. This rapid burning of built-up excess fuel gas in an under-ventilated compartment is known as a "backdraft," and it is apparent from the HRR curve in Fig 8. However, much of the heat from this rapid burning of fuel is immediately exhausted from the compartment and does not significantly affect the temperature of the ERFBS.

To predict cable damage due to temperature and incident heat flux, FDS estimates the temperature of the HGL as a function of time, as shown in Fig 10. As expected, the HGL temperature changes in accordance with the as above described (oxygen-starved) HRR. Once the door opens at 600 seconds, the increased HRR causes the HGL temperature to rapidly increase until the fire consumes the available fuel. After the fire burns out, the HGL temperature slowly drops as heat leaves the HGL through the bounding surfaces and open door. FDS has heat conduction algorithms to account for the multiple layers of insulation and cable materials, further on ERFBS has a large impact on the temperature of the target cable.[4]

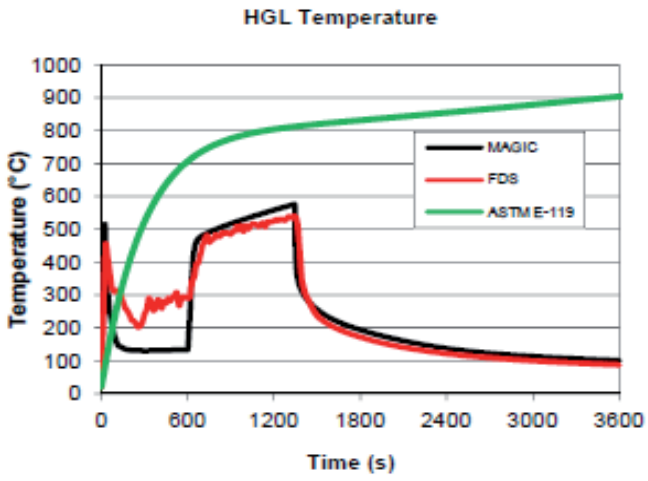

Fig. 10. HGL predicted by FDS for pump room fire

Josip Vuković, Davor Grgić, Performance Based Risk Informed Fire Modelling Evaluation of Electrical Equipment Functionality in Nuclear Power Plants, Journal of Energy, vol. 74 Number 4 (2025), 14–21
https://doi.org/10.37798/2025744734

The HGL temperature for this case reaches 640 °C, compared to 580 °C for the base case, which is still significantly lower than the ASTM E119 temperature curve. However, the predicted cable surface temperature is 200 °C, falling just below the failure criterion of 205 °C. This five-degree margin suggests that further validation may be needed to ensure that the thermal properties of the ERFBS are accurate.[4]

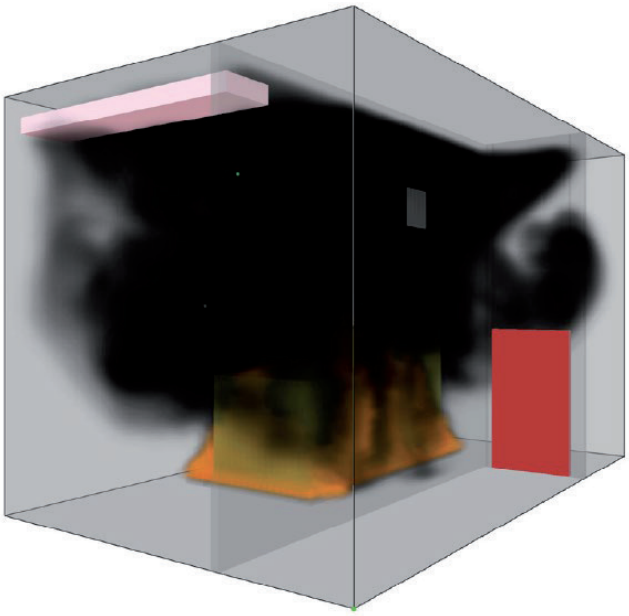

Fig. 11. Smoke buoyancy in the Safety Pump Room

In addition to HRR and temperature, as can be seen from the Fig 11, air is entrained into the flame and/or smoke plume. Consequently, the rate of smoke production at a particular height in the plume is the combination of the generation rate of combustion products and air entrainment rate into the flame and/or smoke plume between the top of the fuel and the height of interest.

Rate of smoke filling rate of is dependent on the rate of smoke production, the heat release rate (HRR), floor area, height and configuration of the space, and time from ignition. For a fire with a steady HRR, the rate of smoke filling in a compartment will decrease with time due to a decrease in the smoke production rate, which decreases as the height available to entrain air decreases when the HGL deepens.

Analysis suggests that to avoid rapid fire escalation, doors to such rooms should not be opened until firefighters are prepared to suppress the fire, and, even then, the potential for rapid fire escalation should be considered. ERFBS is expected to prevent the cables from reaching temperatures that would limit their functionality in the event of a fire involving burning spilled lubricating oil. This conclusion is based on certain expected burning behavior of the lubricating oil during the under-ventilated stages.

Further validation of the thermal properties of the ERFBS is needed in this case to reduce the impact of parameter uncertainty on the surface temperature calculation. Also, a detailed analysis of the cable surface temperature that would limit cable functionality and therefore set the pump-motor inoperable to perform safety function is essential to conform with performance-based risk informed utilization of fire protection. Probability of cable failure is of the most concern when assessing target damage and is to be further analyzed.

References

[1] Nuclear Regulatory Commission, BTP ASB 9.5-1, "Guidelines for Fire Protection for Nuclear Power Plants," Revision 1, March 1979.

[2] Regulatory Guide 1.189, "Fire Protection for Nuclear Power Plants," Revision 2, U.S. Nuclear Regulatory Commission, Washington, DC, October 2009. (ADAMS Accession No. ML092580550)

[3] Fire Protection Equipment Surveillance Optimization and Maintenance Guide, Nuclear Maintenance Applications Center (NMAC), EPRI, Charlotte, July 2003.

[4] NUREG-1934 (EPRI 1023259), Nuclear Power Plant Fire Modeling Analysis Guidelines (NPP FIRE MAG), November 2012.

[5] NUREG-1805, Fire Dynamics Tools (FDTs) Quantitative Fire Hazard Analysis Methods for the U.S. Nuclear Regulatory Commission Fire Protection Inspection Program, 2004.

[6] NUREG-1824 (EPRI 1011999), Verification and Validation of Selected Fire Models for Nuclear Power Plant Applications, 2007.

[7] NUREG/CR-6850 (EPRI 1011999), EPRI/NRC-RES Fire PRA Methodology for Nuclear Power Facilities, Electric Power Research Institute (EPRI), Palo Alto, 2005.

[8] K. McGrattan, S. Hostikka, J. Floyd, R McDermott and M. Vanella, "Fire Dynamics Simulator Technical Reference Guide Volume 1: Mathematical Model", National Institute of Standards and Technology Gaithersburg, Maryland, and Aalto University, Espoo, Finland, and Jensen Hughes, Rockville, Maryland, NIST Special Publication 1018-1 Sixth Edition, October 31, 2019

[9] K. McGrattan, S. Hostikka, J. Floyd, R McDermott and M. Vanella, "Fire Dynamics Simulator User's Guide", National Institute of Standards and Technology Gaithersburg, Maryland, and VTT Aalto University, Espoo, Finland, and Jensen Hughes, Rockville, Maryland, NIST Special Publication 1019 Sixth Edition, October 31, 2019

[10] K. McGrattan, S. Hostikka, J. Floyd, R McDermott and M. Vanella, "Fire Dynamics Simulator Technical Reference Guide Volume 2: Verification", National Institute of Standards and Technology Gaithersburg, Maryland, and Aalto University, Espoo, Finland, and Jensen Hughes, Rockville, Maryland, NIST Special Publication 1018-2 Sixth Edition, October 31, 2019

[11] K. McGrattan, S. Hostikka, J. Floyd, R McDermott and M. Vanella, "Fire Dynamics Simulator Technical Reference Guide Volume 3: Validation", National Institute of Standards and Technology Gaithersburg, Maryland, and Aalto University, Espoo, Finland, and Jensen Hughes, Rockville, Maryland, NIST Special Publication 1018-3 Sixth Edition, October 31, 2019

[12] G. P. Forney, "Smokeview, A Tool for Visualizing Fire Dynamics Simulation Data, Volume I: User's Guide", National Institute of Standards and Technology, Gaithersburg, Maryland, USA, NIST Special Publication 1017-1 Sixth Edition, October 30, 2019

[13] Regulatory Guide 1.205, "Risk-Informed, Performance-Based Fire Protection for Existing Light-Water Nuclear Power Plants," U.S. Nuclear Regulatory Commission, Washington, DC.

[14] NFPA 805, "Performance-Based Standard for Fire Protection for Light-Water Reactor ElectricGenerating Plants," 2001 Edition, National Fire Protection Association, Quincy, MA.

[15] Nuclear Regulatory Commission, "Appendix A to BTP APCSB 9.5-1 - Guidelines for Fire Protection for Nuclear Power Plants, Docketed Prior to July 1, 1976," February 24, 1977.

[16] Code of Federal Regulations, Title 10, Energy, Part 50, Appendix R, "Fire Protection Program for Nuclear Power Facilities Operating Prior to January 1, 1979," U.S. Government Printing Office, Washington DC.

[17] NEI 04-02, "Guidance for Implementing a Risk-Informed, Performance-Based Fire Protection Program Under 10 CFR 50.48(c)," Revision 2, Nuclear Energy Institute, Washington, DC, April 2008. (NRC's Agencywide Documents Access and Management System (ADAMS) Accession No. ML081130188)

Josip Vuković, Davor Grgić, Performance Based Risk Informed Fire Modelling Evaluation of Electrical Equipment Functionality in Nuclear Power Plants, Journal of Energy, vol. 74 Number 4 (2025), 14–21
https://doi.org/10.37798/2025744734

Journal of Energy
VOLUME 74 Number 4 | 2025
journal homepage: http://journalofenergy.com/

Point-Kernel Shielding Applications of Sievert Integral

Mario Matijević, Andrea Kaselj, Krešimir Trontl

Summary **—The application of a point-kernel technique in gamma radiation shielding calculations has a long and successful history. Using this approach radiation sources of various shapes such as point, linear, planar, or volumetric can be subdivided using the linear superposition principle to calculate total radiation received at a detector. Mathematically, any form of a distributed source may be treated as a summation i.e. integration of the radiation received from an equivalent number of point sources, for which exponential point-kernel function is analytically known. Fundamental assumption is that there is no interaction of individual, point sources which together represent total distributed radiation source. The effects of geometrical boundaries and gamma scattering are not included in this treatment, so user should be aware of these inherent limitations when comparing with reference results, such as Monte Carlo (MC) solution. This paper presents specific case of gamma flux attenuation from a distributed line source of photons in front of a slab shield, but is actually part of a larger effort, whose final goal is a general-purpose point-kernel code development. The solution of a line source with slab shield is known as the secant or Sievert integral, which cannot be evaluated analytically, so auxiliary tabulated function is introduced to facilitate bilinear interpolation on angle and shield thickness. Such code written in C-language will provide graphical user interface to assist user with necessary input data preparation and selection of predefined shielding materials for which Taylor buildup factors are provided. This paper gives programming and numerical aspects of such point-kernel code for which results of the test cases are compared with a MC solution of SCALE6.1.3 code package.**

Keywords **— point-kernel, line source, gamma radiation, shielding, buildup factors**

I. Introduction

The point-kernel method in radiation shielding originates from the early days of reactor projects which clearly demonstrated how shield design for neutrons and gamma rays possess significant problems regarding price, size and efficient flux attenuation. Starting with first organized research program in reactor shielding (end of 1940-ties in USA) it was soon recognized that the radiation streaming through ducts and holes together with secondary gamma heating effects in the shield will greatly influence the overall shielding design. The Oak Ridge National Laboratory (ORNL) conducted pioneering research investigation that led to the concept of the fast neutron removal cross section, which quickly came into widespread use for neutron attenuation problems. After that, the pool-type research reactors were constructed and provided numerous basic and applied results of shielding materials. The cancelation of the USA aircraft nuclear propulsion program and successful nuclear submarine program (1950-ies) gave a rich development of shield-analysis methods (point-kernel, method of moments, removal-diffusion, gamma-ray buildup factors, etc.) together with new experimental facilities being built worldwide. Simultaneously, early papers of H. Kahn [1] from Rand Corporation on the Monte Carlo (MC) application for radiation shielding showed a new, alternative approach but scarcity of the first digital computers deferred widespread use of this new stochastic technique, which was also investigated in ORNL and LASL (Los Alamos Scientific Laboratory). The numerical techniques for solving Boltzmann transport equation were concurrently investigated and the most notable one was B. Carlson's method of LASL known as discrete ordinates SN originating from mid 1950-ies [2]. After that, improvements in SN method on spatial differencing and various convergence techniques followed, giving a well known ANISN code of ORNL in 1965 which was also suitable for shielding calculations. In mid 1960-ies there were already eight major MC programs in use only in USA, which confirmed many analytical solutions for shielding configurations originating from an older point-kernel approach, which was still a standard shielding method of those days.

The important historical event from that period was also foundation of Radiation Shielding Information Computational Center (RSICC) in ORNL 1962, which still serves its original mission to promote development of new nuclear codes and data for shielding community. A more detailed historical exposition can be found in [3], but it suffice to say how even today point-kernel methods have their place in many preliminary shielding studies, before reaching to accurate MC or SN methods, giving a fast solution of the problem but within a well known theoretical constraints.

The rest of the paper is organized as follows. Chapter 2 gives formal point-kernel definition for gamma ray shielding with presentation of exponential point kernel and buildup factors. Chapter 3 presents the problem of radiation attenuation from a line source which leads to a Sievert integral solution. The programming details of the point-kernel program for line gamma source and slab shield are presented in Chapter 4, together with graphical user interface (GUI) development to assist user with input data. The comparison of gamma ray shielding results from the point-kernel and Monaco MC code of SCALE6.1.3 is presented in Chapter 5, while conclusions are given in Chapter 6. A list of references is given at the end of the paper.

(Corresponding author: Mario Matijević)
Mario Matijević, Andrea Kaselj and Krešimir Trontl are with the University of Zagreb Faculty of Electrical Engineering and Computing, Zagreb, Croatia (emails: mario.matijevic@fer.hr, andrea.kaselj@fer.hr, kresimir.trontl@fer.hr)

Mario Matijević, Andrea Kaselj, Krešimir Trontl, Point-Kernel Shielding Applications of Sievert Integral, Journal of Energy, vol. 74 Number 4 (2025), 22–29
https://doi.org/10.37798/2025744729

II. The Point-Kernel Method

The point-kernel method or mathematically speaking method of Green's function, is one of the oldest and widely used methods for the solution of both neutron and gamma-ray shielding problems [3][4][5]. Using this approach radiation sources of various shapes such as point, linear, planar, or volumetric can be subdivided using the linear superposition principle to calculate total radiation received at a detector. Mathematically, any form of a distributed source may be treated as a summation i.e. integration of the radiation received from an equivalent number of point sources, for which exponential point-kernel function is analytically known. Fundamental assumption is that there is no interaction of individual, point sources which together represent total distributed radiation source. The effects of geometrical boundaries and gamma scattering are not included in this treatment, so user should be aware of these inherent limitations when comparing with reference results, such as Monte Carlo (MC) solution.

The point-kernel principle is the following [6]: the radiation received at the detector (or other receptor) from a distributed source may be treated as s summation (or integration) of the radiations received from an equivalent number of point sources. The point-kernel function $G(|\vec{r}\,'-\vec{r}\,|)$ is defined as the response of a detector at the space point *r* coming from a point source of radiation located at *r'* emitting one particle per second. The source strength $S(\vec{r}\,')$ can be for a line, surface or volume configuration and if we consider small source element $d\vec{r}\,'$ (increment of length, area or volume) then we can construct a point source emitting particles at the rate of $S(\vec{r}\,')d\vec{r}\,'$. The differential response of a point detector located at $\vec{r}$ is simply:

$$d\phi(\vec{r}) = G(|\vec{r}\,'-\vec{r}\,|)S(\vec{r}\,')d\vec{r}\,'. \tag{1}$$

The total response of an isotropic point detector is obtained by integrating Eq. (1) over the whole finite source space as the

$$\phi(\vec{r}) = \int_{source} G(|\vec{r}\,'-\vec{r}\,|)S(\vec{r}\,')d\vec{r}\,'. \tag{2}$$

One should notice how the point-kernel function depends on a source-detector distance, on particle type, its energy, and materials covering intervening path of radiation. If a *G*-function can be obtained in a fairly simple form, such as exponential form, one could perform integration for distributed sources leading to useful results in radiation attenuation. This is typically done by considering a point isotropic emitter of S_p monoenergetic particles per second, for which uncollided particle flux is given as inverse square law over a hypothetical surface sphere of radius *R*:

$$\phi(R) = \frac{S_p}{4\pi R^2}\exp(-\mu R). \tag{3}$$

The exponential attenuation of a shielding material between the source and the detector is described with a linear attenuation coefficient μ (cm^{-1}), *R* is the line distance while μR is the number of gamma ray mean free paths. Taking the definition of point-kernel from Eq. (3) one can notice that the exponential kernel for the uncollided flux from a point source is given by

$$G(R) = \frac{\exp(-\mu R)}{4\pi R^2}. \tag{4}$$

This result is correct for a relatively thin layer of attenuating material, especially for photons of high energy, meaning there is a small probability of scattered photons reaching the detector. For practical purposes, gamma shields are always "thick", so after a multiple scattering there is certain probability of photon reaching the detector, giving a higher measured flux that exceeds the uncollided flux. Allowance of scattered flux reaching the detector is done by multiplicative buildup factor $B > 1$, which is a function of the number of mean free paths and photon energy. The total measured (buildup) flux will then consist of collided and uncollided part, so for point source of monoenergetic gamma rays S_p and distance *R* in shielding medium flux is given as

$$\phi(R) = \frac{S_p}{4\pi R^2}\exp(-\mu R)B(\mu R, E_\gamma), \tag{5}$$

while the corresponding point-kernel is

$$G(R) = \frac{\exp(-\mu R)B(\mu R, E_\gamma)}{4\pi R^2}. \tag{6}$$

The concept of buildup factors can be, at least in general, applied to both gamma rays and neutrons [7][8], but for practical purposes it is mainly used for gamma-ray attenuation calculation due to complex neutron interactions. Advancing the machine learning algorithms, there is also an incentive to integrate such artificial intelligence algorithms inside point-kernel paradigm [9]. In the case of fast neutrons, it leads to a concept of fast neutron removal cross sections. Tables of buildup factors are readily available as a function of gamma ray energy and shield thickness (in mean free paths) and should be differentiated for point source and planar source. When performing integration of distributed sources, it is often necessary to express buildup factors in analytical form, so in this paper we are using a well-known Taylor form given as:

$$B(\mu R, E_\gamma) = A\exp(-\alpha_1\cdot\mu R) + (1-A)\exp(-\alpha_2\cdot\mu R), \tag{7}$$

where A, α_1, and α_2 denote coefficients readily found in tabulated form for different shielding material and incident gamma ray energy. This function will later be combined with the point exponential kernel when deriving expressions for gamma flux from line source and slab shield. Parameters of the Taylor form can be found in the classical radiation shielding references [3][5].

III. Radiation Attenuation from a Line Source

This section presents application of point-kernel method to a gamma line source [6] emitting S_l particles/cm/s. If we take a differential element of line length *dl* (cm) then the product $S_l \cdot dl$ represents point gamma source (particles/s). The detector response at distance *R* is then given by point-kernel definition as integration over the length *l* of the source:

$$\phi(R) = \int_l S_l G(R)dl. \tag{8}$$

This result is completely general so actual problem setup is needed to perform specific integration. One should bear in mind how effects of problem boundaries are not included, similarly as gamma rays which may be multiple scattered in shield toward the detector are ignored. We are considering a long line representing linear isotropic radiator of photons in front of slab shield with thickness *t* (see Figure 1).

Mario Matijević, Andrea Kaselj, Krešimir Trontl, Point-Kernel Shielding Applications of Sievert Integral, Journal of Energy, vol. 74 Number 4 (2025), 22–29
https://doi.org/10.37798/2025744729

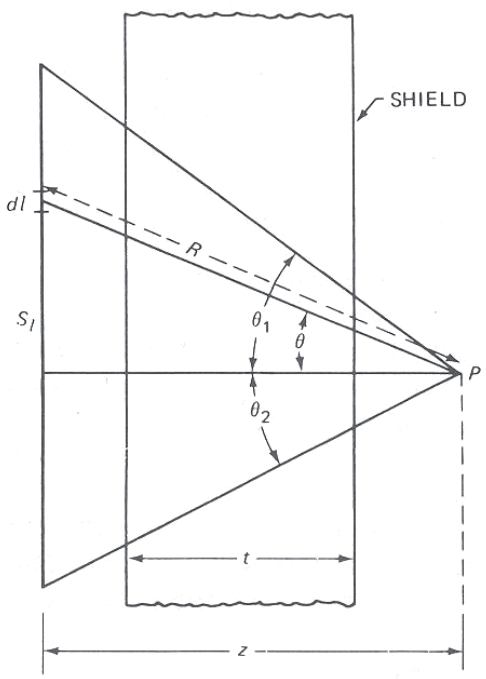

Fig. 1. Point detector response from gamma line source [6]

The exponential point kernel of Eq. (4) is substituted in Eq. (8) for general line source. The distance R for any point source to the detector is expressed in perpendicular distance from the line source to the detector P (variable z) and angle θ, i.e. $R = z \cdot \sec\theta$. The point-kernel function for the uncollided flux (B factor equal to 1) is written as a function of variables z, t, and θ, giving

$$G(z,t,\theta) = \frac{\exp(-\mu t \cdot \sec\theta)}{4\pi R^2} = \frac{\exp(-\mu t \cdot \sec\theta)}{4\pi (z \cdot \sec\theta)^2} . \quad (9)$$

To perform point-kernel integration, we express differential line element dl as a function of variables z and θ. This is done first by derivation of expression $R^2 = z^2 + l^2$, giving $l \cdot dl = R \cdot dR$. The same is repeated for differential element dR, i.e. the derivation of $z = R\cos\theta$ is giving $dR = (l \cdot d\theta)/\cos\theta$. Combining obtained expressions, we eliminate l variable and finally get

$$dl = z \cdot (\sec\theta)^2 \, d\theta . \quad (10)$$

This permits two-part integration over the whole line length in terms of angle θ, i.e. from 0 to θ1 and from 0 to θ_2:

$$\phi(R) = \int_l S_l G(R) dl = \int_l S_l \frac{\exp(-\mu t \cdot \sec\theta)}{4\pi (z \cdot \sec\theta)^2} z \cdot (\sec\theta)^2 \, d\theta . \quad (11)$$

$$\phi(R) = \frac{S_l}{4\pi z} \int_l \exp(-\mu t \cdot \sec\theta) d\theta = \frac{S_l}{4\pi z} \left[\int_0^{\theta_1} e^{-\mu t \cdot \sec\theta} d\theta + \int_0^{\theta_2} e^{-\mu t \cdot \sec\theta} d\theta \right] . \quad (12)$$

It is customary to introduce the secant or Sievert integral defined as $F(\theta,x) = \int_0^{\theta} e^{-x \cdot \sec\theta} d\theta$, so uncollided flux solution can be finally expressed as:

$$\phi_l(z,t) = \frac{S_l}{4\pi z} \left[F(\theta_1, \mu t) + F(\theta_2, \mu t) \right] . \quad (13)$$

Plots of Sievert integral are usually find in standard radiation shielding handbooks [3][4] for various values of (θ, x) or in tabulated values of auxiliary function $\overline{F}(\theta,x)$ as $F(\theta,x) = \theta e^{-x} \overline{F}(\theta,x)$ or in form of several series expansion with different and limited values of (θ, x). For purposes of programming, the tabulated F-function approach was selected.

To obtain the total flux solution, one must include the buildup factor $B(\mu t \cdot \sec\theta)$ in exponential point-kernel and again perform integration. For that purpose, we are using Taylor form of buildup factors as:

$$B = A \exp(-\alpha_1 \mu t \cdot \sec\theta) + (1 - A) \exp(-\alpha_2 \mu t \cdot \sec\theta) . \quad (14)$$

The corresponding point-kernel for buildup flux is thus

$$G(z,t,\theta) = \frac{1}{4\pi (z \cdot \sec\theta)^2} \left[A e^{-\mu t \cdot \sec\theta (1+\alpha_1)} + (1-A) e^{-\mu t \cdot \sec\theta (1+\alpha_2)} \right] , \quad (15)$$

while the total or buildup flux from gamma line source becomes

$$\phi_l(z,t) = \frac{S_l}{4\pi z} \left[\begin{array}{l} A\{F(\theta_1, \mu t(1+\alpha_1)) + F(\theta_2, \mu t(1+\alpha_1))\} + \\ (1-A)\{F(\theta_1, \mu t(1+\alpha_2)) + F(\theta_2, \mu t(1+\alpha_2))\} \end{array} \right] . \quad (16)$$

For practical purposes, this buildup flux of photons originating from the gamma line source and penetrating slab shield configuration can be expressed as a relative ratio to the uncollided flux component, giving so called numerical approximation of the buildup factor, which can be easily compared to other (theoretical) buildup factors set, such as Taylor or Goldstein [3][5]:

$$B = \frac{\phi_{tot}}{\phi_{unc}} = \frac{\begin{array}{l} A\{F(\theta_1, \mu t(1+\alpha_1)) + F(\theta_2, \mu t(1+\alpha_1))\} + \\ (1-A)\{F(\theta_1, \mu t(1+\alpha_2)) + F(\theta_2, \mu t(1+\alpha_2))\} \end{array}}{F(\theta_1, \mu t) + F(\theta_2, \mu t)} . \quad (17)$$

The presented equations for the gamma line source and slab shield are used for programming the point-kernel code which can be used in two different ways: a) shield thickness is a known input parameter, buildup flux is searched on point detector; b) buildup flux on point detector is a known input parameter, shield thickness is searched. In the later case, which is a more difficult one, iterative algorithm with predefined precision is used for a numerical solution.

IV. The Point-Kernel Code Development

The C-programming language [10] was used as a standard tool for coding numerical routines which solve gamma line equations presented in the previous Chapter. The exposure buildup factors for point gamma source (i.e. Goldstein data set) as well as coefficients of Taylor form were used from classic references [3] [5], together with mass attenuation data and densities of several shield materials [6]: water, concrete, aluminum, iron, tin, lead and depleted uranium. The linear interpolation C function was written for calculation of mass attenuation coefficients and for Taylor co-

Mario Matijević, Andrea Kaselj, Krešimir Trontl, Point-Kernel Shielding Applications of Sievert Integral, Journal of Energy, vol. 74 Number 4 (2025), 22–29
https://doi.org/10.37798/2025744729

efficients, since the user provides floating point value for gamma ray energy in MeV. The bilinear interpolation routine was written for calculation of F-function values and Goldstein buildup factors. These user-defined C functions are floating point type with several arguments of floating-point values and pointers on data sets. For example, the function prototype of bilinear interpolation on Goldstein set is given as the float type function with float pointers on buildup factors matrix, energy vector, shield thickness vector, user-defined energy, and user-defined shield thickness:

```
float BilinInt(float *tablica, float *ene, float
*deb, float Eg, float mfp);
```

The user is prompted to select and enter several input variables describing the basic shielding problem: shielding material (1 to 7), gamma ray energy in range [0.5 - 10] MeV, gamma line specific intensity (phot/cm/s), perpendicular distance from gamma line to a point detector, upper and lower line lengths (in cm). The selection of shielding materials (on left) and gamma line parameters (on right) is shown in Figure 2.

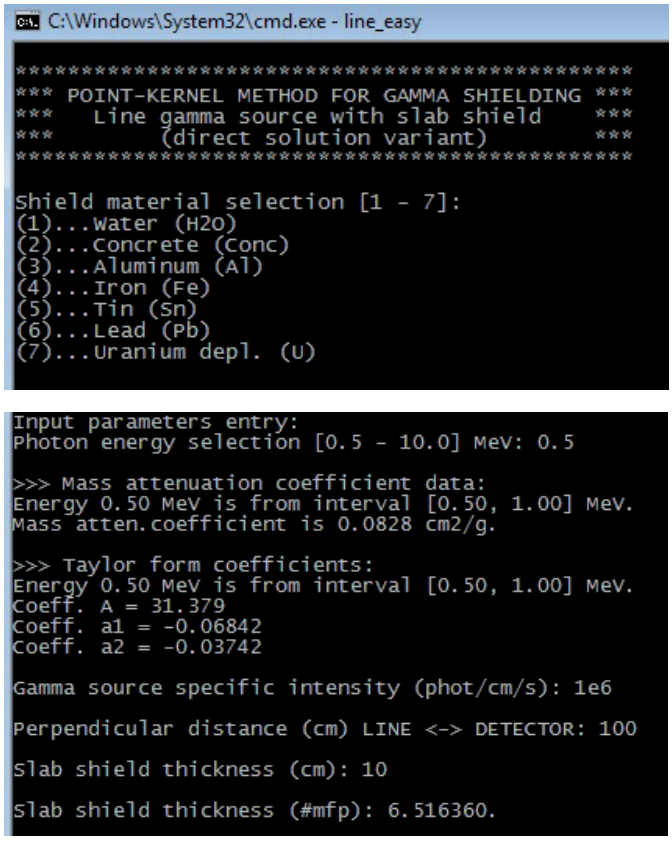

Fig. 2. Example of user entry values

The user input data are accompanied with partial on-screen printout of intermediate results, such as mass attenuation coefficient, gamma ray mean free path (mfp) in shield, Taylor form coefficients, F-function or Sievert integral values, Goldstein buildup factors, etc. The example of such intermediate results is shown in Figure 3 for an asymmetric gamma line with a total length of 125 cm and bilinear interpolation of 10.78 for Goldstein buildup factor.

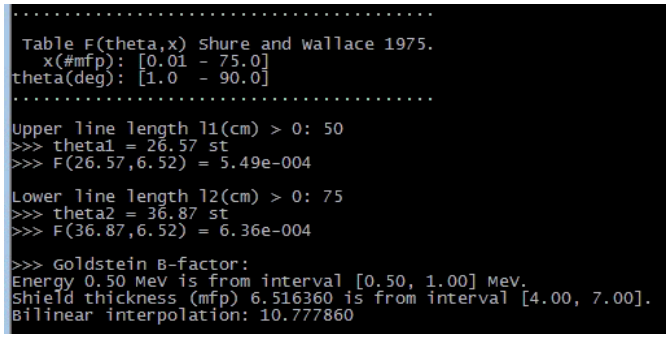

Figure 3: Example of intermediate results

The compiled point-kernel program can be run in two basic modes:

a) *Direct solution variant* (or "easy solution") - the user enters slab shield thickness (in cm) while the program calculates three types of buildup factors (Goldstein, Taylor and numerical) and buildup gamma flux on point detector, based on user input data.

b) *Iterative solution variant* (or "hard solution") - the user enters buildup flux on a point detector (phot/cm^2/s) while the program calculates three types of buildup factors (Goldstein, Taylor and numeric) and slab shield thickness, based on user input data.

In both cases the program will print out information on the relative flux ratio, i.e. uncollided flux divided over buildup flux, providing information about the importance of photon scattering inside the shield. The program finally prints information about CPU timing in ms and sec, based on different built-in C functions defined in "sys/timeb.h" and "time.h" libraries. The Figure 4 shows results of the direct solution variant using the following input parameters: iron shield 10 cm thick, gamma ray energy 0.5 MeV, specific gamma source of 1e6 phot/cm/s, total line length of 125 cm (50 cm above z=0 cm plane and 75 cm below), and line-to-detector distance of 100 cm. One can notice how the flux ratio of uncollided to total is about 9.33% so by inverting this value one can simply obtain so-called numerical buildup factor, which is similar to a well-known theoretical value of Goldstein and Taylor.

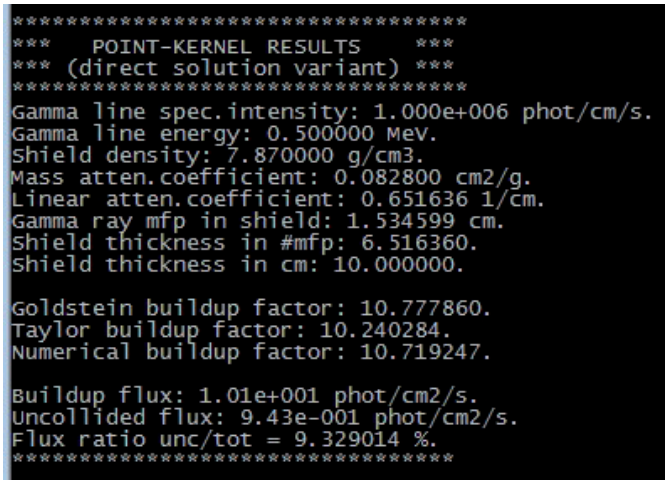

Figure 4: Main output values - direct solution

Mario Matijević, Andrea Kaselj, Krešimir Trontl, Point-Kernel Shielding Applications of Sievert Integral, Journal of Energy, vol. 74 Number 4 (2025), 22–29
https://doi.org/10.37798/2025744729

If the same setup problem is re-run in iterative solution variant, where user inputs a known buildup flux of 10.1 phot/cm²/s, then the shield thickness of 10.002086 cm is obtained through 5518 iterations with total CPU time of 15 ms for the initial shield thickness of 1 mfp (allowed range is 0.01 - 75 mfp). In the worst-case scenario, if the user enters trail value for the shield thickness of 75 mfp, the number of iterations increases to 68512 with total CPU of 110 ms, which is a factor of 7 increase. The iterative solution results for the same problem are shown in Figure 5. The user can easily change numerical ε-values which control desired solution precision and have direct influence on iteration number and CPU timing.

```
**************************************
***      POINT-KERNEL RESULTS      ***
*** (iterative solution variant) ***
**************************************
Gamma line spec.intensity: 1.000e+006 phot/cm/s.
Gamma line energy: 0.500000 MeV.
Shield density: 7.870000 g/cm3.
Mass atten.coefficient: 0.082800 cm2/g.
Liner atten.coefficient: 0.651636 1/cm.
Gamma ray mfp in shield: 1.534599 cm.
Shield thickness in #mfp: 6.517301.
Shield thickness in cm: 10.001444.

Goldstein buildup factor: 10.779654.
Taylor buildup factor: 10.242074.
Numerical buildup factor: 10.721163.

Iterations counter: 68512.
Buildup flux: 1.01e+001 phot/cm2/s.
Uncollided flux: 9.42e-001 phot/cm2/s.
Flux ratio unc/tot = 9.327346 %.

**************************************
***** CPU wall time in sec / ms *****
**************************************
---<function clock() from time.h>----
Wall time for 68512 iterations: 1.09e-001 sec.
Wall time per iteration: 1.59e-006 s.
---<function ftime() from timeb.h>---
Wall time for 68512 iterations: 1.10e+002 ms.
Wall time per iteration: 1.61e-003 ms.
**************************************
```

Fig. 5. Main output values - iterative solution

The final effort was put into a graphical user interface (GUI) development, written in C++ language [11] as a desktop application using Qt cross-platform [12] development framework as widget toolkit. The GUI is an interface program between precompiled executable modules and text-based input and output files. The main window in Figure 6 is a tab Widget which holds all open tabs. For both calculation variants there are input data fields, option to save the result to a text file, scheme of geometric configuration, result field, status and output fields and options to generate graphs by running the C application in a loop. The program displays and exports graphs for selected ranges of input data and provides a display of previously saved calculations in a separate tab. All input data are checked when pressing »Calculate« button and any error messages are shown in the status field. This software was implemented with the aim to enable further development by adding new components such as other source geometric configurations and visualization elements.

V. Comparison of Point-Kernel and MC Solution

The point-kernel solution of isotropic gamma line with a slab shield was compared with a reference MC solution of the same model using the MAVRIC shielding sequence of the SCALE6.1.3 code package [13]. The proposed benchmark was defined as in the previous chapter: isotropic gamma line emitting photons of energy 0.5 MeV, with specific source intensity of 1e6 phot/cm/s, total line length of 125 cm (50 cm above z=0 cm plane and 75 cm below), and line-to-detector distance of 100 cm. The center of the slab shield was always positioned symmetrically between the line and the point detector. The series of calculations were done for the varying slab shield thickness in cm (1, 5, 10, 20, 30, 40, and 50) and for two gamma line energies in MeV (0.5 and 10), enveloping all other values of available buildup factors. The Monaco MC module was used with the following parameters: "v7-27n19g" cross section library, total gamma source of 1.25e8 phot/sec, point detector tally estimator 100 cm from the gamma line, 300 batches with 10000 photons per batch. The CADIS variance reduction (VR) metho-

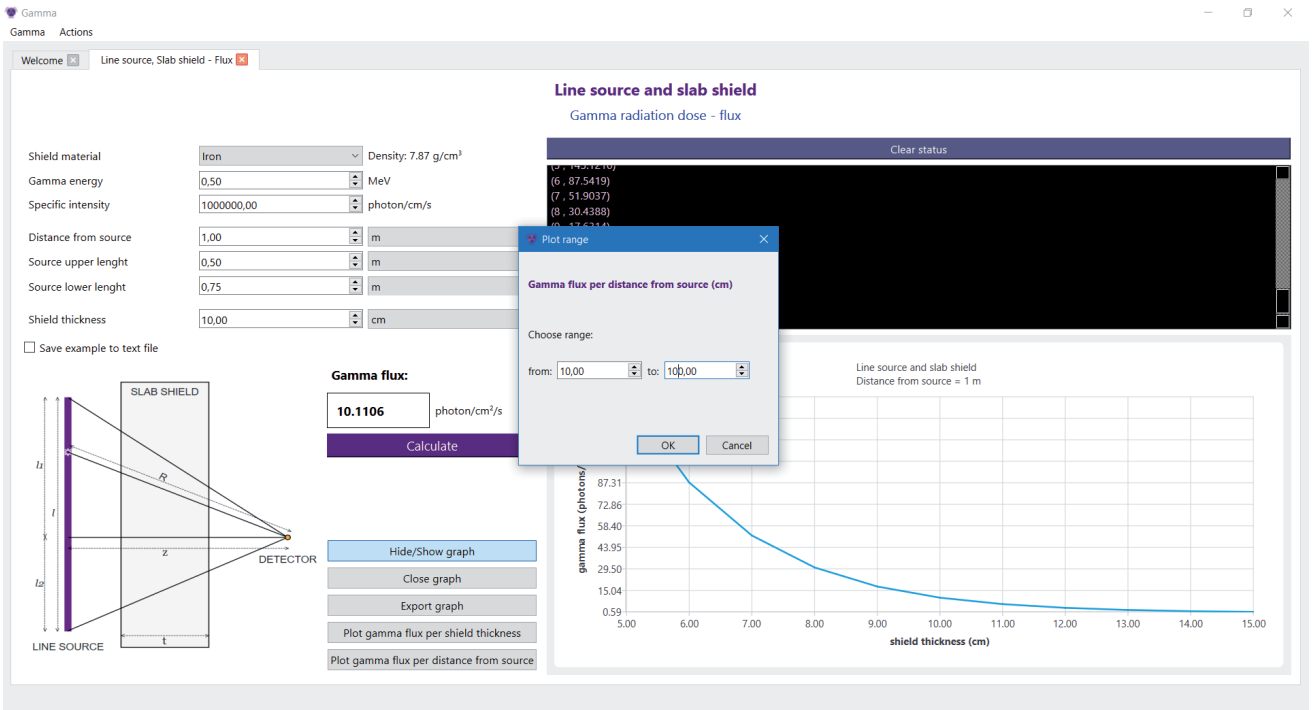

Fig. 6. The main window of the GUI program

Mario Matijević, Andrea Kaselj, Krešimir Trontl, Point-Kernel Shielding Applications of Sievert Integral, Journal of Energy, vol. 74 Number 4 (2025), 22–29
https://doi.org/10.37798/2025744729

dology was used only for those cases of a relatively thick shield with 0.5 MeV photons, while for other cases MC was run in an analog mode. The average MC relative error on point detector for all simulation cases was well below 0.1 % and CPU time took 6-9 minutes per MC simulation. The selected results of 0.5 MeV gamma rays are presented next. Figure 7 shows gamma buildup flux calculated by point-kernel and MC method with varying shield thickness, with noticeable flux difference starting above 30 cm thickness, which is a satisfactory overall behavior.

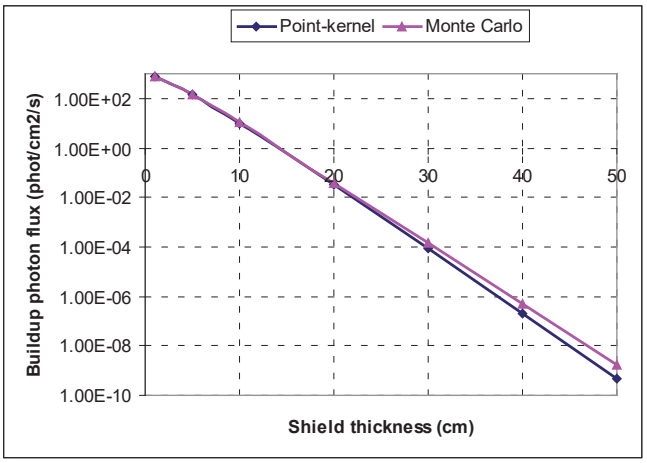

Fig. 7. Gamma buildup flux with point-kernel and MC (0.5 MeV photons)

The ratio of uncollided to buildup gamma flux is show in Figure 8 separately for point-kernel and MC solution, both exhibiting a similar profile, i.e. for shields thicker than 10 cm one can notice how uncollided flux component is below 10% in total flux, so photon scattering becomes a dominant process inside the shield. One can thus expect high-value buildup factors in this scenario.

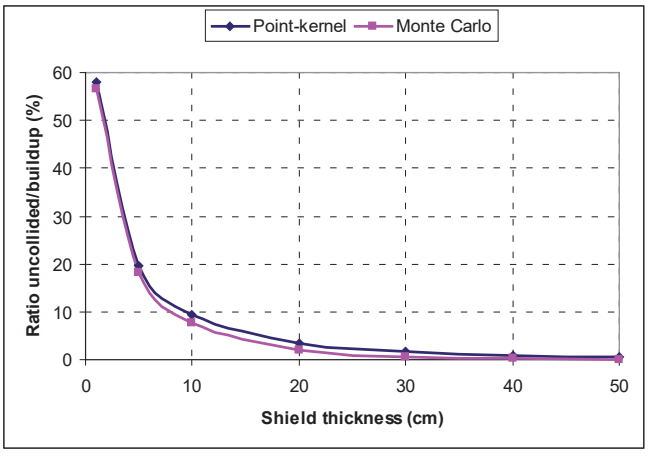

Fig. 8. Ratio of uncollided to total gamma flux (0.5 MeV photons)

Figure 9 shows relative error of point-kernel flux to an average MC flux; comparison is done separately for uncollided and buildup gamma flux. One can notice different trends of this curves with increasing shield thickness, i.e. more conservatism comes from the uncollided point-kernel flux and from the total MC flux. These noticeable differences have an origin in the MC particle transport, capturing many physical interactions of 0.5 MeV photons which are neglected in a simple point-kernel integration technique. For practical shielding purposes, one should be concerned only with iron shields up to cca. 20 cm (for example RPV), where point-kernel method exhibits relative error up to 20% , which is an acceptable deviation from the MC solution.

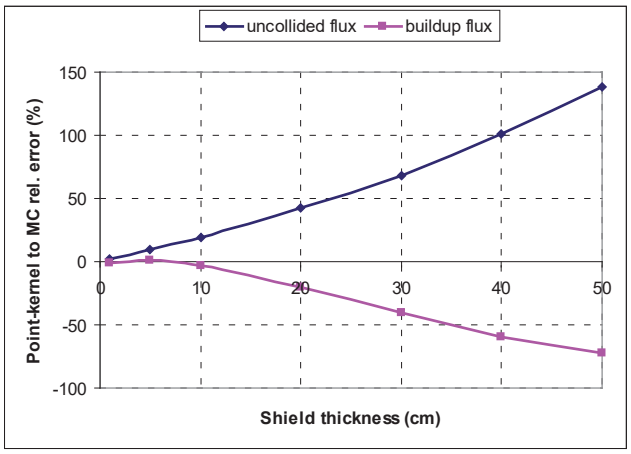

Fig. 9. Relative error of point-kernel to MC solution (0.5 MeV photons)

Finally, the buildup factors of 0.5 MeV photons are shown in Figure 10 as a shield thickness function and exhibit a well-known exponential increase. A good agreement between numerical and theory-based buildup factors has been obtained, with no systematic deviations in curve trends.

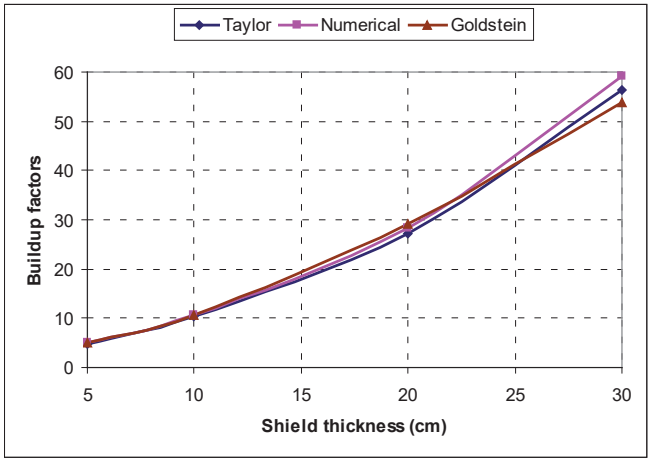

Fig. 10. The buildup factors for 0.5 MeV photons inside iron shield

For completeness, the mesh tally of MC gamma buildup flux with relative errors is shown in Figure 11 in y=0 plane, corresponding to case of 50 cm iron shield and 0.5 MeV photons. This is an example of deep-penetration gamma ray shielding problem, where effective VR techniques must be used, due to MC statistical constraints on point detector tally estimator. For this case, additional CPU time of 12.5 minutes is needed for the CADIS deterministic solution and VR preparation, so total CPU time amounts to 21 minutes. The MC buildup flux on point-detector is 1.77e-09 phot/cm^2/s with rel. error of 0.93%. For comparison, the point-kernel solution gives a smaller flux value of 0.48e-09 phot/cm^2/s with CPU time of cca 20 ms, since only a one-pass through program is needed to obtain an analytical solution. This is about 63000 times faster than MC solution, with an acceptable flux disagreement.

The selected results of 10 MeV gamma ray penetration exhibit different physical behavior since pair-production and photonuclear reactions become a more probable processes for high-energy photons inside the iron shield. Figure 12 shows buildup gamma flux calculated by point-kernel and MC method with varying shield thickness. The curve trends are similar with a constant offset (factor of few) of point-kernel flux values below MC values.

Mario Matijević, Andrea Kaselj, Krešimir Trontl, Point-Kernel Shielding Applications of Sievert Integral, Journal of Energy, vol. 74 Number 4 (2025), 22–29
https://doi.org/10.37798/2025744729

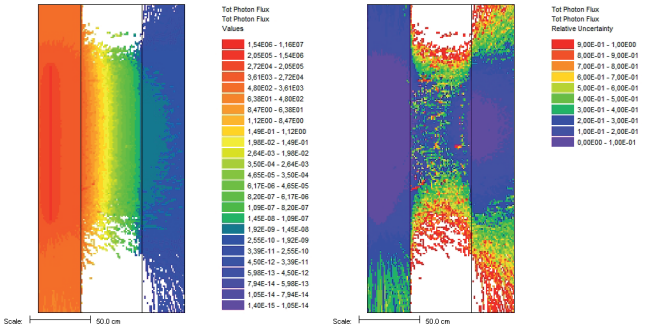

Fig.11. CADIS solution for 0.5 MeV photons and 50 cm thick iron shield

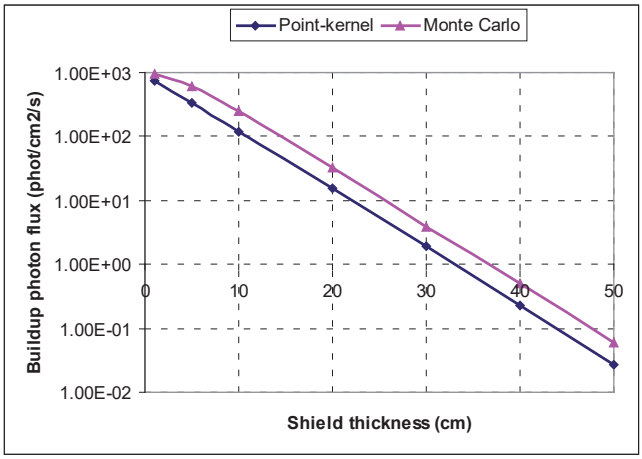

Fig. 12. Gamma buildup flux with point-kernel and MC (10 MeV photons)

The ratio of uncollided to total flux is shown in Figure 13, separately for a more conservative point-kernel and MC solution. Since energetic 10 MeV photons will penetrate iron shield more easily than 0.5 MeV photons, one can notice how gamma ray scattering becomes less pronounced. For example, in the case of 10 cm iron shield, this ratio is now over 60% for point-kernel solution and 30% for MC solution. In the case of 40 cm thick iron shield, this ratio drops to 25% for point-kernel and 10% for MC solution.

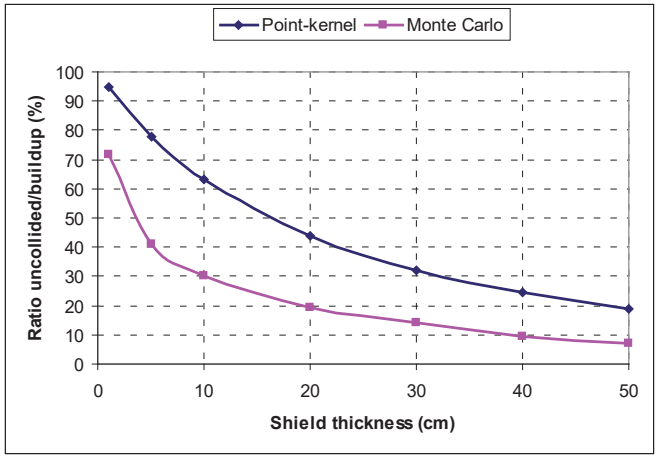

Fig. 13. Ratio of uncollided to total gamma flux (10 MeV photons)

The flux relative error of point-kernel to MC solution in Figure 14 is also different for high energy photons. The uncollided flux ratio between point-kernel and MC is positive and below 20% even for 50 cm thick iron shield while the buildup flux ratio drops to a practically constant value of -50% for shield thicknesses above 10 cm. This is a clear indication how an uncollided flux is a more conservative from a point-kernel solution, while the higher MC buildup flux takes into an account a complete photon physical interaction.

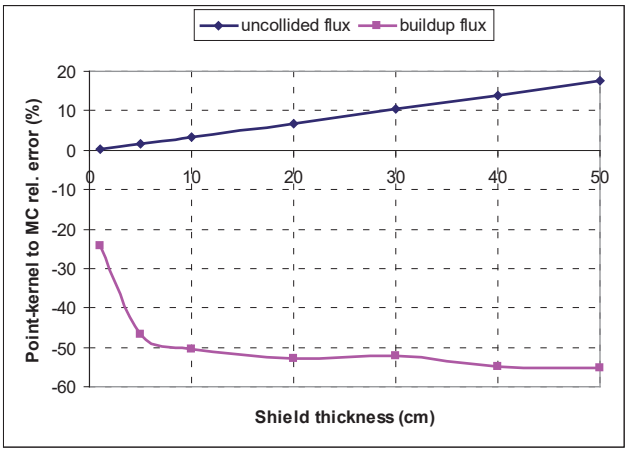

Fig. 14. Relative error of point-kernel to MC solution (10 MeV photons)

The buildup factors in Figure 15 show again a high level of similarity but with much smaller values (range 1 to 6), since the high-energy photon scattering inside the shield is now less pronounced.

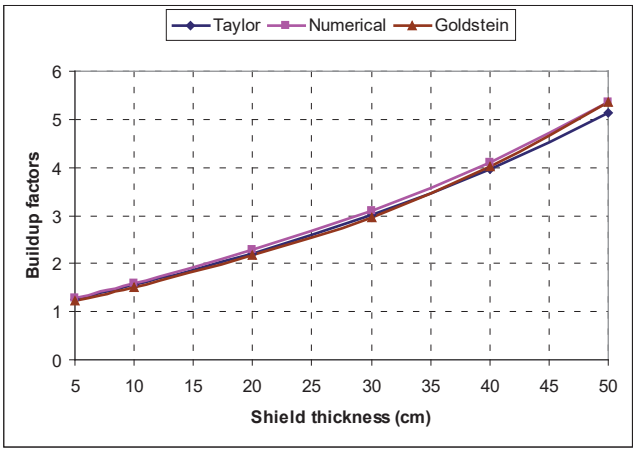

Fig. 15. The buildup factors for 10 MeV photons inside iron shield

Finally, the mesh tally solution of gamma buildup flux with relative errors is shown in Figure 16 in y=0 plane, for the case of 50 cm iron shield and 10 MeV photons. The CADIS method was again used with 12.9 min of CPU time for VR preparation, Monaco MC took 8.4 min so total CPU time amounts to 21.3 min. The point-detector MC buildup flux was 6.04e-02 phot/cm^2/s with rel. error 0.64%. For comparison, point-kernel solution gives smaller value of 2.70e-02 phot/cm^2/s with CPU time of 23 ms (speedup of cca 56000), since only a one-pass through program is needed to obtain an analytical solution.

Mario Matijević, Andrea Kaselj, Krešimir Trontl, Point-Kernel Shielding Applications of Sievert Integral, Journal of Energy, vol. 74 Number 4 (2025), 22–29
https://doi.org/10.37798/2025744729

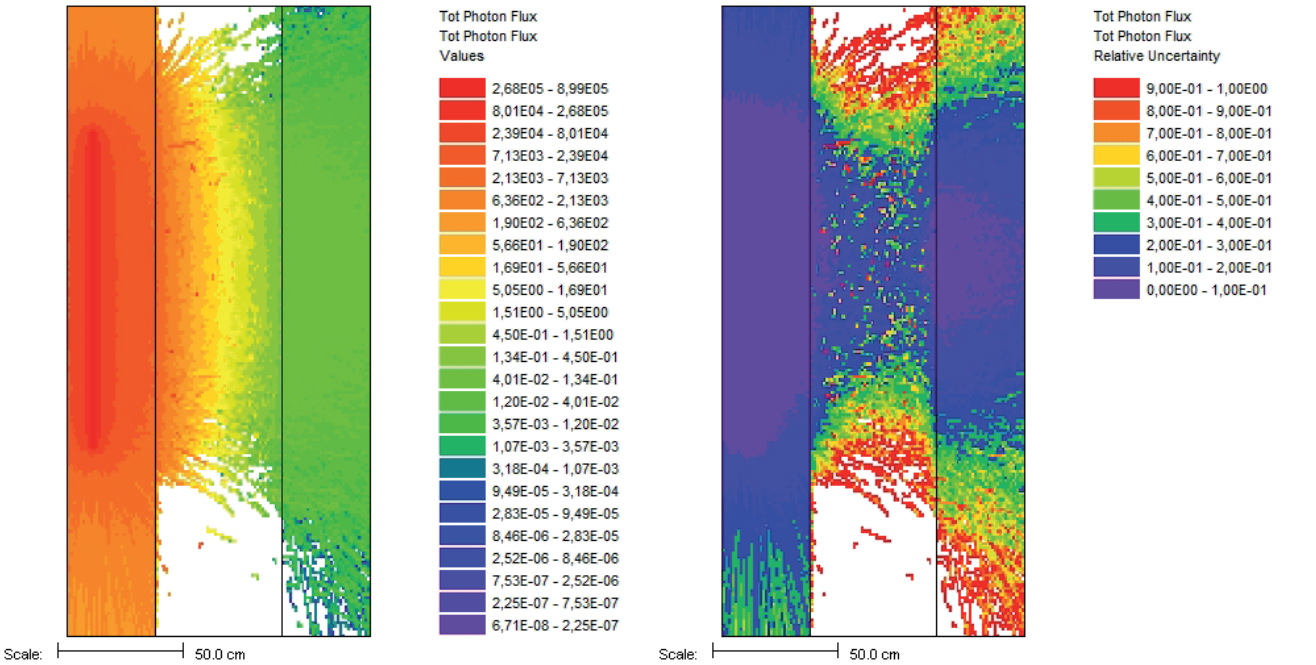

Fig. 16. CADIS solution for 10 MeV photons and 50 cm thick iron shield

VI. Conclusion

The application of point-kernel method to an isotropic gamma line, slab iron shield and isotropic point detector was demonstrated through theoretical and numerical approach. The developed point-kernel code can be run in command prompt by manually entering data or by GUI interface program which assists user with input data preparation. The benchmark test cases were compared to a reference MC solution, with varying iron shield thickness in cm (1, 5, 10, 20, 30, 40, and 50) and enveloping gamma ray energies with 0.5 MeV and 10 MeV, for which available buildup factors were used. A close agreement of obtained results was noticed for small to medium shield thicknesses and obtained numerical buildup factors showed excellent agreement with theoretical Goldstein and Taylor datasets. However, typical point-kernel "conservatism" was noticed only for uncollided gamma flux component while the total MC flux proved to be higher for most of test cases. These findings clearly demonstrate limitations of neglecting various photon transport processes inside the shield, which are more than compensated with only a fraction of CPU time needed for point-kernel flux solution with an acceptable deviation. Future work will expand program and GUI capabilities to other source geometrical forms and composite (multilayered) shields which require specific steps in obtaining so-called effective buildup factors of several different shielding materials.

Acknowledgement

The work was carried out as part of the project HRZZ-IP-2024-05-4011 of the Croatian Science Foundation.

References

[1] H. Khan, Use of Different Monte Carlo Sampling Techniques, RAND Corporation, P-766, 1955. As of May 23, 2024: https://www.rand.org/pubs/papers/P766.html

[2] B. G. Carlson, K. D. Lathrop, Transport theory – The Method of Discrete Ordinates, in: H. Greenspan, C. N. Kelber, D. Okrent (eds), Computing Methods in Reactor Physics, Gordon & Breach, New York, 1968.

[3] N.M. Schaeffer, Reactor Shielding for Nuclear Engineers, U.S. Atomic Energy Commission, Office of Information Services, 1973.

[4] T. Rockwel III (Ed.), Reactor Shielding Design Manual, USAEC Report TID-7004, 1956.

[5] H. Goldstein, Fundamental Aspects of Reactor Shielding, Reading, Mass., Addison-Wesley Pub. Co. 1959.

[6] S. Glasstone, A. Sesonske, Nuclear Reactor Engineering - Reactor Design Basics, Fourth Edition Volume One, Chapman & Hall, New York, 1994.

[7] M. Matijević, R. Ječmenica, D. Grgić, Spent Fuel Pool Dose Rate Calculations Using Point Kernel and Hybrid Deterministic-Stochastic Shielding Methods, *Journal of Energy*, 65 (2016), 1; 151-161.

[8] K. Trontl, D. Pevec, M. Matijević, Monte Carlo Codes for Neutron Buildup Factors, *Journal of Energy*, 62 (2013), 1-4; 171-179.

[9] P. Dučkić, K. Trontl, D. Grgić, M. Matijević, Point Kernel Modification Including Support Vector Regression Neutron Buildup Factor Models, *Journal of Energy*, 68 (2019), 2-3; 156-170.

[10] B.W. Kernighan, D.M. Ritchie, The C Programming Language, 2nd Edition, Prentice Hall, 1988.

[11] B. Stroustrup, The C++ Programming Language, Addison-Wesley Pub. Co. 2013.

[12] Qt documentation available at: https://doc.qt.io/

[13] "SCALE: A Comprehensive Modeling and Simulation Suite for Nuclear Safety Analysis and Design", ORNL/TM-2005/39, Version 6.1, June 2011. Available from Radiation Safety Information Computational Center at Oak Ridge National Laboratory as CCC-785.

Mario Matijević, Andrea Kaselj, Krešimir Trontl, Point-Kernel Shielding Applications of Sievert Integral, Journal of Energy, vol. 74 Number 4 (2025), 22–29
https://doi.org/10.37798/2025744729

Journal of Energy

VOLUME 74 Number 4 | 2025

journal homepage: http://journalofenergy.com/

Assessing the Impact of Transport Electrification on Distribution Networks - A Case Study of the Croatian Region of Istria

Tomislav Antić, Klemen Knez, Miljan Lenić, Anđelko Tunjić, Darko Hecer, Goran Jerbić, Lara Buljan, Denis Brajković, Zoran Pećarić

***Summary* — The increasing number of electric vehicles (EVs) introduces significant challenges for distribution networks planning and operation, including higher loading levels, voltage deviations, and potential transformer and line overloads. These challenges are amplified by the requirements of European Union Directive 2014/94/EU on alternative fuels infrastructure and Croatia's National Energy and Climate Plan for the period 2021–2030. This paper analyzes the impact of transport electrification on the distribution network of the Croatian region of Istria, selected due to its pronounced seasonality and specific geographical conditions. The analysis is based on a detailed network model consisting of nearly 2,500 medium to low voltage substations and more than 170,000 end users, incorporating real data on existing and planned charging stations, tourism related load variations, and EV growth projections. The methodology applies a k-medoids approach to identify representative low voltage networks, enabling the assessment of load increases and the identification of necessary grid reinforcements. The results show that EV growth combined with uncoordinated infrastructure deployment leads to voltage and current congestion. Based on these findings, the paper proposes a timeline of required investments, including conductor replacements and the construction of new and replacement of existing substations, to ensure reliable and efficient network operation as transport electrification progresses.**

***Keywords* — charging points, distribution networks planning, e-mobility, k-means clustering, network reinforcement**

(Corresponding author: Tomislav Antić).

Tomislav Antić is with University of Zagreb Faculty of Electrical Engineering and Computing, Zagreb, Croatia (e-mail: tomislav.antic@fer.unizg.hr).

Klemen Knez is with Faculty of Electrical Engineering, University of Ljubljana, Ljubljana, Slovenia (e-mail: klemen.knez@fe.uni-lj.si).

Darko Hecer is with Ekonerg Ltd., Zagreb Croatia (e-mail: dhecer@ekonerg.hr).

Lara Buljan and Goran Jerbić are with Institut za elektroprivredu d.d., Zagreb, Croatia (e-mail: lara.buljan@ie-zagreb.hr, goran.jerbic@ie-zagreb.hr)

Miljan Lenić, Anđelko Tunjić, Denis Brajković and Zoran Pećarić are with HEP-Operator distribucijskog sustava d.o.o., Zagreb, Croatia (e-mails: miljan.lenic@hep.hr, andelko.tunjic@hep.hr, denis.brajkovic@hep.hr, zoran.pecaric@hep.hr)

The research was funded by the European Union's NextGenerationEU programme, as part of the institutional project "Resilient Self-Healing Future Power Systems – RePowerFER," which is included in the programme agreement of the University of Zagreb Faculty of Electrical Engineering and Computing. The views and opinions expressed are solely those of the author and do not necessarily reflect the official position of the European Union or the European Commission. Neither the European Union nor the European Commission can be held responsible for them.

I. Introduction

Accelerated electrification of road transport, driven by environmental protection policies, represents one of the major challenges of today for European distribution system operators, including the Croatian DSO. The increasing number of electric vehicles (EVs) leads to higher electrical loads and electricity consumption, which may pose significant challenges for the planning and operation of distribution networks. These emerging challenges increase pressure on both transmission and distribution networks and can cause network congestion, ultimately resulting in interruptions in electricity supply. The impact is also evident in other sectors, such as construction, particularly in the development of new residential buildings and urban areas. Such issues are already observable in Western European countries with a high penetration of electric vehicles, such as the Netherlands [1].

Despite these challenges, transport electrification continues to be actively promoted, and the number of EVs has been increasing over the years, as reported by the International Energy Agency [2]. Further growth in the EV fleet is expected in 2025; however, projections indicate a slowdown in growth, reaching 7.7% in 2025 compared to 48% in 2024 [3]. One of the reasons for the reduced growth rate is the insufficient development of charging infrastructure, specifically, an inadequate number of charging stations that cannot meet overall charging demand, which significantly affects endusers' decisions to invest in EVs due to convenience concerns and potential travel challenges [4]. To address this issue, the European Union adopted the Regulation on the deployment of alternative fuels infrastructure, which defines targets for the construction of charging stations for light- and heavy-duty EVs along roads belonging to the core and comprehensive transport networks [5]. The regulation considers the period up to 2035 and periodically specifies increases in installed charging power at each designated charging location. This regulation is not the only EU document addressing electromobility. The European Green Deal identifies 2035 as the target year for achieving zero emissions from passenger vehicles and establishes the need for significant CO_2 emission reductions by 2030 [6].

In addition to EU-level policies, the importance of electromobility is also reflected in national legislation in Croatia. The update of the Integrated National Energy and Climate Plan for the Republic of Croatia from 2025 [7] provides detailed measures related to road vehicles, charging infrastructure, and the deployment of zero-emission technologies and associated infrastructure in rail transport, seaports, and airports. This plan has been positively assessed by the European Commission with certain steps already being implemented.

Tomislav Antić, Klemen Knez, Darko Hecer, Lara Buljan, Miljan Lenić, Anđelko Tunjić, Denis Brajković, Zoran Pećarić, Assessing the Impact of Transport Electrification on Distribution Networks - A Case Study of the Croatian Region of Istria, Journal of Energy, vol. 74 Number 4 (2025), 30–40
https://doi.org/10.37798/2025744733

Beyond high-power charging stations installed along major transport corridors, the growth in EV adoption requires the development of charging infrastructure in the parking areas of both residential and non-residential buildings. Amendments to construction legislation define the requirement for installing charging stations and ensuring the availability of cable infrastructure to enable future EV charger deployment in parking facilities in Croatia [8] but also in other European countries, e.g., the United Kingdom [9]. For residential EV chargers, clearly defined rules and guidelines are still lacking; however, relevant standards specify typical charger power ratings and grid connection requirements [10]. Consequently, it can be expected that the connection of EV chargers to residential low-voltage networks may lead to current and voltage-related network issues, as demonstrated in several analyses reported in the published [11], [12]. These papers assess the impact of transport electrification on real-world case studies defined for Croatia and Malta and also propose solutions related to the operation domain that might help DSOs to resolve voltage and current issues that occur when EVs integration is uncoordinated.

Technical challenges in distribution networks caused by accelerated transport electrification can be mitigated through proper distribution network development planning and investment in upgrading network components in areas affected by increased EV charger penetration. The importance of such analyses has been recognized by the Croatian DSO, motivating comprehensive assessments of the impact of electromobility on distribution networks. Regions with strong seasonal demand variations, such as tourist areas, are of particular interest due to higher expected EV usage by visitors from countries with already high EV adoption rates. As a result, the impacts of transport electrification in such regions are expected to be more pronounced than in other parts of the country.

In the literature, solutions addressing technical challenges in electric vehicle (EV) charging tend to focus on operational management and reactive problem-solving, rather than on anticipation and prevention. Common approaches include vehicle-to-grid (V2G) strategies [13] and smart, price-based charging schemes [14]. However, these methods largely remain confined to the research domain, as their practical implementation is limited by factors such as insufficient financial incentives and potential user discomfort. Furthermore, many proposed solutions lack robustness, as they are difficult to replicate or generalize across different case studies.

This paper presents a structured methodology for assessing the impact of electric mobility on distribution networks, with a particular focus on anticipating and mitigating EV-related technical issues. The paper summarizes key findings of "The Impact of Transport Electrification on the Development of HEP ODS's Distribution Network: A Case Study of the Elektroistra Pula Distribution Area" [15] and builds on top of our previous work presented in [16], [17], [18]. Unlike previous studies that primarily address operational problems, our approach operates in the planning domain, projecting the growth of EVs and analyzing grid conditions for relevant future years. By identifying potential current and voltage issues, we propose specific mitigation actions that distribution system operators (DSOs) should take to ensure network reliability. A central contribution of this work is a robust and transferable methodological framework: although the case study focuses on the Croatian distribution area of Istria, the methodology can be applied and replicated in other regions, providing a generalizable tool for proactive e-mobility planning.

The paper outlines the key steps defined within the methodology. Separate procedures are distinguished for MV and LV network analyses. Each section provides a detailed description of the corresponding methodological step, forming a comprehensive framework that supports future practical application.

Section 2 presents the detailed methodology, including the procedure for selecting representative LV network models, projections of EV growth and their contribution to network loading, and the calculation of the EV charging simultaneity factor. Section 3 describes the results of the LV network analysis, including a detailed example of the medoid network and the replication of these results across other LV networks within the same cluster. Section 4 summarizes the key findings for both MV and LV networks. Section 5 presents the methodology for assessing critical network assets, along with a detailed explanation of how the proposed approach can be applied to other distribution areas. Conclusions are provided in Section 7.

II. Methodology

A. Representative LV Network Models

The analysis of the impact of the growing number of electric vehicles on current and voltage conditions in the medium-voltage and low-voltage networks of the Elektroistra Pula distribution area is performed using network models that accurately reflect existing conditions. Models of the mediumvoltage network are available because this network is regularly planned and used in development studies and other planning analyses. In contrast, the low-voltage network is not examined in detail in development studies, and for a large part of the low-voltage system there are no models in planning simulation tools such as NEPLAN. However, low-voltage network data are documented in various DSO's and other databases, which enables the construction of low-voltage network models in specialized simulation tools using the available information.

An assessment of the collected data shows that the Elektroistra Pula distribution network contains more than 2,400 medium-voltage to low-voltage substations, each associated with a corresponding low-voltage network. Even after excluding 386 substations classified as part of the commercial group, more than 2,000 low-voltage networks remain to be modeled.

Modeling each network individually would be impractical, and for this reason a clustering procedure was applied to the available dataset. The main purpose of this procedure is to identify the low-voltage network whose characteristics best represent the networks within the same group or cluster.

Clustering provides a methodological simplification that primarily reduces the number of networks that must be modeled in NEPLAN, the tool used for all analyses in the referenced study [10]. This reduction is achieved by grouping networks into clusters according to the similarity of their technical attributes. The number of clusters is selected to achieve the highest possible level of internal similarity. For each cluster, one low-voltage network is chosen as the representative or average network, and this network is then modeled in NEPLAN. The total number of low-voltage networks modeled therefore corresponds to the number of clusters.

The clustering method applied in this study is the k-medoid method. Based on statistical processing, this method selects an actual low-voltage network from the dataset as the medoid, or the cluster center. This ensures that the representative network is a real system rather than a synthetic model created from average values of technical parameters. The k-medoid method is a classical clustering technique that partitions a set of n objects into k clusters, where the value of k is defined in advance. The objective is to minimize the dissimilarity of objects within a cluster relative to the representative medoid. Membership of an object in a cluster is determined by its distance from the medoid. Along with the ma-

Tomislav Antić, Klemen Knez, Darko Hecer, Lara Buljan, Miljan Lenić, Anđelko Tunjić, Denis Brajković, Zoran Pećarić, Assessing the Impact of Transport Electrification on Distribution Networks - A Case Study of the Croatian Region of Istria, Journal of Energy, vol. 74 Number 4 (2025), 30–40
https://doi.org/10.37798/2025744733

trix of objects and their characteristics, the algorithm must also be provided with the desired number of clusters.

1) Clustering algorithm: The input data for the algorithm consist of a matrix of objects with their associated characteristics. In the context of this analysis, the low-voltage networks represent the objects, while the selected technical parameters of the network represent the corresponding characteristics, that is, the coordinates of these objects. The dimensionality of the system is equal to the number of selected technical parameters used to evaluate similarity. Thus, if only two technical parameters are selected, each object occupies a position in a two-dimensional coordinate system; if three parameters are selected, the object is placed in a three-dimensional coordinate system, and so forth.

At the beginning of the procedure, the algorithm randomly selects a set of objects to serve as the medoids. The number of medoids is equal to the number of clusters specified by the user as an input parameter. All remaining objects are assigned to the medoid to which they are closest. The medoid together with its assigned objects forms a cluster, and the total number of clusters equals the number of medoids. The algorithm then randomly selects new candidate medoids and evaluates whether they are more suitable as final medoids. Suitability is determined by calculating the sum of distances between the medoid and the objects assigned to it, that is, the objects within the cluster. The medoids that minimize the total distance to their associated objects are selected as the final medoids.

The output of the algorithm consists of vectors representing the coordinates of the final medoids, along with the assignment of each remaining object to the corresponding medoid. In the context of this analysis, the final medoids represent actual lowvoltage networks, and the algorithm provides the classification of all remaining low-voltage networks into the appropriate medoid, that is, cluster. Fig. 1 presents a schematic illustration of the clustering algorithm described above.

2) Optimal number of clusters and selection of attributes: To apply the clustering algorithm, it is necessary to define the number of clusters within which the low-voltage networks will be grouped. Although the number of clusters may be chosen arbitrarily, such an approach raises concerns regarding the justification of the selected number, as the user may choose either too many or too few clusters. To avoid this issue, statistical methods such as the silhouette coefficient are used to determine the optimal number of clusters.

The silhouette method is particularly suitable for this analysis because it evaluates the similarity or cohesion of objects within their clusters in comparison with objects in other clusters, that is, their separation.

The silhouette coefficient is calculated for different numbers of clusters. In this study, the coefficient was computed for every value between 2 and 20. The highest silhouette coefficient was ob-tained for three clusters, indicating that this is the optimal number. It is important to note that the clustering process was not applied to the low-voltage networks previously assigned to the Commercial cluster.

As previously explained, clustering is performed based on available technical attributes that describe each low-voltage network. The known attributes include: rated MV/LV substation power, feeder length, share of overhead line length in total feeder length, impedance of the longest feeder section, total number of end-users' connections in the network, total end-users' connection power, average end-users' connection power per connection point, total annual electricity consumption, average annual consumption per connection point, total number of metering points, average number of metering points per connection point, and average an-nual consumption per metering point.

The silhouette coefficient was calculated for ten different com-binations of technical attributes. Although it may initially seem reasonable to use all available attributes, the statistical analysis in-dicates otherwise. Among all observed combinations, the lowest silhouette coefficient (0.26) was obtained when all attributes were used. The highest value (0.51) was achieved for the combination of attributes rated MV/LV substation power, share of overhead line length in total feeder length, and average annual consumption per metering point.

Clustering using these three attributes resulted in three clusters. A detailed examination of the networks in each cluster shows that they correspond to the following categories: »Urban networks – houses«, »Urban networks – buildings«, and »Rural networks«.

The »Urban networks – buildings« cluster contains a total of 643 low-voltage networks. These networks are characterized by higher substation installed power, a lower share of overhead lines, and generally higher average annual energy consumption per con-nection point.

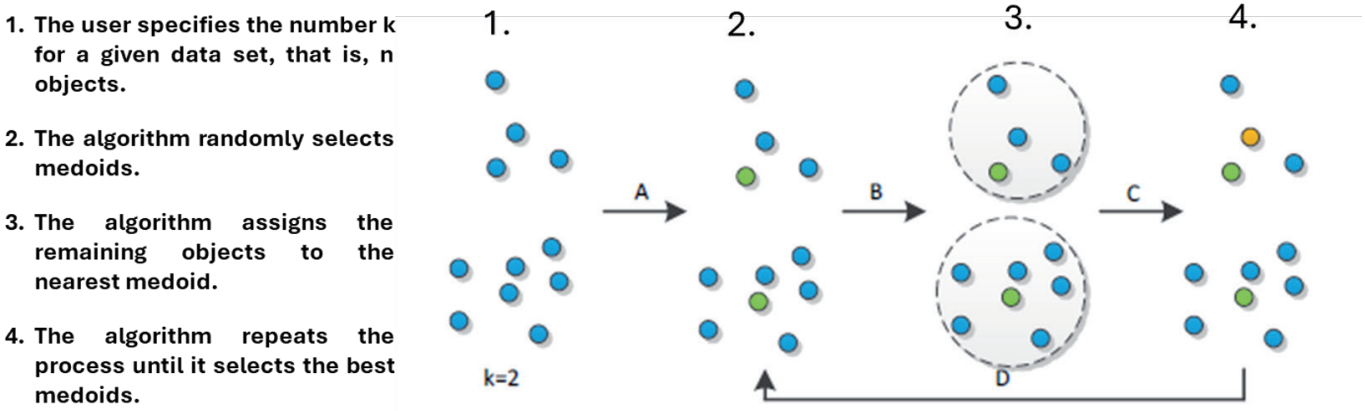

Fig. 1. Clustering approach

Tomislav Antić, Klemen Knez, Darko Hecer, Lara Buljan, Miljan Lenić, Anđelko Tunjić, Denis Brajković, Zoran Pećarić, Assessing the Impact of Transport Electrification on Distribution Networks - A Case Study of the Croatian Region of Istria, Journal of Energy, vol. 74 Number 4 (2025), 30–40
https://doi.org/10.37798/2025744733

The »Urban networks – houses« cluster contains 625 low-voltage networks. These networks have somewhat lower installed transformer power, a slightly higher share of overhead lines, and lower average annual consumption per connection point. The »Rural networks« cluster consists of 772 low-voltage networks. These networks are characterized by low installed transformer power, a high share of overhead lines, and low average annual consumption per connection point. Also, 386 networks were not part of the clustering algorithm and were predetermined as the industrial type of network based on the information from the DSO.

B. Projection tf the Increase in the Number of Electric Vehicles in the Area of Istria

To determine the contribution of electromobility to the increase in load in the area of Istria, it is necessary to create a projection of the growth in the number of electric vehicles over the observed period. The process of determining the increase in the number and total power of charging stations for electric vehicles in Istria consists of three main steps.

The first step concerns establishing the current situation, and involves detailed research of available data aimed at identifying the main characteristics of Istria in terms of vehicles—both those using fossil fuels and electric ones. A comprehensive approach is used, meaning that the population structure and seasonal patterns are analyzed, given the strong influence of tourism in the region. Additionally, publicly available demographic data, statistics from tourist boards, data from the Croatian Auto Club (HAK) and motorway operators regarding traffic flows are used. To obtain the most accurate data on the current state of electromobility in Istria, available electric vehicle charging curves are also utilized. All relevant documents that provide a solid foundation and discuss plans for introducing electric vehicles are taken into consideration.

The second step involves assessing future trends and determining projections for the coming period based on the situation established in the previous step and the expected increase in the share of various types of electric vehicles and vessels over a twenty-year period. For specific projections, in addition to the increase in the share of electric vehicles, demographic developments and tourism growth in the region are also considered. To enable more precise modeling, a wide range of literature and reference materials is taken into account. This includes the European Union's plans for promoting electromobility, historical population trends in Istria, the penetration rate of electric vehicles in the Republic of Croatia, as well as in the countries from which tourists visiting Istria most commonly arrive.

The third step focuses on segmenting the overall observed period of the next twenty years. Initially, a series of microanalyses are carried out for one-year intervals for the first ten years of the observed timeframe, while the second ten-year period is based on somewhat broader five-year estimates.

Additionally, it is important to closely examine certain statistical indicators characteristic of Istria and on which the projection must be based. The first indicator relates to the total number of vehicles in Istria, consisting of vehicles owned by the local population and vehicles brought by tourists. As mentioned earlier, one reason for choosing Istria for this analysis is the number of tourists—particularly those from developed countries where the rate of electromobility is already significant. Besides the number of cars, demographic parameters such as the number of inhabitants and tourism indicators such as the number of arrivals and overnight stays are also observed. Along with statistical parameters, it is necessary to review relevant documents from the European Union and the Republic of Croatia, such as EU regulations on the deployment of alternative fuel infrastructure or the Integrated National Energy and Climate Plan.

Furthermore, information on the LV (low-voltage) network is required, especially for determining the growth in the number of lower-power charging stations, given that the projection for the LV network is carried out separately for each cluster and then scaled to the level of the entire distribution area. Fig. 2 and Fig. 3 show the results of the projection for the observed twenty-year period. It is important to note that the projection corresponds to the area of Istria and that, in the case of analyzing another area, it must be adjusted to match the characteristic indicators of that area.

It should be noted that changes in the European and

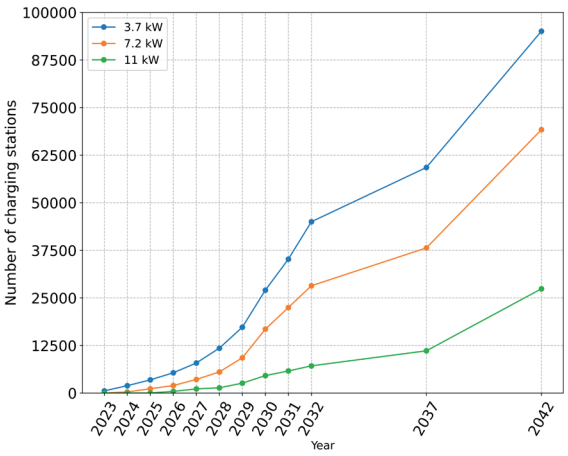

Fig. 2. Projection of the EV charging stations increase - 3.7 kW, 7.2 kW, 11kW

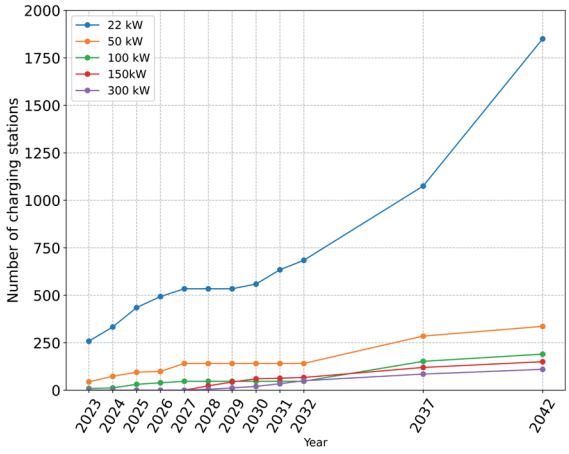

Fig. 3. Projection of the EV charging stations increase - 22 kW, 50 kW, 100 kW, 150 kW, 300 kW

Croatian regulatory environments may affect the projection results, which would directly influence the contribution of EV charging to peak demand and the timing of potential technical issues. Consequently, conclusions regarding the specific year in which network reinforcements are required may change. However, beyond identifying the timing of necessary investments, the projections also define the demand levels at which such actions become necessary. Therefore, even if the growth in the number of EVs is delayed or occurs earlier than expected, distribution system operators (DSOs) can monitor the total installed EV charging power and implement the same mitigation measures accordingly.

Tomislav Antić, Klemen Knez, Darko Hecer, Lara Buljan, Miljan Lenić, Anđelko Tunjić, Denis Brajković, Zoran Pećarić, Assessing the Impact of Transport Electrification on Distribution Networks - A Case Study of the Croatian Region of Istria, Journal of Energy, vol. 74 Number 4 (2025), 30–40
https://doi.org/10.37798/2025744733

C. EV CHARGING SIMULTANEITY FACTOR

After determining the installed power of aggregated charging stations at each MV node, it is necessary to determine the simultaneity factor of electric vehicle charging. The simultaneity factor must be defined because the probability that all charging stations are loaded at a level equal to their installed power is extremely low. The simultaneity factor $k_{EV,i}^{simultaneity}$ is defined as the ratio of the charging power at a given moment to the total installed power of the charging infrastructure, as defined with eq. (1).

$$k_{EV,i}^{simultaneity} = \frac{S_{EV,i}^{charging}}{S_{EV,i}^{installed}} \quad (1)$$

The simultaneity factor is determined separately for each cluster, since the level of transport electrification as well as the characteristic charging power differ for each cluster. For the purposes of the analyses conducted within the study, two scenarios are defined:

- High simultaneity factor scenario (Scenario 1)
- Scenario with the simultaneity factor defined based on real data (Scenario 2)

In Scenario 1, the simultaneity factor for all clusters is equal to 1. Since the study considers the case of maximum system loading, a simultaneity factor of 1 corresponds to the maximum theoretical utilization of an individual charging station, i.e., the case in which the maximum charging power is equal to the installed power of the charging station. This is also the case in which EV charging power contributes the most to the total system load. As the system load is also defined as maximum, in Scenario 1 the highest voltage drop values as well as the highest current loading of transformers and lines/cables in the observed distribution network can be expected. Furthermore, if no current–voltage issues occur in this case, they will not occur in any other case either.

Given that the scenario with $k_{EV,i}^{simultaneity} = 1$ represents a worst-case scenario and it is not realistic to expect the charging power to be equal to the installed power of each charging station, a more realistic case needs to be defined. Although it is possible to determine the simultaneity factor for each cluster using a rule-of-thumb approach, the charging simultaneity factors were determined based on real data available in the literature. Data were found for two clusters—«Urban networks – houses« and »Urban networks – buildings«. The data for houses are based on Denmark, while the data for buildings are based on Norway. Finally, data from Finland were used to calculate the simultaneity factor for the cluster »Industrial/commercial networks« Denmark and Norway are among the leaders in transport electrification and the share of electric vehicles, and as such represent a good example of what can be expected in the Istria region, where a somewhat higher number of electric vehicles is anticipated due to tourism compared to the rest of the Republic of Croatia. Simultaneity factors different from 1 also indicate that it is not necessary to ensure simultaneous charging of all electric vehicles. Although the existing infrastructure may be sufficient to allow all electric vehicles to charge without waiting, such a situation is not realistic and does not need to be guaranteed. This also means that not all parked electric vehicles require charging at the same moment.

Values of calculated simultaneity factors for each cluster, with the reference to the original data which was the basis for the factor calculation are presented in Table I.

TABLE I.
EV CHARGING SIMULTANEITY FACTOR OF DIFFERENT CLUSTERS

Cluster	Value	Reference country	Reference
Urban networks - houses	0.385	Denmark	Multiple sources
Urban networks - buildings	0.218	Norway	[19]
Rural networks	0.367	Germany	[20]
Industrial/commercial networks	0.192	Finland	[21]

III. LOW VOLTAGE NETWORK RESULTS

After defining the medoids of the LV networks, the growth of the base load, the increase in load due to the connection of EV charging stations, the increase in load due to the connection of heat pumps, and the increasing impact of distributed generation, it was necessary to proceed with the analysis of the medoid networks over the observation period. For each year of the observed period, an analysis of each medoid was carried out using the Neplan software package. In order to identify network congestion, checks were performed on MV/LV transformer loading, line loading, and voltage drops. For the identified congestion issues, the necessary mitigation measures were defined. This analysis was repeated for medoids in all cluster, however, in this paper we only present the results for one representative cluster, »Urban networks - houses«.

Fig. 4 presents the most important results of the analysis conducted for the medoid LV network. The figure shows the total electricity demand, along with the contributions of household baseline demand, photovoltaic (PV) generation, HVAC systems, and EV charging. It also indicates the nominal power of the transformer. Unlike all other demand sources, the contribution of PVs is zero, as the period under consideration corresponds to peak demand during evening hours, when there is no PV generation. This period also represents the worst-case scenario for the distribution network. In addition, the years in which voltage and current congestion occur, as well as the year in which the transformer needs to be replaced, are shown.

Total electricity demand exceeds the transformer's nominal power in 2030, and replacement of the installed 250 kVA transformer with a 630 kVA unit is recommended, as demand surpasses 400 kVA—the next typical transformer rating after 250 kVA. In addition to transformer replacement, upgrading lines and/or cables in the LV network is also necessary. Such replacements are required due to either voltage or current congestion. The results indicate that voltage drops exceed 10% in 2033 and 2034, while line currents surpass the lines' ampacity in 2037.

The analysis results from a locational perspective are presented in Fig. 5, showing both current and voltage congestion. Areas marked at the beginning of the network highlight lines and cables most affected by the increased power demand from EV charging. Since the highest power flows through the initial lines, these observations are expected. The marked area at the end of the network identifies nodes experiencing the largest voltage drops, i.e., the lowest voltage magnitudes. This location of minimum voltages is also expected due to the unidirectional power flow and the natural voltage decrease with increasing electrical distance.

Tomislav Antić, Klemen Knez, Darko Hecer, Lara Buljan, Miljan Lenić, Anđelko Tunjić, Denis Brajković, Zoran Pećarić, Assessing the Impact of Transport Electrification on Distribution Networks - A Case Study of the Croatian Region of Istria, Journal of Energy, vol. 74 Number 4 (2025), 30–40
https://doi.org/10.37798/2025744733

A. Projecting medoid results on other LV networks within a cluster

The results of the analysis of LV networks apply exclusively to the medoid of each cluster. Although there are certain similarities between the medoid and the other networks within the cluster, they also differ in many respects. For this reason, the conclusions drawn for the medoid cannot be directly transferred to all other networks within the cluster.

Based on the differences in technical attributes between the medoid and the other networks in the cluster, the analysis results can be projected in a way that accounts for these differences. In this way, an investment will not always be proposed in the same year; instead, it will change depending on the technical attributes of each LV network.

To make the medoid's results applicable to all other networks within the cluster, it is necessary to design and define a methodology that would adapt the medoid's results to any other network, taking into account its specific characteristics. During the analysis, three indicators of the need for investment in the network were defined: transformer overload, exceeding the current load of lines/cables, and an excessively high voltage drop.

B. Replacement of MV/LV transformers

For determining the replacement year of MV/LV transformers, no methodological approach is required; in other words, the year can be determined independently of the medoid results, based on other known data. For each transformer, its rated power is known. The annual load growth has been determined, as well as the additional increase in load caused by the integration of air conditioners and heat pumps, and electric vehicle charging stations. Using these data, it is possible to determine the load of each LV network according to eq. (2):

$$S^{load}_{total,year} = S^{load}_{base,year} + S^{load}_{HVAC,year} + S^{load}_{EV,year} \qquad (2)$$

By comparing the total load of the network with the rated power of the substation, it is possible to determine whether the transformer needs to be replaced in the observed year, i.e., whether the

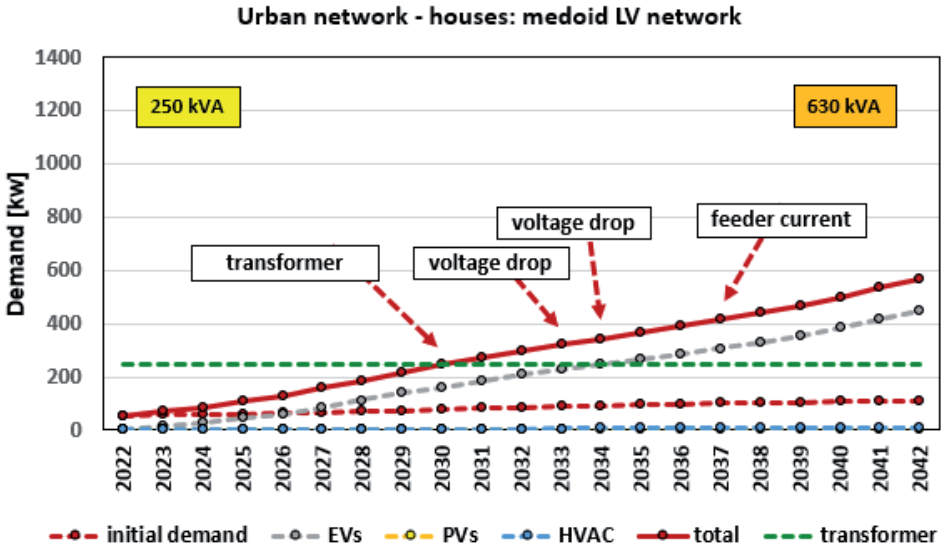

Fig. 4. Congestion location in the medoid LV network

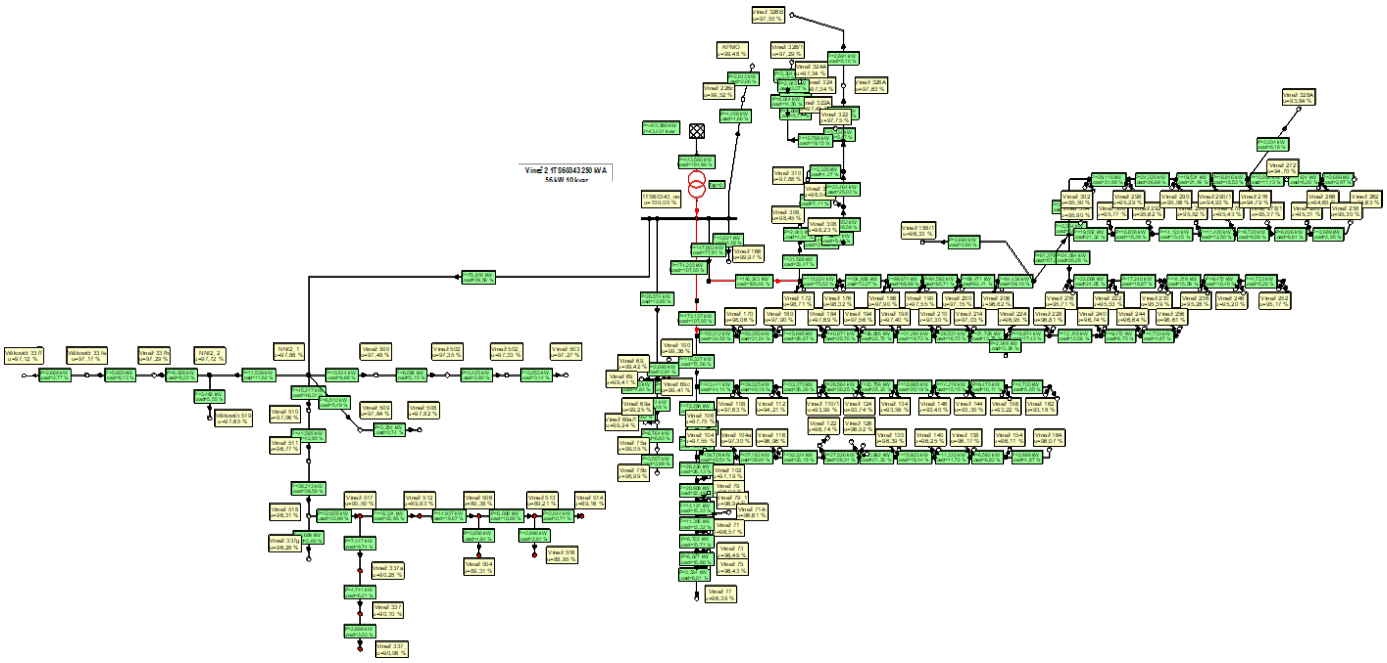

Fig. 5. Congestion location in the medoid LV network

Tomislav Antić, Klemen Knez, Darko Hecer, Lara Buljan, Miljan Lenić, Anđelko Tunjić, Denis Brajković, Zoran Pećarić, Assessing the Impact of Transport Electrification on Distribution Networks - A Case Study of the Croatian Region of Istria, Journal of Energy, vol. 74 Number 4 (2025), 30–40
https://doi.org/10.37798/2025744733

condition in eq. (3) is satisfied:

$$S_{total,year}^{load} \geq S_{nominal,year}^{MV/LV\,substation} \quad (3)$$

The potential replacement of transformers in substations is considered for each year, meaning that a replacement will not be proposed solely on the basis of the network load in the final year. For example, if the total network load in 2027 is 430 kVA, and the rated power of the transformer is 400 kVA, the first transformer replacement will occur in 2027, and the 400 kVA transformer will be replaced with a 630 kVA unit. Then, the network load in subsequent years will be observed to determine whether there is a year in which the load exceeds the new rated power of the transformer. In this paper, the results of replicating the results for themedoid LV network on other networks in a cluster will be shown only for the cluster »Urban networks – houses«, since the methodology remains unchanged for the other clusters. Also, we present the results only for Scenario 2 as this is more realistic scenario that considers real-world EV charging patterns in defining simultaneity factor. Fig. 6 shows the results of the transformer replacement analysis for the cluster »Urban networks – houses«.

Based on the results of the analysis in Scenario 2, it is evident that there is a need for at least one replacement of a larger number of transformers, caused by the electrification of transport and the increase in the number of charging stations in low-voltage networks. In addition to transport electrification, the continuous growth in the number of air conditioners also contributes to the number of overloaded substations. The electrification of transport and heating and/or cooling requires the distribution system operator to invest in new transformers. These results enable investment planning by year, while it is up to the system operator to decide whether the proposed replacements will be carried out in cycles or whether only the final proposed replacement will be considered, with existing transformers replaced by those with the highest proposed capacity.

C. Replacement of Low Voltage Lines And Cables

The analysis of the need for investment in the replacement of lines in the LV network is somewhat more complex compared to the analysis for transformers, since it cannot be carried out solely on the basis of load values. The calculation of investment needs was made using the methodology presented in several previous studies that dealt with the similar problems. Methods in these studies assess the impact of the increasing number of different DERs on the distribution network. In these methods, projecting of medoid results to other networks within the cluster was performed based on the *kdU* factor, defined as the sum of all products of the connection point power and the sum of the impedances of the lines and/or cables leading from the substation to the connection point.

A similar approach was used in this study, where the *kdU* factor was also used to project medoid results, with its calculation adapted to the available data provided as input for the analysis. For LV networks, line and/or cable impedances were not determined in the initial step—only their lengths. More precisely, the corresponding attribute table contains only the total line length, and this value will be used in calculating the *kdU* factor.

Although the type of line or cable plays a significant role in the voltage drop value, the assumption is that each cluster uses standard line types with similar unit resistance and reactance values. For this reason, the *kdU* factor will depend more on line length than on the line and/or cable type.

In addition to network length, the total network load will also be used. The load has been pre-determined, and the same parameter was used in the analysis of required transformer replacement. The detailed mathematical formulation of the *kdU* factor is given in equations (3)–(6).

Equations (3) and (4) are commonly used to calculate the squared voltage drop magnitude ΔU_{ij} of a line *ij*, where S_j s the power at the endpoint of the line/cable, and Z_{ij} is the impedance of the line/cable calculated from the per-unit resistance and reactance values r_{ij} and x_{ij} and the line length l_{ij}. The *kdU* factor is calculated using equations (5) and (6) as the total voltage drop, i.e., as the sum of the demand *d* of all connection points CP $_{d\in CP}S_l$ and the sum of all impedance in the network. As already mentioned, the use of standardised components affects only the magnitude of the *kdU* factor. Assuming that the per-unit nominal impedance is approximately the same for all networks within the same cluster, i.e., it is a constant, its contribution to the *kdU* value will always be identical. In other words, although neglecting the exact value of impedance will change the factor, this change will be the same across all networks and will therefore not influence the conclusions drawn.

$$\Delta U_{ij} = S_j \cdot Z_{ij} \quad [V^2] \quad (4)$$

$$\Delta U_{ij} = S_j \cdot (r_{ij} + x_{ij}) \cdot l_{ij} \quad [V^2] \quad (5)$$

$$kdU = \sum_{d\in CP} S_l \cdot (r_{ij} + x_{ij}) \cdot \sum_{l\in L} l_{ij} \quad [V^2] \quad (6)$$

$$kdU = \sum_{d\in CP} S_l \cdot \sum_{l\in L} l_{ij} \quad (7)$$

The results of the medoid analysis provide insight into the years in which line and/or cable replacements are required, i.e., they provide information on the network investment cycles. For all years in which a replacement is needed, the medoid's *kdU* factor is calculated for the given year. Since lines and cables are replaced, after investing in new network elements, the network can handle a higher *kdU* value. For this reason, the medoid's *kdU* is calculated for each year in which a replacement is needed. For all other networks within the cluster, the *kdU* factor is calculated for each year. The annual *kdU* values are compared with the medoid's *kdU* values. A year in which a network's *kdU* exceeds the medoid's *kdU* in the year when investment is required is identified as the year when investment is necessary. This procedure is repeated as long as there are needs for investment in new network elements within the observed twenty-year period.

As in the case of the transformer replacement analysis, this report presents the results for the »Urban networks – houses« cluster in Scenario 2. Fig. 7 shows the results of projecting the medoid onto the other networks within the cluster. The results indicate a significant number of LV networks that require intervention already in the first year, even when the share of EVs is not yet substantial. This means that certain current–voltage issues can be expected in the initial state if a number of existing lines are not replaced. The need for replacing network elements in subsequent years is lower and increases gradually with time from the initial year, which is expected given the dynamics of EV growth. The majority of investments will be required over a period of more than 20 years, indicating that it is possible to avoid risks in operating distribution networks amid transport electrification.

Only one investment cycle in new lines and/or cables has been identified, given that the medoid results indicate that voltage drop issues occur during the period between 2032 and 2037, and for this

Tomislav Antić, Klemen Knez, Darko Hecer, Lara Buljan, Miljan Lenić, Anđelko Tunjić, Denis Brajković, Zoran Pećarić, Assessing the Impact of Transport Electrification on Distribution Networks - A Case Study of the Croatian Region of Istria, Journal of Energy, vol. 74 Number 4 (2025), 30–40
https://doi.org/10.37798/2025744733

five-year period a single *kdU* factor value was calculated. Considering the assumption that certain networks may potentially require an additional investment cycle, the number of networks for which the *kdU* factor in any year exceeds the medoid's factor in the final year will be determined. Since the medoid network does not experience current–voltage constraints in 2042, even for Scenario 1, the *kdU* factor calculated for that scenario will be used, as it is of a higher value. This approach ensures that fewer networks need to be analyzed in more detail. The results show that all 205 networks in which the *kdU* in the final year is higher than that of the medoid potentially require analysis over the other ten years of the observed period. There is a high probability that additional investment in line and/or cable replacement will not be necessary, particularly for 47 networks for which potential replacement falls within the period between 2037 and 2042.

IV. Analysis of System-Level Results

Based on the results of the MV network analysis, analyses of medoid LV networks and replication of those results on other networks within a cluster, system-level conclusions were made. The conclusions mostly relate to investments needed by the DSO, in terms of replacing existing assets and building new substations. Follwoing conclusions were made:

- The total number of HV/MV transformers in the Elektroistra distribution area is 36. The analysis shows that during the observed period, 19 transformers (53%) will need to be replaced, of which 11 replacements (60% of all planned) will occur in the last five-year period. The situation is somewhat more favorable for MV/MV transformers – out of a total of 59 transformers, 19 (32%) will need to be replaced.
- The total length of the 35 kV network in the analyzed distribution area is 133 km, including 72 km of overhead lines and 61 km of cable lines. According to the results, no investments will be needed in this network during the first 5 years. In the second five-year period, more than 40% of overhead lines will need to be replaced, while in the remaining period, almost the entire overhead network will be replaced. Cable lines will require investment only in the last 5 years, accounting for 7% of the total length.
- The total length of the 20 kV network is approximately 2,900 km, of which about 1,700 km are overhead lines and 1,200 km are cable lines. No additional investments are needed during the first 5 years. In the next 5 years, approximately 2% of overhead lines are planned to be replaced, while in the remaining period, an additional slightly more than 2% will need replacement. For cable lines, a total of 6% of the network is planned for replacement over the entire observed period.
- Based on the results, the following number of MV/LV transformers (total of 2,425) will need to be replaced during the study period:

  — 428 transformers (68%) in the »Urban networks – houses« cluster

  — 277 transformers (43%) in the »Urban networks buildings« cluster

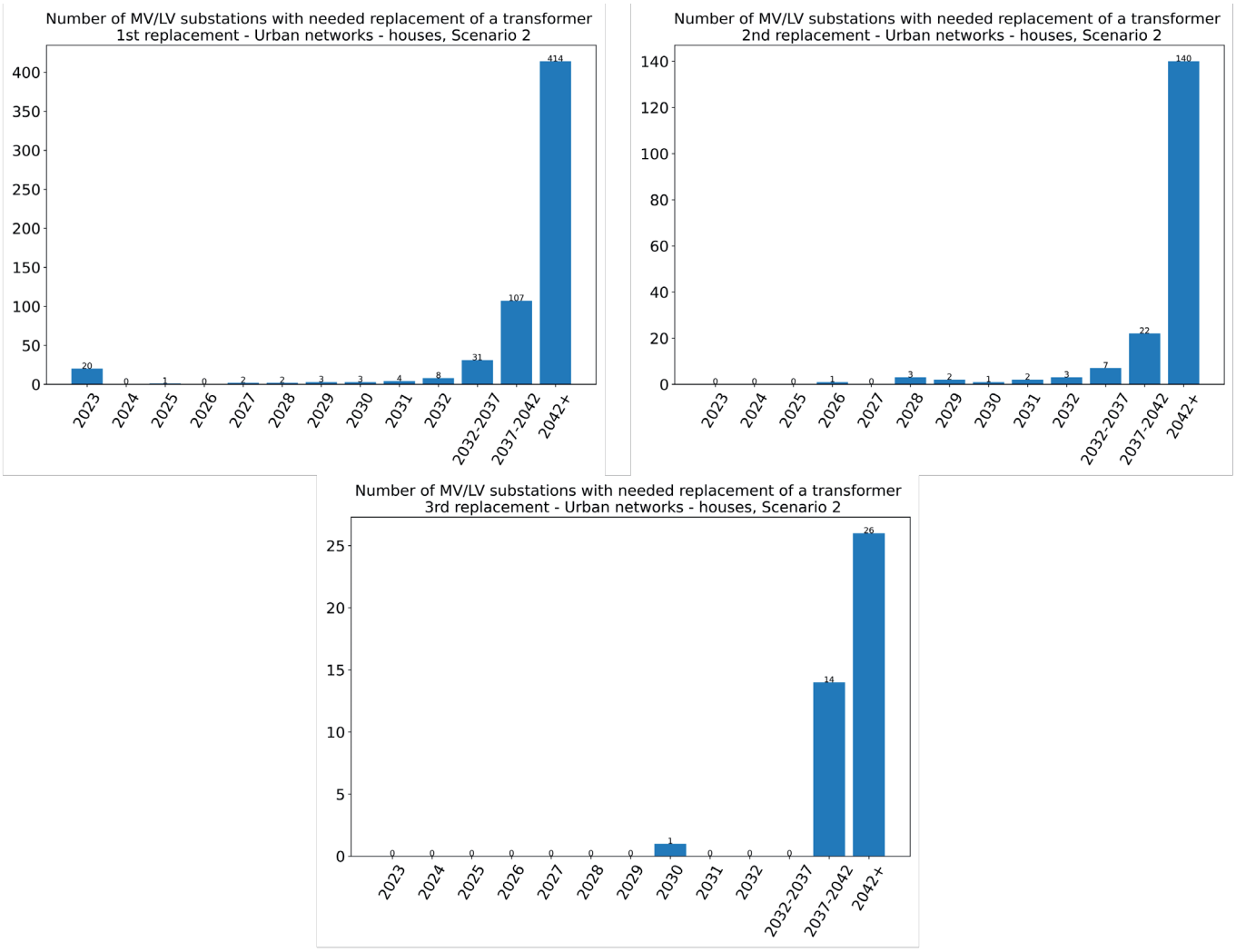

Fig. 6. Replacement of transformers in 20-year period: »Urban networks-houses« cluster

Tomislav Antić, Klemen Knez, Darko Hecer, Lara Buljan, Miljan Lenić, Anđelko Tunjić, Denis Brajković, Zoran Pećarić, Assessing the Impact of Transport Electrification on Distribution Networks - A Case Study of the Croatian Region of Istria, Journal of Energy, vol. 74 Number 4 (2025), 30–40
https://doi.org/10.37798/2025744733

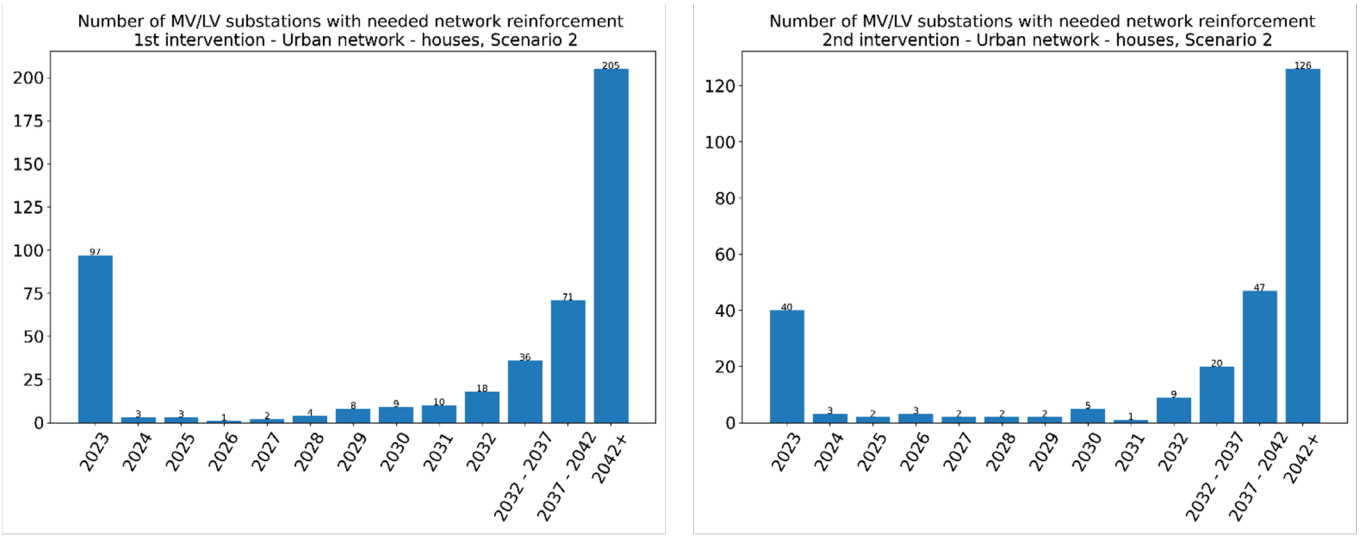

Fig. 7. Replacement of lines and cables in 20-year period: »Urban networks-houses« cluster

— 772 transformers (123%) in the »Rural networks« cluster

— 67 transformers (17%) in the »Industry/commercial« cluster

- The most unfavorable situation is in the »Rural networks« group, where multiple replacements of transformers are needed – the total number of replacements (123%) exceeds the number of existing units, indicating that some transformers must be replaced more than once, e.g., a 400 kVA transformer is first replaced with a 630 kVA transformer, and then later with a 1,000 kVA transformer. In this group, the highest number of replacements (623 transformers, i.e., 81%) is planned in the last five-year period. In the »Urban networks – houses« group, 225 transformers are planned to be replaced in the same period, which is 40% of all required replacements. In the other two groups, the situation is significantly better.
- The total length of the LV network in the Elektroistra Pula distribution area is approximately 4,500 km, of which about 2,000 km are overhead lines and 2,500 km are

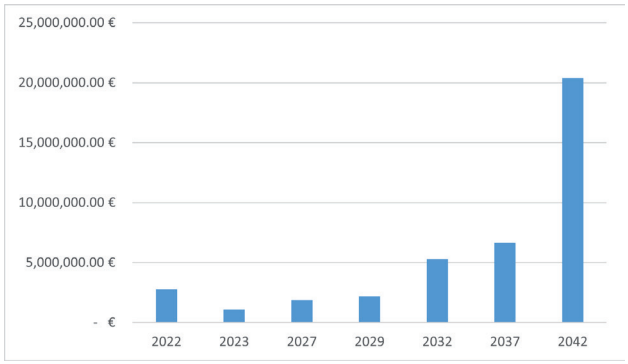

Fig. 8. Investment in MV/LV transformers in the 20-year period

cable lines. During the observed period, approximately 800 km of the network will need to be replaced, which represents 18% of the total length. The largest portion of investments concerns the »Urban networks – houses« cluster, where 564 km of the network will need to be replaced, accounting for more than 70% of all planned investments.

Furthermore, a financial analysis related to the replacement of existing MV/LV transformers was carried out, as shown in Fig. 8. The costs associated with replacing substations at the HV/MV and MV/MV levels are estimated at €52 million. Fig. 8 shows the growth of total costs for renewing MV/LV substations. By 2042, approximately €40 million will need to be invested in the renewal of these substations.

V. Methodology for Assessing the Critical Assets in MV and LV Networks

The aim of this study was not only to analyze the impact of the increasing number of EVs on current–voltage conditions in the Istria region, but also to define a unified methodology that would allow the application of the study results to other areas. The methodology for assessing the impact of EV growth on current–voltage conditions in the distribution network, i.e., the methodology for evaluating and identifying critical network assets, is described in this paper.

The results of the analysis show that the methodology can also be applied to other distribution areas if the defined steps are followed. Also, the methodology can be applied no matter the characteristics of networks in the observed area, after certain input parameters are modified to better reflect the actual state of networks. The analysis of the impact of transport electrification on the development of the distribution network is methodologically divided into the analysis of the MV network and the analysis of the LV network. These analyses can be conducted separately, independently of each other, although they are connected by certain input parameters, e.g., the projection of load growth, and documents relevant for assessing the number of EVs and the construction of the corresponding infrastructure.

Regardless of the voltage level of the distribution network, for each distribution area it is necessary, in the first step, to perform a legislative and regulatory analysis, as well as an analysis of certain demographic and economic indicators, in order to adapt the EV growth projection from the Istria region. The number of tourists in Istria significantly contributes to the expected acceleration of transport electrification, and such growth is not expected in other distribution areas. In addition, data on the initial load curve of a given distribution area are needed to enable the creation of a resultant load curve. The load curve is unique for each distribution area and serves as input data for further MV and LV network analyses.

Tomislav Antić, Klemen Knez, Darko Hecer, Lara Buljan, Miljan Lenić, Anđelko Tunjić, Denis Brajković, Zoran Pećarić, Assessing the Impact of Transport Electrification on Distribution Networks - A Case Study of the Croatian Region of Istria, Journal of Energy, vol. 74 Number 4 (2025), 30–40
https://doi.org/10.37798/2025744733

The MV network is analyzed in its entirety; that is, a detailed network model is used to assess the impact of transport electrification at the MV level. For this reason, the first step in the methodology is to analyze the configuration of the existing model of the MV network presented in a specialized distribution network simulation tool, e.g., NEPLAN. Network models are available in all distribution areas due to the preparation of development studies or other studies whose results are based on the MV network model.

It is to be expected that the existing model will always need to be adjusted, for example, due to the construction of new or decommissioning of existing substations, or due to adjusting peak load to actual conditions. Additionally, the existing NEPLAN model must be expanded by adding new elements that represent the load from EV charging stations, heat pumps, or solar power generation. The consumption and/or production power values are determined based on initial projections of peak load growth.

In the final step, the current–voltage conditions in the network model are analyzed for each selected year within the observed period. Based on these results, the need for investment in new transformers and lines, the need for constructing new and replacement of existing substations, and the dynamics of network investments are determined.

The analysis of the LV network is different, as presented in this paper. For numerous reasons, including the large number of LV networks in each distribution area, LV networks are not modeled in their entirety in the specified distribution network simulation tool. The simplified approach to modeling the LV network has several advantages, and for this reason, the methodology proposes such an approach also for application in not only the analyzed but also other distribution areas. In the first step of applying the methodology to LV network analysis, a clustering procedure must be carried out based on the available technical attributes. It is important to note that the number of clusters determined for the area analyzed in this paper does not necessarily have to be the same for other distribution areas. In addition to determining the optimal number of clusters, the clustering algorithm also produces a representative model of the LV network, i.e., the medoid of each cluster. A network model is created exclusively for the medoids, and the results of the analysis are generalized to all other LV networks within the same cluster. Generalizing the results, i.e., projecting the medoid results onto the other LV networks within the same cluster, is described in detail in the previous chapter. This step is also a key part of the methodology, as it enables the system operator to plan investments more effectively each year.

During the implementation of the steps in the methodology, certain conclusions were drawn that lead to recommendations for future application in other distribution areas. The quality of the analysis results largely depends on the availability and accuracy of the data, particularly data on the LV network, the determination of the necessary attributes, and the accuracy in identifying the medoid. These points are most closely related to the clustering procedure. Since this is a statistical analysis, a high-quality set of input data is a prerequisite for the accuracy of the process. In addition to input data, certain steps can further improve the accuracy of projecting the medoid results. Accuracy can be increased if clustering is performed at the branch level and if the medoid is defined as a branch rather than the entire network. Additionally, the impedance of the lines, as well as the number and average length of branches, should be taken into account. Finally, the calculation of the kdU factor can be modified to include the actual impedance, not just the line length. If all of these steps were implemented in the methodology, its future application would allow for even more accurate results and more precise analyses.

VI. CONCLUSION

This work demonstrates that the growth in electric vehicle (EV) numbers can lead to the exceedance of technical limits in the distribution network, including the need for transformer replacements and line upgrades. The results clearly identify critical sections of both medium-voltage (MV) and lowvoltage (LV) networks and the timing of required investments.

Beyond identifying potential issues, the study developed a methodology for accurately assessing the impact of transport electrification and planning necessary network investments. The methodology includes an analysis of the existing network state, demographic and economic indicators, regulatory frameworks, and projections of EV growth. MV network assessment uses a detailed full-network model, while LV network analysis employs clustering to define representative models (medoids), allowing results to be generalized across other networks within each cluster. Additional steps, such as accounting for line impedances and refining the kdU factor, enhance the precision of the analysis.

Timely and coordinated investments in both MV and LV networks can prevent adverse effects of increased electricity demand and ensure reliable network operation. The methodology can also be applied to other distribution areas, supporting a sustainable continuation of transport electrification in Croatia without compromising network reliability.

REFERENCES

[1] M. van Rossum du Chattel, "Netcongestie: elektrische auto's mogelijk helemaal niet meer opladen in Utrecht." https://www.rtvutrecht.nl/nieuws/3710260/netcongestie-elektrische-autos-mogelijk-helemaal-niet-meer-opladen-in-utrecht, 2024. [Accessed 10-12-2024].

[2] IEA, "Global ev outlook 2024," tech. rep., IEA, 2024.

[3] "Global automotive outlook: Predictions for 2025." https://www.forbes.com/sites/sarwantsingh/2025/01/13/global-automotive-outlook-predictions-for-2025/, 1 2025. [Accessed 10-12-2025].

[4] H. Pandzic, B. Franc, S. Stipetic, F. Pandzic, M. Mesar, M. Miletic, and S. Jovanovic, "Electric vehicle charging infrastructure in croatia – first-hand experiences and recommendations for future development," *Journal of Energy - Energija*, vol. 71, pp. 16–23, 6 2023.

[5] "Regulation (EU) 2023/1804 of the European Parliament and of the Council of 13 September 2023 on the deployment of alternative fuels infrastructure, and repealing Directive 2014/94/EU." https://eur-lex.europa.eu/legal-content/EN/TXT/HTML/?uri=CELEX:32023R1804, 2023.

[6] "The European Green Deal." https://eur-lex.europa.eu/legal-content/EN/TXT/HTML/?uri=CELEX:52019DC0640, 2019. [Accessed 18-12-2025].

[7] "Revised integrated national energy and climate plan for the republic of croatia." https://mzozt.gov.hr/UserDocsImages//KLIMA//NECP_Update%20_CRO_EN_FINAL.pdf, 2025.

[8] "Law on amendments to the construction law." https://narodne-novine.nn.hr/clanci/sluzbeni/2019_12_125_2489.html, 12 2019.

[9] "Public Charge Point Regulations 2023 guidance." https://www.gov.uk/government/publications/the-public-charge-point-regulations-2023-guidance/public-charge-point-regulations-2023-guidance, 2023. [Accessed 10-12-2025].

[10] S. S. G. Acharige, M. E. Haque, M. T. Arif, N. Hosseinzadeh, K. N. Hasan, and A. M. T. Oo, "Review of Electric Vehicle Charging Technologies, Standards, Architectures, and Converter Configurationsn," *IEEE Access*, vol. 11, pp. 41218–41255, 2023.

[11] T. Antić, T. Capuder, and M. Bolfek, "A comprehensive analysis of the voltage unbalance factor in pv and ev rich non-synthetic low voltage distribution networks," *Energies*, vol. 14, p. 30, 2021.

[12] B. Azzopardi and Y. Gabdullin, "Impacts of electric vehicles charging in low-voltage distribution networks: A case study in malta," *Energies*, 2024.

[13] Y. Hu, F. J. Bahamonde-Birke, and D. Ettema, "Vehicle-to-grid, why not? An interview with battery electric vehicle users with various driving patterns in Utrecht, the Netherlands," *Transport Policy*, vol. 164, pp. 231–240, 2025.

[14] F. Brockmann, R. S. Kohn, and M. Marinelli, "When smart charging meets smart users: How price-sensitive plug-in behavior reshapes EV integration," *Sustainable Energy, Grids and Networks*, vol. 44, p. 101977, 2025.

[15] "The Impact of Transport Electrification on the Development of HEP ODS's Distribution Network: A Case Study of the Elektroistra Pula Distribution Area (Utjecaj elektrifikacije prometa na razvoj distribucijske mreže HEP ODS-a na primjeru mreže distribucijskog područja Elektroistra Pula)," tech. rep., Ekonerg Ltd. and Institut za elektroprivredu d.d. and University of Zagreb Faculty of Electrical Engineering and Computing and Faculty of Electrical Engineering, University of Ljubljana, 2024.

[16] T. Antić, D. Hecer, M. Lenić, D. Brajković, L. Buljan, A. Tunjić, Z. Pećarić, G. Jerbić, K. Knez, H. Pandžić, and B. Blažić, "Methodology for assessing the impact of traffic electrification on the development of the hep ods distribution network," in *9th Conference of the Croatian Branch of the International Conference on Electricity Distribution (HO CIRED)*, 2025.

[17] T. Antić, D. Hecer, M. Lenić, D. Brajković, L. Buljan, A. Tunjić, Z. Pećarić, G. Jerbić, K. Knez, H. Pandžić, and B. Blažić, "Key results of the study "the impact of transport electrification on the development of hep ods's distribution network: A case study of the elektroistra pula distribution area"," in *9th Conference of the Croatian Branch of the International Conference on Electricity Distribution (HO CIRED)*, 2025.

[18] K. Knez, D. Hecer, M. Lenić, T. Antić, L. Buljan, A. Tunjić, Z. Pećarić, G. Jerbić, D. Brajković, H. Pandžić, and B. Blažić, "The impact of electromobility on the development of distribution networks in croatian istria," in *17th professional-scientific conference of HRO CIGRE*, 2025.

[19] Åse Lekang Sørensen, K. B. Lindberg, I. Sartori, and I. Andresen, "Residential electric vehicle charging datasets from apartment buildings," *Data in Brief*, vol. 36, p. 107105, 2021.

[20] S. Ali, P. Wintzek, and M. Zdrallek, "Development of Demand Factors for Electric Car Charging Points for Varying Charging Powers and Area Types," *Electricity*, vol. 3, no. 3, pp. 410–441, 2022.

[21] I. Jokinen and M. Lehtonen, "Modeling of Electric Vehicle Charging Demand and Coincidence of Large-Scale Charging Loads in Different Charging Locations," *IEEE Access*, vol. 11, pp. 114291–114315, 2023.

Tomislav Antić, Klemen Knez, Darko Hecer, Lara Buljan, Miljan Lenić, Anđelko Tunjić, Denis Brajković, Zoran Pećarić, Assessing the Impact of Transport Electrification on Distribution Networks - A Case Study of the Croatian Region of Istria, Journal of Energy, vol. 74 Number 4 (2025), 30–40
https://doi.org/10.37798/2025744733

Journal of Energy
VOLUME 74 Number 4 | 2025
journal homepage: http://journalofenergy.com/

Comparative Analysis of Metaheuristic Algorithms for Parameters Estimation of Single-Cage and Double-Cage Induction Machine Models

Mihailo Micev, Martin Ćalasan, Miljan Janketić

***Summary* — This paper deals with the estimation of parameters of single-cage and double-cage induction machine models using HBA (Honey Badger Algorithm) and EO (Equilbrium Optimizer) algorithms. The input data for the estimation procedure are the induction machine nameplate data – power factor, starting, rated, and maximum torque. Based on the nameplate data, the criterion function is defined. The applicability of both considered methods is proven by comparing the output characteristics of induction machine determined using parameters estimated with other literature known algorithm. The obtained results demonstrate that the applied algorithm is very efficient, accurate, and precise method for the parameters estimation of single-cage and double-cage induction machine models.**

***Keywords* — induction machine, estimation, parameters, metaheuristic algorithms.**

I. Introduction

Induction machine (IM) is the most common type of alternating current (AC) electric machine. The main characteristic of this machine type is that the rotor speed and the speed of stator's rotating magnetic field are not equal. Due to the fact that IMs cannot produce reactive power, they are mainly used as a motor.

The proper functioning of an IM is very important for every electrical drive, device or application in which the IM is used. In order to provide reliable and efficient operating of an IM, it is very important to know the parameters of the machine, as well as the current, torque, and other electrical and mechanical characteristics. The operation of an IM is defined with its' equivalent circuit and the values of the parameters. According to that, it is obvious that the determination of IM's parameters provides insight into the condition of the machine and the expected level of its' performances [1]. Classic method for IM's parameters estimation is based on the short-circuit and open-circuit tests, as described in IEEE and IEC standards [2], [3]. However, since there is practical need to estimate the parameters of IM during the normal operation mode, it is evident that the standard short-circuit and open-circuit tests are not applicable. Therefore, the authors in the available literature tend to develop the methods for estimation of IM's parameters which do not require the disconnection of the machine from the load. Generally, the developed methods for the estimation of IM parameters can be divided into two main categories. The first category comprises methods that rely on the IM's nameplate data, such as rated torque and slip, as well as starting and maximum torque [4] – [6]. On the other side, the second category of estimation methods relies on measuring the data during the normal operation mode of the machine [7] – [12]. To be more precise, the methods based on the analysis of the machine's acceleration are presented in [7] and [8]. The direct start of the induction machine represents the basic for the test method proposed in [9], while the U/f regulation is considered in [10]. The parameters of the IM are determined while operating in generator mode in [11]. Also, the impulse response of an IM is used for the parameters estimation procedure in [12].

This paper presents the comparative analysis between HBA [13] and EO [14] algorithms for estimation of parameters of single cage induction machine (SCIM) and double cage induction machine (DCIM) models. The parameters are estimated using the nameplate data. Also, the comparison with SA-ERWCA algorithm, used in [6], is provided.

The paper is organized as follows. In Section 2, both single cage and double cage induction machine models are described in details, along with the presentation of corresponding equivalent circuits. Considered metaheuristic algorithms are described in Section 3. The results of the estimation procedure, along with the comparative analysis, are presented in Section 4.

II. Single Cage and Double Cage Induction Machine Models

In this section, two basic models of induction machine are presented – single cage and double cage models. Also, equivalent circuits and corresponding mathematical equations will be analyzed.

A. Single cage model (SCM) of induction machine

The equivalent circuit of the single cage induction machine model is depicted in Fig. 1. The resistances of stator and rotor are denoted with R_1 and R_2, X_1 and X_2 stand for reactances of stator and rotor, respectively, X_m is magnetization reactance, and s is slip.

Corresponding author: Mihailo Micev
Mihailo Micev and Martin Ćalasan are with the University of Montenegro, Faculty of Electrical Engineering, Podgorica, Montenegro (emails: mihailom@ucg.ac.me; martinc@ucg.ac.me.
Miljan Janketić is with CEDIS, Montenegrin distribution system operator, Podgorica, Montenegro (email: miljan.janketic@gmail.com)

Mihailo Micev, Martin Ćalasan, Miljan Janketić, Comparative Analysis of Metaheuristic Algorithms for Parameters Estimation of Single-Cage and Double-Cage Induction Machine Models, Journal of Energy, vol. 74 Number 4 (2025), 41–46
https://doi.org/10.37798/2025743718

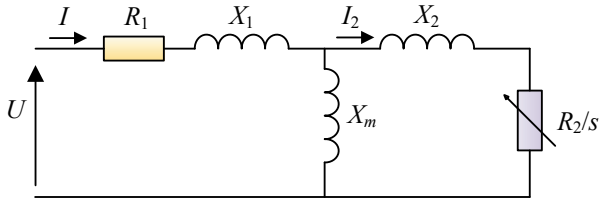

Fig. 1. Equivalent circuit of single cage induction machine model.

Based on the presented equivalent circuit, firstly the equivalent impedance of rotor circuit and magnetization branch Z_p is determined:

$$\underline{Z}_p = \frac{1}{\frac{1}{jX_m} + \frac{1}{\frac{R_2}{s} + jX_2}}. \tag{1}$$

Therefore, the stator current I can be determined as follows:

$$\underline{I} = \frac{\underline{U}}{R_1 + jX_1 + \underline{Z}_p}. \tag{2}$$

Knowing the stator current, the rotor's current I_2 can be easily determined:

$$\underline{I}_2 = \frac{\underline{Z}_p \cdot \underline{I}}{\frac{R_2}{s} + jX_2}. \tag{3}$$

Based on that, the electromagnetic torque of the motor can be calculated using the following equation:

$$T = \frac{3 \cdot p}{\omega_s} \cdot \left|\underline{I}_2\right|^2 \cdot \frac{R_2}{s}, \tag{4}$$

where p stands for the number of pole pairs of the machine, and ω_s is the synchronous speed. Starting torque, denoted as T_s, can be easily determined by including s=1 in (4). In order to determine the maximum value of torque T_{max}, the first step is to differentiate torque expression with respect to slip s, and to set the first derivative to be equal to 0:

$$\frac{dT}{ds} = 0. \tag{5}$$

The solution of (5) is the value of slip s_{max} that corresponds to maximum torque:

$$s_{max} = \frac{R_2}{\sqrt{R_{TH}^{\ 2} + \left(X_{TH} + X_2\right)^2}}, \tag{6}$$

where R_{TH} and X_{TH} correspond to resistance and reactance of the equivalent Thevenin circuit of single cage induction machine model:

$$\begin{aligned} &\underline{Z}_{TH} = \frac{\underline{Z}_1 \cdot \underline{Z}_p}{\underline{Z}_1 + \underline{Z}_p}, \underline{Z}_1 = R_1 + jX_1, \\ &R_{TH} = Re\left\{\underline{Z}_{TH}\right\}, X_{TH} = Im\left\{\underline{Z}_{TH}\right\}. \end{aligned} \tag{7}$$

Thevenin voltage V_{TH} is calculated as follows:

$$\underline{V}_{TH} = \underline{U} \cdot \frac{\underline{Z}_p}{\underline{Z}_1 + \underline{Z}_p}. \tag{8}$$

Finally, expressions for torque and maximum torque are obtained as follows:

$$\begin{aligned} T &= \frac{3 \cdot R_2 \cdot \left|\underline{V}_{TH}\right|^2}{s \cdot \omega_s \cdot \left(\left(R_{TH} + \frac{R_2}{s}\right)^2 + \left(X_{TH} + X_2\right)^2\right)}, \\ T_{max} &= \frac{3 \cdot \left|\underline{V}_{TH}\right|^2}{2 \cdot \omega_s \cdot \left(R_{TH} + \sqrt{R_{TH}^{\ 2} + \left(X_{TH} + X_2\right)^2}\right)}. \end{aligned} \tag{9}$$

B. Double Cage model (DCM) of Induction Machine

The equivalent circuit of the induction machine double cage model is given in Fig. 2.

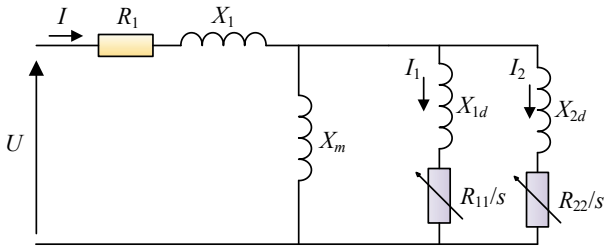

Fig. 2. Equivalent circuit of double cage induction machine model.

In the presented equivalent circuit, R_{11} and R_{22} represent the resistances of the first and second cage, while X_{1d} and X_{2d} stand for the reactances of the first and second rotor cage, respectively. Therefore, the stator current can be calculated as follows:

$$\underline{I} = \frac{\underline{U}}{R_1 + jX_1 + \underline{Z}_p}, \tag{10}$$

where the equivalent impedance of parallel branches Z_p is calculated using the following equation:

$$\underline{Z}_p = \frac{1}{\frac{1}{jX_m} + \frac{1}{\frac{R_{11}}{s} + jX_{1d}} + \frac{1}{\frac{R_{22}}{s} + jX_{2d}}}. \tag{11}$$

Based on the value of stator current, the currents I_1 and I_2 of the first and second rotor cages, respectively, are obtained:

$$\begin{aligned} \underline{I}_1 &= \frac{\underline{Z}_p \cdot \underline{I}}{\frac{R_{11}}{s} + jX_{1d}}, \\ \underline{I}_2 &= \frac{\underline{Z}_p \cdot \underline{I}}{\frac{R_{22}}{s} + jX_{2d}}. \end{aligned} \tag{12}$$

Afterward, the machine torque can be easily calculated:

$$T = \frac{3 \cdot p}{\omega_s} \cdot \left(\left|\underline{I}_1\right|^2 \cdot \frac{R_{11}}{s} + \left|\underline{I}_2\right|^2 \cdot \frac{R_{22}}{s}\right). \tag{13}$$

Similar to the approach presented within SCM analysis, the starting torque can be obtained by substituting s=1 in (13). Also, the value of slip s_{max} that corresponds to maximum torque is obtai-

Mihailo Micev, Martin Ćalasan, Miljan Janketić, Comparative Analysis of Metaheuristic Algorithms for Parameters Estimation of Single-Cage and Double-Cage Induction Machine Models, Journal of Energy, vol. 74 Number 4 (2025), 41–46
https://doi.org/10.37798/2025743718

ned by solving (5). After determining s_{max}, maximum torque T_{max} is obtained by substituting s=s_{max} in (13).

III. Description of Applied Metaheuristic Algorithms

In this section, the description and basic mathematical equations for two metaheuristic algorithms – HBA and EO algorithms- are provided.

A. Honey Badger Algorithm (HBA)

The honey badger algorithm is based on the social behavior of honey badgers, precisely on the search and locating of the food. From mathematical aspect, each badger is represented with vector $\boldsymbol{x}_i$=[x_{i1}, x_{i2},…, x_{iD}], where $\boldsymbol{x}_i$ is position of i-th badger, and i counts from 1 to N (N-population size). Also, D denotes the dimension of the optimization problem, or the number of variables that are being optimized. First step in the algorithm is to randomly initialize the position of each honey badger between the lower and upper bounds of the optimization variable:

$$x_{i,j} = LB_j + rand \cdot \left(UB_j - LB_j\right); i = 1,2,...,N;\ j = 1,2,...,D, \quad (14)$$

where *rand* stands for a random number between 0 and 1, while LB_j and UB_j are the lower and upper bound of j-th optimization variable, respectively. The main equations that iteratively repeat in the HBA algorithm are the digging phase and the honey phase. These equations are used to update the positions of the honey badgers.

The digging phase is expressed as follows:

$$\boldsymbol{x}_{new} = \boldsymbol{x}_{prey} + F \cdot \beta \cdot \boldsymbol{I} \cdot \boldsymbol{x}_{prey} + F \cdot r_3 \cdot \alpha \cdot \boldsymbol{d}_i \cdot |cos(2\pi r_4) \cdot [1 - cos(2\pi r_5)]|, \quad (15)$$

where $\boldsymbol{x}_{new}$ stands for the updated position of each honey badger, $\boldsymbol{x}_{prey}$ is the best badger so far (the one with the lowest criterion function value); r_3, r_4, and r_5 are random numbers in range from 0 to 1, and β is the ability of the badger to get food – according to [13], it is selected to be 6.

The other factors mentioned in (15), are defined as follows:

- $\boldsymbol{I}_i$ is smell intensity of the prey:

$$\boldsymbol{I}_i = r_2 \times \frac{\boldsymbol{S}}{4\pi \boldsymbol{d}_i^2}, \quad (16)$$

- $\boldsymbol{S}$ is strength source:

$$\boldsymbol{S} = \left(\boldsymbol{x}_i - \boldsymbol{x}_{i+1}\right)^2, \quad (17)$$

- $\boldsymbol{d}_i$ is distance between prey and i-th badger:

$$\boldsymbol{d}_i = \boldsymbol{x}_{prey} - \boldsymbol{x}_i, \quad (18)$$

- α is density factor:

$$\boldsymbol{a} = e^{-\frac{t}{t_{\max}}}, \quad (19)$$

- F is flag, defined as follows:

$$F = \begin{cases} 1, \text{if } r_6 \le 0.5 \\ 1, \text{else} \end{cases} \quad (20)$$

In previous equations, r_2 and r_6 are random numbers between 0 and 1, while t and $t_{\max}$ stand for current and maximum number of iterations, respectively.

After completing digging phase, the following step in HBA is honey phase. It is described using (21):

$$\mathbf{x}_{new} = \mathbf{x}_{prey} + F \cdot r_7 \cdot \alpha \cdot \mathbf{d}_i. \quad (21)$$

The described procedure is iteratively repeated until the algorithm reaches predefined maximum number of iterations t_{max}. After completing the last iterations, the solution of the optimization problem is the honey badger with the lowest criterion function value.

B. Equilibrium optimizer (EO) algorithm

The inspiration for equilibrium optimizer (EO) algorithm is found in the law related tothe mass balance, which is frequently mentioned in chemistry and physics. Similar to the previously described HBA, the population of EO algorithm is presented as the population of N particles. The concentration of i-th particle, denoted as $\boldsymbol{C}_i$, represents a potential solution of the optimization problem, and is presented as vector of D variables. The first step of the algorithm is to randomly initialize the population, which is carried out using (14). Afterward, the iteration procedure begins, and it is carried out until maximum number of iterations t_{max} is reached. In each iterations, the concentration of every particle is updated as

$$\boldsymbol{C}_i(t) = \boldsymbol{C}_{eq} + \left(\boldsymbol{C}_i(t-1) - \boldsymbol{C}_{eq}\right) \cdot \boldsymbol{F} + \frac{\boldsymbol{G}}{\boldsymbol{\lambda}}\left(1 - \boldsymbol{F}\right). \quad (22)$$

The explanation of each term from previous equation is given as follows:

- Randomly chosen particle from equilibrium pool is denoted as $\boldsymbol{C}_{eq}$. The equilibrium pool is formed once after each iteration – it consists of four best particles of the population, and of the their average value.
- The exponential term is denoted as $\boldsymbol{F}$. Taking into account that $\boldsymbol{\lambda}$ (turnover rate) represents vector of random numbers in the range from 0 to 1, the exponential term can be calculated as follows:

$$\begin{aligned} &\boldsymbol{F} = e^{-\lambda(x - x_0)}, \\ &\boldsymbol{x} = \left(1 - \frac{t}{t_{\max}}\right)^{a_2 \frac{t}{t_{\max}}}, \\ &\boldsymbol{x}_0 = \frac{1}{\boldsymbol{\lambda}} ln\left[-a_1 \cdot (1 - e^{-\lambda x}) \cdot sign(\boldsymbol{r} - 0.5)\right] + \boldsymbol{x}, \end{aligned} \quad (23)$$

- The third term is called generation rate, and is denoted as the vector $\boldsymbol{G}$. It can be calculated as follows:

$$\begin{aligned} &\boldsymbol{G} = \boldsymbol{G}_{CP}\left(\boldsymbol{C}_{eq} - \boldsymbol{\lambda}\boldsymbol{C}(t-1)\right)\boldsymbol{F}, \\ &\boldsymbol{G}_{CP} = \begin{cases} 0.5\boldsymbol{r}_1, & \boldsymbol{r}_2 \ge GP \\ 0, & \boldsymbol{r}_2 < GP \end{cases}. \end{aligned} \quad (24)$$

In (23) and (24), a_1 and a_2 stand for random numbers between 0 and 1, while $\boldsymbol{r}$, $\boldsymbol{r}_1$ and $\boldsymbol{r}_2$ are vectors of random numbers also in ran-

Mihailo Micev, Martin Ćalasan, Miljan Janketić, Comparative Analysis of Metaheuristic Algorithms for Parameters Estimation of Single-Cage and Double-Cage Induction Machine Models, Journal of Energy, vol. 74 Number 4 (2025), 41–46
https://doi.org/10.37798/2025743718

ge from 0 to 1. Also, *GP* stands for generation probability, whose value is set to 0.5, according to [14].

After reaching the maximum number of iterations t_{max}, the particle whose concentration has the lowest fitness function value is considered as the optimal solution.

IV. Results of the Optimization

In this section, the formulation of the optimization problem is firstly described. Afterward, the results of the parameters estimation procedure for SCM and DCM of two different induction machines are presented.

A. Formulation of the Optimization Problem

The most important step in application of metaheuristic algorithms is to define criterion function (*CF*). The goal of this paper is to estimate the parameters of the induction machine, so that the calculated values of torques, currents, and power factor match with the values from the nameplate of the machine. To be more precise, the criterion functions used in this work are given with the following equations:

$$\begin{aligned} CF_1 &= F_1^2 + F_2^2 + F_3^2 + F_4^2, \\ CF_2 &= F_1^2 + F_2^2 + F_3^2 + F_4^2 + F_5^2 + F_6^2, \end{aligned} \tag{25}$$

where functions F_1-F_6 are defined as follows:

$$\begin{aligned} &F_1 = \frac{T_{fl,c} - T_{fl,n}}{T_{fl,n}}; F_2 = \frac{T_{st,c} - T_{st,n}}{T_{st,n}}; F_3 = \frac{T_{\max,c} - T_{\max,n}}{T_{\max,n}}; \\ &F_4 = \frac{\cos(\varphi)_{fl,c} - \cos(\varphi)_{fl,n}}{\cos(\varphi)_{fl,n}}; F_5 = \frac{I_{st,c} - I_{st,n}}{I_{st,n}}; F_6 = \frac{I_{fl,c} - I_{fl,n}}{I_{fl,n}}. \end{aligned} \tag{26}$$

In the previously defined criterion function, index *fl* stands for full load, *st* denotes starting, max is maximum, and also *c* and *n* stand for calculated and nameplate value, respectively. Also, CF_1 is criterion function for single cage model, while CF_2 denotes criterion function for double cage model.

B. Case 1 – Estimation of Parameters of SCM of the Machine

Firstly, the parameters of the single cage model equivalent circuit of induction motor are estimated. The nameplate data of the considered motor are given in Table 1.

TABLE I.
Induction Motor 1 – Nameplate Data

Quantity	Description	Value
P_n	Nominal power	40 HP (horse power)
V_n	Nominal voltage	400 V
f	Frequency	50 Hz
p	Pole pairs	2
T_{st}	Starting torque	260 Nm
T_{fl}	Full-load torque	190 Nm
$T_{\max}$	Maximum torque	370 Nm
$\cos(\varphi)_{fl}$	Full-load power factor	0.8
s_{fl}	Full-load slip	0.09

The parameters of the SCM equivalent circuit of the presented induction motor (R_1, R_2, X_1, X_2, and X_m) are estimated using HBA and EO algorithms. The results are compared with the corresponding results obtained with SA-ERWCA algorithm [6]. The results of the estimation, along with the criterion function values, are given in Table 2.

TABLE II.
Induction Motor 1 – Results of the Estimation

Parameter	HBA	EO	SA-ERWCA
R_1	0.27821	0.27821	0.27821
X_1	0.68056	0.16343	0.20111
R_2	0.34216	0.39167	0.38795
X_2	0.25867	0.84936	0.80380
X_m	7.39873	7.91588	7.87820
CF	$3.88 \cdot 10^{-14}$	$1.993 \cdot 10^{-13}$	$1.6 \cdot 10^{-10}$

Furthermore, the graphical comparison of the obtained resultsis provided. Namely, the torque-slip and power factor-slip characteristics are calculated using the parameters from the previous table. The mutual comparison of the calculated characteristics is presented in Fig. 3 (torque-slip) and Fig. 4 (power factor-slip). Also, the nameplate values of torque and power factor are drawn on the corresponding figures.

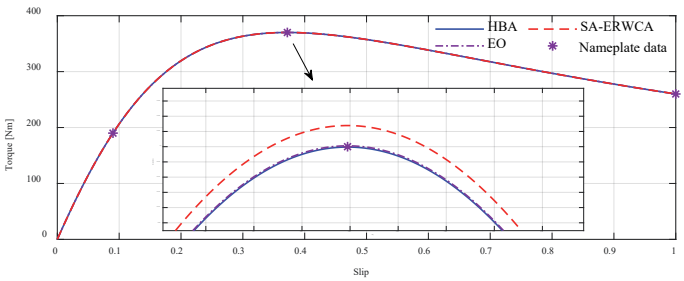

Fig. 3. Comparison of torque-slip characteristics for single cage model.

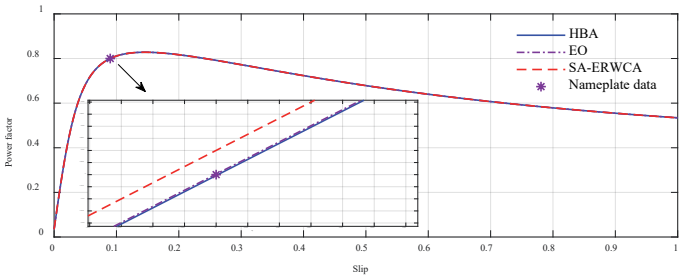

Fig. 4. Comparison of power factor-slip characteristics of single cage model.

Based on the results presented in Table 2, as well as the graphical comparison given in previous figures, it is evident that both HBA and EO algorithms can ensure better matching than the SA-ERWCA algorithm. Also, mutual comparison between HBA and EO algorithms shows that HBA algorithm provides slightly less criterion function value than EO algorithm.

C. Case 2 – Estimation of Parameters of DCM of the Machine

The parameters of the double cage equivalent circuit of the induction motor are estimated in the second case presented in this paper. The nameplate data of the considered motor are given in Table 3.

Mihailo Micev, Martin Ćalasan, Miljan Janketić, Comparative Analysis of Metaheuristic Algorithms for Parameters Estimation of Single-Cage and Double-Cage Induction Machine Models, Journal of Energy, vol. 74 Number 4 (2025), 41–46
https://doi.org/10.37798/2025743718

TABLE III
INDUCTION MOTOR 2 – NAMEPLATE DATA

Quantity	Description	Value
P_n	Nominal power	148 HP (horse power)
V_n	Nominal voltage	400 V
f	Frequency	50 Hz
p	Pole pairs	2
T_{st}	Starting torque	847.2 Nm
T_{fl}	Full-load torque	353 Nm
$T_{\max}$	Maximum torque	1094.3 Nm
$\cos(\varphi)_{fl}$	Full-load power factor	0.9
s_{fl}	Full-load slip	0.0077
I_{st}	Starting current	1527.2 A
I_{fl}	Full-load current	184 A

Considered EO and HBA algorithms are applied to estimate the parameters of the double cage model equivalent circuit – R_1, X_1, R_{11}, X_{1d}, R_{22}, X_{2d}, and X_m. Table 4 presents the comparison of obtained results with corresponding results from [6], where SA-ERWCA algorithm is applied.

TABLE IV.
INDUCTION MOTOR 2 – RESULTS OF THE ESTIMATION

Parameter	HBA	EO	SA-ERWCA
R_1	0.037748	0.0377021165	0.037614
X_1	0.03664	0.1113609818	0.050454
R_{11}	0.01077	0.01204092448	0.010833
X_{1d}	0.171758	0.1114089951	0.159068
R_{22}	0.162733	0.0500786904	0.135273
X_{2d}	0.150063	0.003877696845	0.112364
X_m	3.779905	3.705739386	3.767293
CF	$5.02 \cdot 10^{-11}$	$3.75 \cdot 10^{-10}$	$4.73 \cdot 10^{-9}$

Similar to the previously presented approach, the graphical comparison of the obtained results is also provided. To be precise, Fig. 5 presents the comparison of torque-slip characteristics, which are calculated using the parameters from the previous table. Also, the power factor-slip characteristics are presented in Fig. 6.

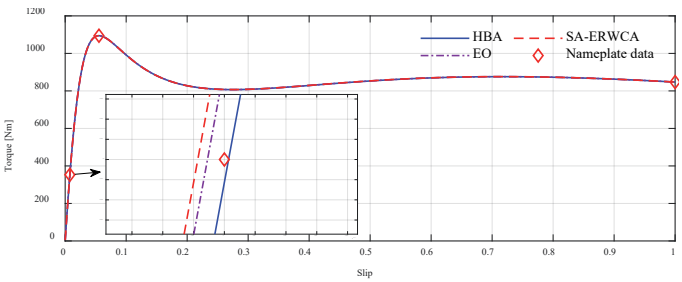

Fig. 5. Comparison of torque-slip characteristics for double cage model.

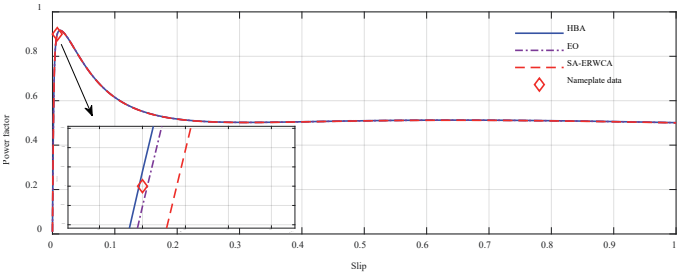

Fig. 6. Comparison of power factor-slip characteristics of double cage model.

As it can be seen from the previous figures, the characteristics calculated with parameters estimated with HBA have the best matching with the nameplate data. Very close matching is also provided with EO algorithm, while the application of SA-ERWCA algorithm leads to the results that are further from nameplata data compared with other two considered algorithms. The same conclusion can also be drawn observing the criterion function values from Table 4.

D. CONVERGENCE CURVES COMPARISON

One of the main characteristics of each metaheuristic algorithm is its' convergence curve, which denotes the criterion function value after each iteration. Therefore, the convergence curves for the algorithms applied in this paper are presented, in both considered cases.

In case 1, where the SCM equivalent circuit parameters are estimated, the parameters of both HBA and EO algorithm are selected to have equal values. Precisely, maximum number of iterations is 100, and the population size is also 100. The convergence curves comparison is depicted in Fig. 7.

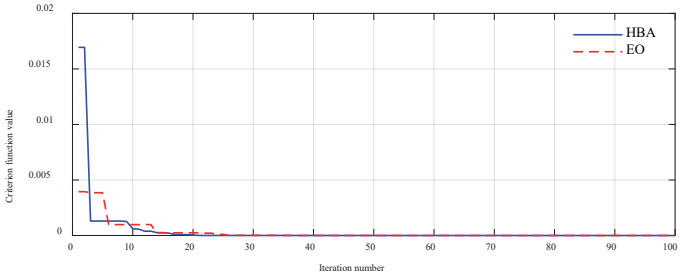

Fig. 7. Comparison of convergence curves – case 1.

In the second considered case, the parameters of DCM equivalent circuit are estimated. Population size and maximum number of iterations, for both HBA and EO algorithm, are selected to be 300 in this case. The graphical comparison of convergence curves is provided in case 2.

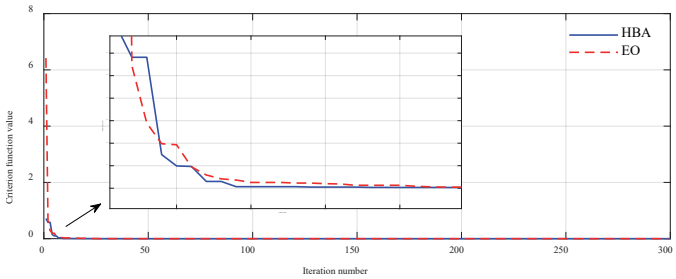

Fig. 8. Comparison of convergence curves – case 2.

The analysis of the presented convergence curves, in both of the considered cases, clearly proves the applicability of both HBA and EO algorithm for the estimation of IM equivalent circuits parameters. Both of the algorithms reach optimal solution really fast, after only a couple of iterations. Mutual comparison gives slight advantage to the HBA, because it reaches optimal solution before the EO algorithm.

V. CONCLUSION

This paper presented a comparative analysis of the Honey Badger Algorithm and Equilibrium Optimizer for the estimation of parameters of single-cage and double-cage induction machine models using nameplate data. The obtained results clearly demon-

Mihailo Micev, Martin Ćalasan, Miljan Janketić, Comparative Analysis of Metaheuristic Algorithms for Parameters Estimation of Single-Cage and Double-Cage Induction Machine Models, Journal of Energy, vol. 74 Number 4 (2025), 41–46
https://doi.org/10.37798/2025743718

strate that both algorithms provide high accuracy and fast convergence, with HBA showing a slight advantage in terms of convergence speed and criterion function value in all considered cases. The comparison with a previously published SA-ERWCA-based approach further confirms the effectiveness and robustness of the proposed methods for practical parameter estimation of induction machines.

Future work will be focused on extending the proposed methodology to include parameter estimation based on measured operational data, as well as the application of hybrid and adaptive metaheuristic algorithms. Additionally, the integration of the proposed estimation framework into real-time monitoring and control systems, as well as its validation on a wider range of induction machine ratings and operating conditions, will be considered.

References

[1] Krishnan R, Electric motor drives – Modeling, Analysis and Control, Prentice Hall, USA, 2001.

[7] IEEE Standard l12: Test Procedure for Polyphase Induction Motors and Generators, 2004.

[8] IEC standards 60034-28 IEC - Rotating Electrical Machines - Part 28. Test Methods for Determining Quantities of Equivalent Circuit Diagrams for Three- Phase Low-Voltage Cage Induction Motors, Dec.2012.

[9] Haque M. H, Determination of NEMA design induction motor parameters from manufacturer data, IEEE Trans. Energy Convers, Vol. 23, No. 4, pp. 997– 1004, 2008.

[10] Sakthivel P, Bhuvaneswari R, Subramanian S, Bacterial Foraging Technique Based Parameter Estimation of Induction Motor from Manufacturer Data, Elect. Power Comp. Syst, Vol. 38, pp. 657-674, 2010.

[11] M. Ćalasan, M. Micev, Z. M. Ali, A. F. Zobaa, and S. H. E. A. Aleem, "Parameter estimation of induction machine single-cage and doublecage models using a hybrid simulated annealing-evaporation rate water cycle algorithm," *Mathematics*, vol. 8, no. 6. 2020, doi: l0.3390/math8061024.

[12] Babau R, Boldea I, Miller T. J. E, Muntean, N.Complete parameter identification of large induction machines from no-load acceleration deceleration tests, IEEE Trans. Ind. Electr, Vol. 54, No. 4, pp. 1962– 1972, 2007.

[13] Jafari H. K, Monjo L, Corcoles F, Pedra J, Using the instantaneous power of a free acceleration test for squirrel cage motor parameters estimation, IEEE Trans. Energy Conv, Vol. 30, No. 3, pp. 974–982, 2015.

[14] Benzaquen J, Rengifo J, Albanez E, Aller J. M, Parameter Estimation for Deep-Bar Induction Machine Using Instantaneous Stator Measurements From a Direct Startup , IEEE Trans Energy Conv, Vol. 32, No. 2, pp. 516 – 524, 2017.

[15] Seok J. K, Moon S. I, Sul S. K, Induction machine parameter identification using PWM inverter at standstill, IEEE Trans. on Energy Conv, Vol. l2, No.2, pp. 127–132, 1997.

[16] Laroche E, Boutayeb M, Identification of the Induction Motor in Sinusoidal Mode, IEEE Trans Energy Conv, Vol. 25, No. l, pp. ll- 19, 2010.

[17] Repo A, Arkkio A, Numerical impulse response test to identify parametric models for closed-slot deepbar induction motors, IET Electr. Power Appl, Vol. l, No. 3, pp. 307–315, 2007.

[18] F. A. Hashim, E. H. Houssein, K. Hussain, M. S. Mabrouk, and W. Al-Atabany, "Honey Badger Algorithm: New metaheuristic algorithm for solving optimization problems," *Math. Comput. Simul.*, vol. 192, pp. 84–110, 2022, doi: 10.1016/j.matcom.2021.08.013.

[19] A. Faramarzi, M. Heidarinejad, B. Stephens, and S. Mirjalili, "Equilibrium optimizer: A novel optimization algorithm," *Knowledge-Based Syst.*, vol. 191, 2020, doi: 10.1016/j.knosys.2019.105190.

ENERGIJA